Department of Physics and Astronomy

Heidelberg University

Master's Thesis in Physics

submitted by

Sophie Armbruster

born in Frankfurt am Main (Germany)

2023

Background characterisation
and muon veto upgrade for the CONUS+ experiment

This Master's Thesis has been carried out by Sophie Armbruster at the
Max Planck Institut für Kernphysik in Heidelberg
under the supervision of
Prof. Dr. Dr. h.c. Manfred Lindner

Abstract

The CONUS+ experiment aims to detect coherent elastic neutrino nucleus scattering (CEνNS) involving electron antineutrinos by the Leibstadt nuclear power plant (KKL). Serving as the successor to CONUS, CONUS+ features an enhanced experimental setup, including an upgraded muon veto to address the increased muon radiation at the new experimental site. This work includes on-site muon and gamma flux measurements, Monte Carlo simulations to assess the impact of incorporating an additional muon veto layer into the CONUS+ shielding, the commissioning process, and the subsequent installation within the experimental setup. Measurements revealed that the muon rate at KKL will be 2.6 times higher than in the former experimental location in Brokdorf. To maintain a comparable background level to CONUS, the muon rejection must be elevated to over 99%. Notably, the initial run of the muon veto in KKL has demonstrated a promising alignment with the expected performance.

Abstrakt

Das Ziel vom CONUS+ Experiments ist es kohärente elastische Neutrino-Kern Streuung (CEνNS) mit Elektron Antineutrinos aus dem Kernreaktor in Leibstadt (KKL) nachzuweisen. CONUS+ ist das Nachfolger Experiment von CONUS und nutzt einen verbesserten Aufbau vom Conus Schild, einschließlich einem optimierten Myonvetos um der erhöhten Myon Strahlung am neuen Versuchsort gerecht zu werden. Diese Arbeit umfasst Messungen der Myonen und Gamma Strahlung vor Ort, Monte-Carlo-Simulationen, um das Ausmaß eines zusätzlichen Myonvetos in CONUS+ zu evaluieren, die Inbetriebnahme des Vetos und die anschließende Installation im Experiment. Messungen ergaben, dass die Myonenrate in KKL 2,6-mal höher sein wird als an dem früheren Versuchsort in Brokdorf. Um ein vergleichbares Hintergrundniveau wie bei CONUS aufrechtzuerhalten, muss das Verwerfen von Myon induzierten Ereignissen auf über 99% erhöht werden. Bemerkenswert ist, dass der erste Betrieb des Muonenvetos in KKL vielversprechend mit der erwarteten Leistung übereinstimmt.

Contents

Chapter 1

Introduction

If we gaze deep into the Universe, we can see stars and galaxies, yet concealed from the naked eye is that the Universe is filled with particles called neutrinos. These particles with little to no mass were created merely seconds after the creation of the Universe through the Big Bang [1]. As neutrinos rarely interact with matter, a large number of these primordial low-energy neutrinos remain in the Universe today.

Neutrinos were initially theorised by Wolfgang Pauli in 1933 as a vital explanation for conserving energy, momentum, and angular momentum in beta decay processes. It took almost 23 years for the first direct detection by the Cowan-Reines neutrino experiment [2]. Ever since then, several groundbreaking discoveries unfolded. Notably, the revelation of neutrino masses through neutrino oscillation [3] [4] resolved the long-standing solar neutrino problem, a large discrepancy between the flux of solar electron neutrinos on earth and the flux predicted from the Sun's luminosity [5]. However, how neutrino masses arise has not been answered conclusively, as in the Standard Model (SM), fermions solely gain intrinsic mass because of their interactions with the Higgs field. This interaction requires both left- and right-handed versions of the fermions. Since only left-handed neutrinos have been observed so far, neutrinos cannot interact with the Higgs boson and, therefore can not acquire any mass in the SM. Hence, neutrino masses imply an extension of the SM. An approach involves a particle called the Majorana neutrino, which allows the left-handed neutrinos to have Majorana masses [6]. This, however does not explain why neutrinos have significantly smaller masses than other known particles. A popular solution is the seesaw mechanism, which adds right-handed neutrinos with very large Majorana masses [7]. The quantum states of these particles are mixed, leading to an inverse relation of both neutrinos. The hypothetical heavy neutrino does not interact in any of the fundamental interactions. The seesaw mechanism also leads to the assumption that neutrinos are their own antiparticle. Currently, several double-beta decay experiments, including LEGEND [8], CUPID [9] and nEXO [10] are searching for lepton violation caused by massive Majorana neutrinos.

So far, neutrinos have been detected from many terrestrial and astrophysical sources and across a large range of energy scales. Figure 1.0.1 depicts the fluxes of natural and reactor neutrinos. As can be seen, nuclear

reactors produce neutrinos with MeV energies, while accelerator sources typically produce GeV energy neutrinos. On the other hand, astrophysical sources yield neutrinos across a broad energy spectrum, ranging from MeV to PeV energies.

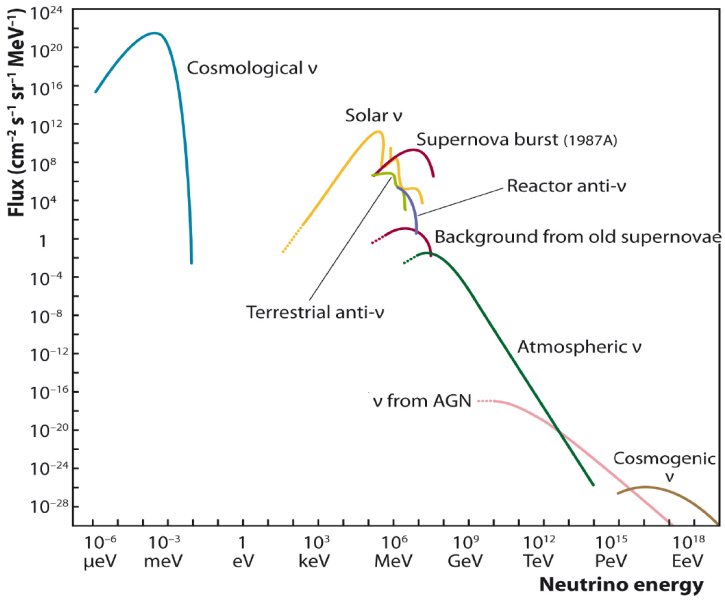

Figure 1.0.1: Fluxes of natural and reactor neutrinos. The highest energy neutrinos come from sources like supernova remnants, Gamma Ray Bursts or Active Galactic Nuclei (AGN) [11].

Neutrinos engage with matter through several interaction channels, including neutrino-electron elastic scattering as well as neutral and charged current inelastic neutrino-nucleus interactions. In the former case, detectors identify the energy in the outgoing electron, whereas in the latter case, detectors identify either a charged lepton produced in a charged current interaction or a MeV gamma in the case of inelastic nuclear interactions.

The most commonly employed detection mechanism is the inverse beta decay (IBD) ($\bar{\nu}_e + p \rightarrow e^+ + n$), where both the outgoing positron and neutron may be detected. However, detection through IBD has several disadvantages, including a 1.6 MeV energy threshold and a relatively low cross-section. A novel alternative method for neutrino detection is Coherent Elastic Neutrino Nucleus Scattering, also known as CEνNS. In CEνNS, neutrinos interact with the nucleus as a whole and do not need to satisfy an energy threshold. Due to coherency enhancement, the cross-section for a CEνNS interaction is significantly larger for the IBD. Even though the total cross section is large compared to other neutrino interactions, detecting CEνNS is challenging due to the small recoil energy deposited in the target material.

In 2017, the COHERENT collaboration achieved the first-ever detection of CEνNS using a stopped-pion source with a CsI[Na] scintillating crystal detector [12]. Subsequent to this, COHERENT achieved a complementary measurement of CEνNS with a single-phase liquid argon target in March 2020 using the same

neutrino source [13]. This marked an important milestone as it not only confirmed the predictions of the SM but also inspired new constraints on beyond standard model physics.

However, due to the energy of accelerator neutrinos, the observed CEνNS interactions at COHERENT are not in the fully coherent regime. Hence, several experiments are currently trying to detect CEνNS in the fully coherent regime using reactor electron antineutrinos at much lower energies. A detection would serve as both validation of the standard model and as a powerful tool in exploring novel physics beyond the standard model.

In the following chapter, I will delve deeper into coherent elastic neutrino nucleus scattering, exploring possible neutrino sources as well as the underlying physical motivation for CEνNS detection. Furthermore, I will continue with the backgrounds of ultra-low threshold experiments and end with an overview of past and current experimental efforts.

1.1 Coherent Elastic Neutrino Nucleus Scattering

Coherent Elastic Neutrino Nucleus Scattering was first predicted in 1974 by Freedman [14]. In a CEνNS interaction, neutrinos engage in a flavor-blind exchange involving a neutral Z boson with every nucleon within the nucleus

$$\nu + (N,Z) \rightarrow \nu + (N,Z). \tag{1.1}$$

In this process, solely energy and momentum are transferred, and the quantum numbers of the initial and final state remain unchanged. The differential cross section for CEνNS is expressed as

$$\frac{d\sigma}{d\Omega} = \frac{G_f^2 \cdot M}{16\pi} \cdot \left(N - (1 - 4sin^2\theta_W)Z\right)^2 E_\nu^2 (1 + cos\theta) F^2(Q^2), \tag{1.2}$$

where G_F denotes the Fermi constant, F is the form factor depending on the momentum transfer Q, M is the mass of the target nucleus, E_ν is the energy of the incoming neutrino, θ is the scattering angle and θ_W is the Weinberg angle. The coherency requirement necessitates an upper limit in neutrino energies, a parameter that can be derived from the nucleus's diameter. In the case of germanium nuclei (Z=32 and N=38-42), energies below 20 MeV ensure coherency, as the momentum transfer is smaller than the reciprocal of the nucleus's diameter $d_{nuc} = 0.0127\sqrt[3]{N+Z}$ [1/MeV]. With increasing energy, the single constituents of the nucleus become visible. This is expressed in the nuclear form factor $F(Q^2)$ that approaches unity in the coherence limit $Q^2 \rightarrow 0$.

At low energies, the Weinberg angle θ_W is ~ 0.23 [15]. This prompts the proton number to nearly drop out, leading to a cross-section proportional to the number of neutrons squared N^2. Consequently, this implies that CEνNS is mainly sensitive to the neutron distribution in the nucleus. Due to coherence enhancement,

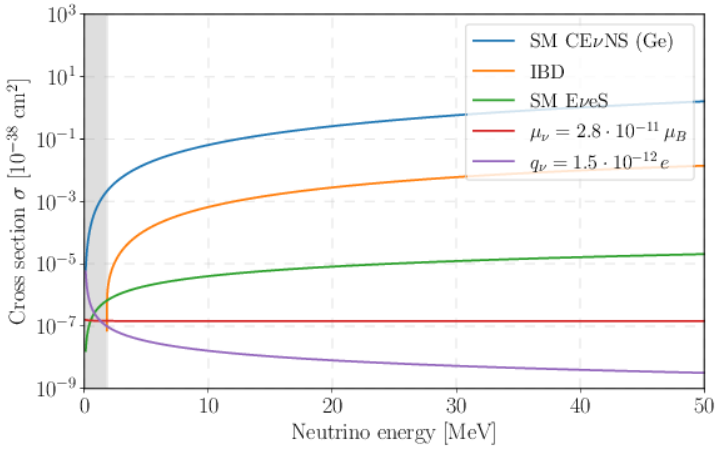

Figure 1.1.1: Neutrino interaction cross sections below 50 MeV. The CEνNS cross section is about two orders of magnitude larger than the one for inverse β decay [16].

the cross-section is proportional to the neutrino energy E_ν squared. In Figure 1.1.1 the cross-section of CEνNS in a germanium target is compared to other neutrino interaction channels. Clearly, the cross-section for CEνNS is about two orders of magnitude larger than for inverse β-decay and about four orders of magnitude larger than elastic neutrino-electron scattering (EνeS). The large cross-section allows physicists to build compact neutrino detectors with sensitivities similar to multi-ton experiments.

Nonetheless, the search for CEνNS poses several experimental challenges as the experimental signature for the interaction is a low-energy recoil of the nucleus. The maximum recoil energy T_{max} of the nucleus with mass m_A after interaction with neutrino with energy E_ν is given by:

$$T_{max} = \frac{2E_\nu^2}{m_A + 2E_\nu} \tag{1.3}$$

T_{max} is inversely proportional to the mass of the nucleus. This creates a push-pull situation. While larger cross sections promote heavier nuclei, the recoil energy diminishes alongside mass. Therefore, a medium mass number is ideal for the detection of CEνNS. Notably, Germanium (Ge) serves as an exemplary candidate.

Assuming a germanium target nucleus with a mass of $m_A \approx 68.84$ GeV, the maximum recoil energy T_{max} in the fully coherent regime for $E_\nu = 10$ MeV and $E_\nu = 1$ MeV neutrinos leads to nuclear recoils of about 3 keV and 0.03 keV respectively. This illustrates the experimental requirement for very low threshold detectors.

1.2 Physical motivation

The detection of CEνNS serves not only as a way to validate the SM but also as a powerful instrument to search for new physics and probe the nuclear structure. Examining the cross-section in Equation 1.2 it

is apparent that a detection of CEνNS with high statistics allows to evaluate input parameters with great precision. This includes the nuclear form factor and the Weinberg angle, a fundamental parameter of the electroweak theory. This parameter is traditionally determined at much higher energies at colliders as from the ratio of the W and Z boson masses by measuring the mass at $\sim$100 GeV [15]. CEνNS offer a tool to examine the momentum dependence at lower energies where any deviation from SM predictions could potentially unveil new physics.

CEνNS experiments inherently search for physics beyond the Standard Model. Two specific BSM physics scenarios probed include sterile neutrinos or non-standard interactions (NSI). Sterile neutrinos are hypothetical particles that are believed to interact only via gravity and not via other interactions of the SM [17]. Since CEνNS experiments are sensitive to the total active neutrino flux, they could potentially search for sterile neutrinos by comparing the energy spectrum of nuclear recoil events at different baselines [18]. NSI can be described by modifying the weak charge in the cross section within Equation 1.2 with additional couplings ε. New NSI or exotic neutral current interactions would modify the overall CEνNS cross section predicted by the SM [19].

As previously discussed, the observations of neutrino oscillations suggest that neutrinos have mass. This also motivates the existence of neutrino electromagnetic properties in the form of a neutrino magnetic moment (NMM) or a neutrino charge radius. A sizeable neutrino magnetic moment would manifest in a CEνNS experiment as an excess of low energy recoil events [19].

Expanding its utility, CEνNS could also serve as an instrument for monitoring reactors and nuclear waste at great distances. An advantage of CEνNS detectors, compared to the traditionally used IBD decay detector, lies in a larger cross-section. Additionally, the CEνNS interaction is not limited by the 1.8 MeV neutrino threshold as the IBD decay is [20]. However, due to the current status of detection technologies, conventional monitoring tools are preferred.

Furthermore, CEνNS interactions play an essential role in astrophysical models as they affect the hydrodynamic behaviour of the stellar collapse of iron-core stars to hot neutron stars surrounded by a thin iron layer. Here, the neutrinos from the outer layer scatter coherently outward and accelerate the iron layer to above escape velocity. This is further elaborated in [21]. Moreover, CEνNS interactions present a background in direct dark matter searches, limiting the reach of detectors. This will be explored in a subsequent section.

1.3 Neutrino sources for CEνNS detection

Despite the substantial cross-section of the CEνNS interaction, its measurement introduces a formidable experimental challenge due to the small recoil energy involved. There are three perquisites to be satisfied for a successful CEνNS experiment: a potent neutrino source with neutrino energies within the coherent regime, a suitably low energy threshold and an effective suppression of background. For a coherently en-

hanced interaction, the neutrino sources are required to produce neutrinos with energies in the MeV regime. Currently, the most favoured neutrino sources for the detection of CEνNS are the πDAR sources and nuclear reactors. Recent advancements in direct dark matter experiments have ushered solar neutrinos into the discourse as plausible contenders potentially serving as alternative sources for CEνNS.

1.3.1 πDAR source

Spallation sources produce both π^+ and π^- through proton collision with nuclei. While a significant fraction of π^- are captured, thus failing to produce neutrinos, the produced π^+ lose energy and decay at rest. Subsequently, μ^+ born from this process decay at rest and produce $\bar{\nu}_\mu$ and ν_e neutrinos.

$$\pi^+ \rightarrow \mu^+ + \nu_\mu \qquad\qquad \mu^+ \rightarrow e^+ + \bar{\nu}_\mu + \nu_e \tag{1.4}$$

Due to the lifetime of the decay, $\bar{\nu}_\mu$ and ν_e emerge with a noticeable 2.2 μs delay [22] compared to the promptly generated ν_μ from the initial pion decay. The neutrinos reach energies of up to 50 MeV. This allows for a large CEνNS cross-section and, in tandem, large recoil energies. However, this comes at the price of a not fully coherent interaction.

1.3.2 Solar neutrinos

The Sun is an abundant source of electron neutrinos radiating forth a substantial flux of $2 \cdot 10^{38} \nu_e$ per second through nuclear fusion [23]. A vast majority of solar neutrinos come from the main hydrogen-burning process, termed the p-p chain:

$$p + p \rightarrow D + e^+ + \nu_e. \tag{1.5}$$

The neutrinos produced in this process have low energies of up to 400 keV. The highest energy solar neutrino originates from the β-decay of $^8_5$B that is produced from the fusion of two helium nuclei

$$^8_5\mathrm{B} \rightarrow ^8_4\mathrm{Be}^* + e^+ + \nu_e \tag{1.6}$$

with an energy of up to 15 MeV. However, these interactions produce a much lower neutrino flux. Therefore, solar neutrinos are not commonly used as neutrino sources for CEνNS experiments due to their comparatively modest flux on Earth. However, they are currently becoming more relevant as next-generation dark matter experiments increase their masses while simultaneously decreasing their energy thresholds.

1.3.3 Nuclear reactors

Reactors are high-intensity isotropic sources of electron antineutrinos. The antineutrinos are produced in the β^--decay of fission fragments of uranium and plutonium. On average, six $\bar{\nu}_e$ are released per fission. For a typical commercial reactor with 3 GW thermal power and yielding approximately 200 MeV per fission,

an astounding amount of 6×10^{20}antineutrinos are released per second [24]. The electron antineutrinos are emitted with energies of up to $\sim$ 10 MeV which largely ensures the coherence recoil condition over the entire reactor energy regime [25]. However, the trade-off surfaces in the form of low nuclear recoil energies that present great experimental challenges for detection. Moreover, background suppression is especially demanding at nuclear reactor sites. This will be discussed in the next section.

Table 1.1 compares the πDAR source and the nuclear reactor in the context of CEνNS experiments. πDAR sources produce different flavor neutrinos with energies of $\sim$20 to 50 MeV, making them easier to detect, however at the cost of a fully coherent interaction. On the other hand, nuclear reactors produce only electron antineutrinos at energies below 10 MeV, which are harder to detect, but the interaction is in the fully coherent regime.

Source	Flavour	Energy	Pro	Con
πDAR source	$\nu_e \nu_\mu\ \bar{\nu}_\mu$	$\sim$20-50 MeV	• Higher recoil energies	• Not fully coherent interaction
Reactor	$\bar{\nu}_e$	<10 MeV	• Fully coherent	• Lower recoil energies • Strict safety restrictions

Table 1.1: Comparison of πDAR source and nuclear reactors in CEνNS experiments.

1.4 Background suppression at nuclear reactor sites

In the pursuit of a CEνNS detection, the effective suppression of background signals is essential. This challenge becomes especially pronounced for experiments located at nuclear reactor sites. In the following section, I will give an overview of background contributions and their corresponding shielding strategies in reactor experiments.

1.4.1 Cosmic rays

Cosmic rays compromised of high energy charged particles and gamma rays produce secondary radiation upon impact with Earth's atmosphere in the form of particle showers. At sea level, a flux of about 300 $\mathrm{m}^{-2}\mathrm{s}^{-1}$ [26] is expected, existing of x-rays, protons, alpha particles, pions, muons, electrons, neutrinos, and neutrons.

Neutrons and charged mesons, such as positive or negative pions and kaons are significant products of these

collisions. To combat the background induced by cosmic radiation, most experiments involve shielding, often in the form of a large overburden. An overburden of 50 meters water equivalent (m w.e.) is sufficient to substantially reduce radiation, particularly photons, protons and electrons.

Muons make up the majority of particles of the cosmic ray flux at sea level [27]. They are created via the decay of kaons and pions.

$$\begin{aligned} \pi^+ &\to \mu^+ + \nu_\mu \quad \pi^- \to \mu^- + \bar{\nu}_\mu \\ K^+ &\to \mu^+ + \nu_\mu \quad K^- \to \mu^- + \bar{\nu}_\mu \end{aligned} \tag{1.7}$$

Incoming muons can induce additional neutrons inside the detector via spallation, which then can cause signals similar to CEνNS events. With a mean energy of ~ 4 GeV [26] muons are quite difficult to shield. They lose energy through ionisation and radiation processes with their mean energy shifting to higher levels as depth increases. To significantly reduce muon flux, an overburden of more than 1000 m w.e. [28] would be required, a feat achievable only in underground facilities. Figure 1.4.1 illustrates the reduction rate of secondary and tertiary cosmic rays relevant to cosmic ray-induced background of shielded detectors and of neutrons from primordial radionuclides. However, since almost all nuclear power plants are located at the surface, many experiments adopt a different strategy, employing muon anti-coincidence systems, commonly known as muon vetos. Cherenkov detectors are a common choice as muon veto in low background experiments. They are typically composed of a large water tank surrounding the inner detector and are equipped with waterproof photomultiplier tubes (PMTs). Most muons are of high energy, i.e., highly relativistic. If they have a velocity greater than the phase velocity of light in water, Cherenkov light is emitted [29]. The produced light is then collected by the PMTs.

Other methods include surrounding the detector with plastic scintillator plates that, upon being struck by an incoming particle, absorb its energy and scintillate. The produced light is then collected by a PMT. Muon vetos using plastic scintillators have the advantage of being more compact and producing more light. They will be further discussed in the upcoming sections. In both cases, data collection pauses within a specific time window after each detected muon signal, thereby reducing muon-induced background.

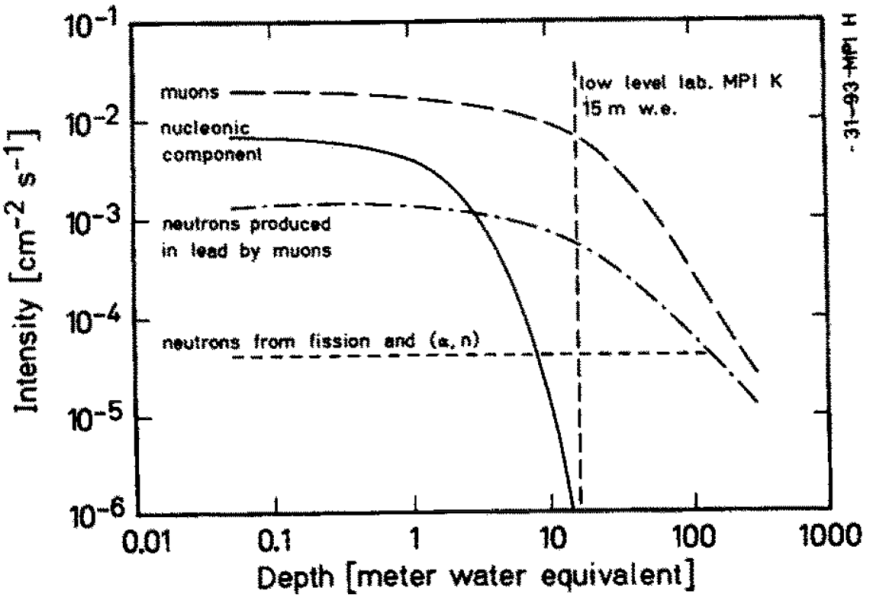

Figure 1.4.1: Reduction of cosmic radiation in dependence of depth in m w.e. [28].

1.4.2 Natural radioactivity

Other backgrounds arise from the material of the experiment's components and the surrounding environment. Primordial radioactivity, stemming from the uranium and thorium series, can be found everywhere on Earth's surface and is thereby present in many materials such as concrete. Gamma rays are emitted in their decays and have energies of up to several MeV. These gammas interact with matter via the photoelectric effect, Compton scattering and e^-e^+ pair production, processes that either release an electron or, in the case of pair production, both an electron and positron.

The background suppression techniques depend on the source of radiation. To suppress radiation stemming from the components of the experiment themselves, materials with low radioactive traces are meticulously selected. On the other hand, the background originating from the surrounding environment is suppressed by enveloping the detector in a material of high atomic number, density ρ and large γ-ray attenuation coefficient μ_{att}.

The radiation intensity after a shield thickness of x and an intensity of $I(0)$ before the shield is given by:

$$I(x) = I(0)exp(-x\rho\mu_{att}). \tag{1.8}$$

In rare cases, nuclear decays result in the emission of neutrons. To spontaneously emit neutrons, nuclei need a large excess of neutrons or need to be very heavy. The spontaneous fission of heavy nuclei is also a source of neutrons but with very low probabilities. Because collisions with light nuclei are far more effective at moderating neutrons [30], materials for neutron moderation will have high amounts of hydrogen or other

low atomic weight elements. For these reasons, water, polyethylene, and polycarbonate are typically used for neutron shielding.

1.4.3 Radon

Radon is a noble gas emanated from both the materials of the detector components and its surroundings, containing traces of uranium (^{222}Rn) and thorium (^{220}Rn). While the parent isotopes decay within the materials, radon can emanate to the ambient air. Typical domestic levels are approximately 50 Bq/m^3 [31] but in closed spaces like cellars or underground laboratories, radon concentration can rise significantly. ^{222}Rn is the most relevant isotope as it is the most abundant. When ^{222}Rn eventually decays, betas, alphas and nuclear recoils are emitted that can reach the active volume of the detector and produce a background signal [32].
Radon can be suppressed by sealing the detector radon tight, for example with radon tape, or by flushing the shield with radon-free gas. Boil-off nitrogen gas is often employed for this purpose due to its ready availability as a byproduct of liquid nitrogen cooling. However, some nuclear power plants prohibit the use of liquid nitrogen, therefore alternatives such as radon-free air are used.

1.4.4 Cosmogenic activation

Hadronic components of cosmic rays at Earth's surface can activate materials through spallation reactions [33]. This leads to the creation of radioactive isotopes, which can have half-lives ranging from seconds to several years. For example, for neutrons above 20 MeV the following reaction in germanium occurs:

$$^{70}Ge + n \rightarrow ^{68}Ge + 3n. \tag{1.9}$$

To minimise their influence, detector parts are ideally placed underground at depths exceeding 10 m w.e.. Activation ceases at depths beyond 10 m w.e., resulting in only the decay products remaining. Consequently, background diminishes over time.

1.4.5 Reactor correlated background

All the previously discussed background sources are common to experiments conducted at shallow depths. However, nuclear power plants introduce additional potential backgrounds due to fission reactions occurring within the reactor core. This is especially important for experiments situated close to the reactor. The reactor correlated background includes both neutron and gamma-ray emissions.

Within a nuclear power plant, neutrons generated by fission in the reactor core can induce further fission reactions within fuel assemblies. In each fission reaction, around 2 to 3 neutrons are produced, depending on the fissile isotope. While most neutrons continue fission, some may escape the reactor core. These fission

neutrons, with an average energy of 2 MeV [34], engage in either elastic or inelastic scattering off nuclei or undergo capture, upon interacting with matter. Especially elastic scattering poses a dangerous background for CEνNS searches due to its recoils bearing resemblance to CEνNS events. Due to their high penetration length, neutrons need additional shielding by materials such as polyethylene as was previously discussed for natural radiogenic neutrons.

The fission process also creates high energy gamma radiation [35]. Since gamma rays are best absorbed by materials with high atomic numbers and high density, lead is a specially suitable material for gamma radiation shielding.

These additional background contributions make it necessary to perform extensive measurement campaigns at the experimental site and to use Monte Carlo (MC) simulations to evaluate the contributions remaining inside the shield.

1.5 Experimental efforts

In recent years, the field of CEνNS has garnered significant attention. Consequently, a multitude of ongoing and upcoming experiments are dedicated to CEνNS observation and exploration. In the subsequent sections, a short selection of experiments will be presented to provide a comprehensive overview of the ongoing advancements in the field.

1.5.1 COHERENT

The COHERENT collaboration was the first to measure nuclear recoils from CEνNS successfully. COHERENT is a multitarget experiment located at the Spallation Neutron Source (SNS) in Oak Ridge, US which produces a well-known neutrino spectrum from pion and muon decay at rest. The experimental setup consists of six detectors that are installed in a corridor parallel to the proton beam, also called neutrino alley. Figure 1.5.1 shows the arrangement of the COHERENT detectors within the neutrino alley.

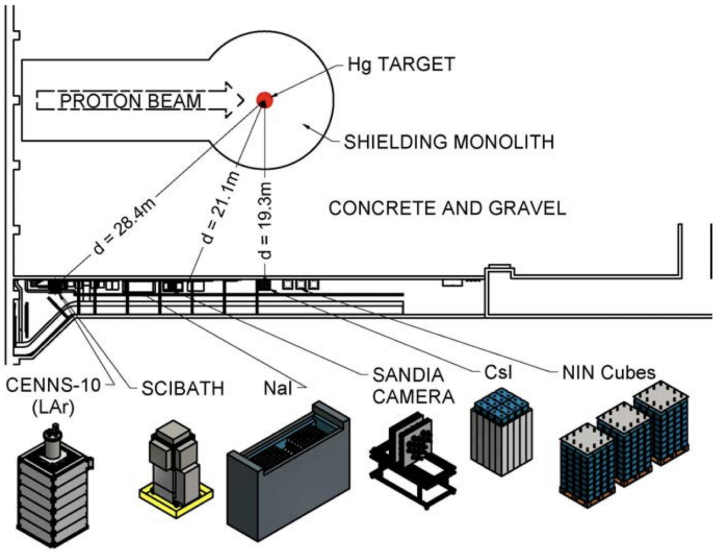

Figure 1.5.1: COHERENT detectors at SNS [12].

In the year 2017, a pivotal milestone was achieved by COHERENT as it recorded the first CEνNS detection with a 14.6 kg low-threshold CsI[Na] detector [12]. The signal derived from this measurement was consistent with the SM prediction at one sigma level. A complementary measurement of CEνNS was performed with a 24 kg liquid argon target in March 2020 [13], in which the collaboration also reported no deviation of the measured cross-section from the SM prediction.

1.5.2 Dark matter and CEνNS detectors

As previously explained, neutrinos stemming from astrophysical sources such as the Sun can produce nuclear recoils via CEνNS. However, while offering invaluable insights into astrophysical processes, they simultaneously present an irreducible background for direct dark matter searches. This is because, in experiments dedicated to directly detecting dark matter via elastic scattering off nuclei, CEνNS' recoils look remarkably similar to signals arising from dark matter. The so-called "neutrino-floor" that limits the reach of dark matter detectors is shown in Figure 1.5.2. The cross-section of dark matter to interact with nuclei is shown as a function of the dark matter mass. The neutrino floor from CEνNS of solar, diffuse background from supernova and atmospheric origin is depicted in light blue. The curves show exclusion limits from different experiments. As can be seen from the image, at low dark matter masses the neutrino floor limits the reach of dark matter detectors. As future dark matter experiments increase in size and decrease energy thresholds, they will become sensitive to CEνNS from solar neutrinos. Current dark matter experiments are already searching for CEνNS as for instance XENON1T [36] and the LZ dark matter experiment.

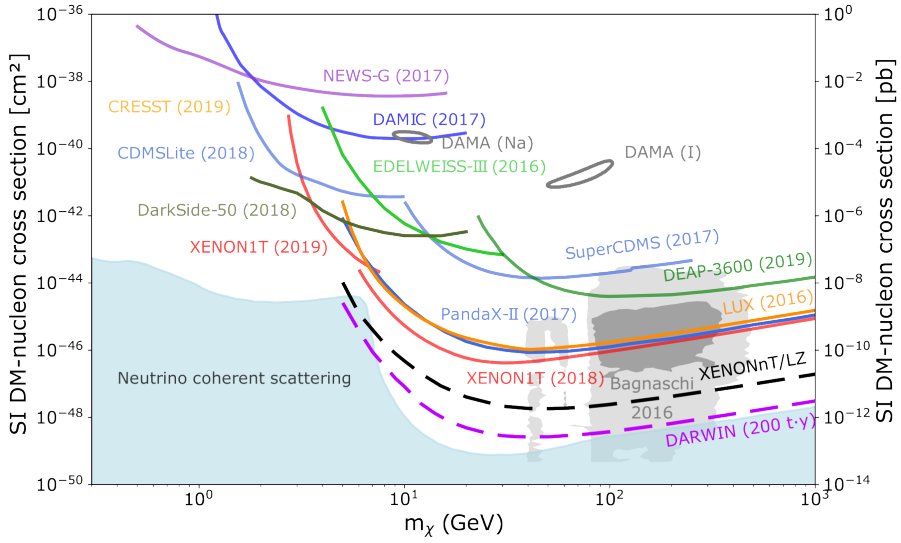

Figure 1.5.2: WIMP dark-matter search parameter space. the neutrino floor, depicted in light blue, limits the reach of dark matter detectors [37].

1.5.3 Reactor experiments

As reactor neutrinos are produced in the fully coherent regime, CEνNS experiments at reactors have the potential to disentangle new physics from nuclear physics effects. Currently, several experiments are either running, being commissioned or being constructed.

Among the currently running experiments is CONNIE [38], located 30 m from the core of the Angra 2 reactor in Brazil. CONNIE uses fully depleted, high-resistivity CCDs as particle detectors which allow to detect very low threshold energies of 5.5 eV. The latest results published by CONNIE state that the observed upper limit in the lowest energy range of 50 to 180 eV is 66 times above the SM prediction [39].

The TEXONO [40] experiment runs since 2003 and is located a distance of 28 m from the Kuo-Sheng power plant core in Taiwan. TEXONO uses 0.5 and 1.5 kg high-purity Germanium spectrometers. Data taking and analysis are ongoing [41].

νGen [42] is situated at the Kalinin nuclear power plant with 11 m from the nuclear reactor core. νGen stands out with the construction of a special movable platform to move its setup, consisting of high-purity germanium (HPGe) detectors, closer to the reactor core. This allows changing the flux by 21%. Its latest upper limit is a factor 7 above the SM prediction at a 90% CL.

The CONUS [43] experiment also used HPGe spectrometers at 17.1 m from the core of the nuclear power plant in Brokdorf, Germany. In 2020, the CONUS collaboration reported the best limit at that time on CEνNS with antineutrinos emitted from a nuclear reactor off germanium nuclei of 0.4 $d^{-1}kg^{-1}$, a factor 17 over the SM prediction (90 % C.L.). The analysed data includes 248.7 kg days with the reactor turned on and background data of 58.8 kg days with the reactor off.

The CONUS project continued data collection until and beyond the end of the reactor operation in late 2021 with additional improvements in the data acquisition systems and a better understanding of the quenching factor in germanium. These improvements lead to the preliminary new limit that is below a factor 2 above the SM prediction.
In 2022, the DresdenII [44] experiment claimed a detection of CEνNS using a 3 kg HPGe detector at the power reactor of the same name, 10.39 m from its core. However, this result is in tension with the other germanium experiments as TEXONO, νGen and CONUS.
RICOCHET [45] is an upcoming experiment that plans to use cryogenic bolometers to detect phonons induced by CEνNS interactions. The ILL research reactor in Grenoble, France, was selected as the experiment site.
The cryogenic bolometer technology will also be used by another upcoming experiment, NUCLEUS [46]. The NUCLEUS experiment will operate at the Chooz nuclear power plant in France located between the two reactor cores of 4.25 GW thermal power each. The NUCLEUS experiment is foreseen to use 10 g $CaWO_4$ and Al_2O_3 crystals aiming to feature a very low energy threshold of 10 to 20 eV.

Another upcoming experiment utilising HPGe spectrometers in the search for CEνNS from reactor antineutrinos is CONUS successor experiment CONUS+. In the following section, I will elaborate on the former CONUS setup and discuss its experimental challenges. Finally, I will introduce the CONUS+ detector.

Chapter 2

The CONUS+ Experiment

Numerous experiments are currently in preparation with the shared goal of detecting CEνNS with electron antineutrinos from nuclear reactors using high-purity germanium spectrometers. Among them, the CONUS experiment stands as one of the leading experiments, which was briefly introduced in the last chapter.
CONUS operated from 2018 to 2022, positioned at 17.1 m from the core of the Brokdorf nuclear power plant (KBR) in Germany. However, due to the shutdown of the power plant, CONUS had to be relocated to a new reactor site, specifically the Leibstadt nuclear power plant (KKL) in Switzerland.
This led to CONUS+, the follow-up experiment of CONUS, utilising an upgraded setup of CONUS.

This chapter begins with an introduction to high-purity germanium detectors. Subsequently, the chapter will delve into the CONUS experimental setup, its background and the scientific results achieved during its operation. Following this, the focus shifts towards CONUS+, where the enhancements and improvements made to the setup are discussed in comparison to its predecessor, CONUS.

2.1 High purity germanium detectors

High-purity germanium (HPGe) spectrometers have established themselves as popular choices of detectors used in CEνNS experiments due to their excellent energy resolution and thus low energy threshold, the relatively high target mass as well as the radio-purity of the detector material. Besides germanium, crystalline silicon is also a commonly applied material for low-threshold detectors.
HPGe spectrometers are semiconductor detectors. In semiconductors and insulators, electrons are confined within energy bands and are forbidden from other regions. The term *band gap* refers to the energy difference between the top of the valence band and the bottom of the conduction band. Electrons can transition between these bands, but this requires a specific minimum amount of energy for the process to occur.
Semiconductors, unlike non-conduction insulators, feature very narrow band gaps. In the case of ger-

manium, at a temperature of 77 K, the temperature of liquid nitrogen, the band gap is $E_g = 0.67$ eV. To increase the number of free charge carriers, i.e., electrons in the conduction band or holes in the valence band, single foreign atoms are implemented into the crystal structure. This process is called doping. Doping introduces extra levels into the band structure. In n-type materials, electron energy levels near the top of the band gap allow easy excitation into the conduction band. In contrast, in p-type material, extra holes in the band gap enable the excitation of valence band electrons, resulting in mobile holes in the valence band. When both types are brought into contact, a pn-junction is established, as depicted in the image (a) of Figure 2.1.1. The free charge carriers diffuse to the opposite side, recombining at the midpoint, thus generating the depletion region. Applying an external voltage in reverse bias expands the depletion region across the entire volume, transforming the semiconductor into a diode, as illustrated in the image (b) of Figure 2.1.1.
Germanium is the material of choice due to its intrinsic high purity. In CONUS, the detectors achieved approximately one impurity atom per 10^{12} Ge atoms. This allows for a high voltage of only a few kV to fully deplete the detector and minimise the risk of charge trapping, resulting in a high charge collection efficiency. The excellent energy resolution in germanium detectors can be attributed to the minimal energy required to create electron-hole pairs.
Furthermore, since germanium has a relatively low band gap, the detectors must be cooled down to temperatures well below -100°C to reduce the thermal generation of charge carriers, commonly referred to as leakage current.

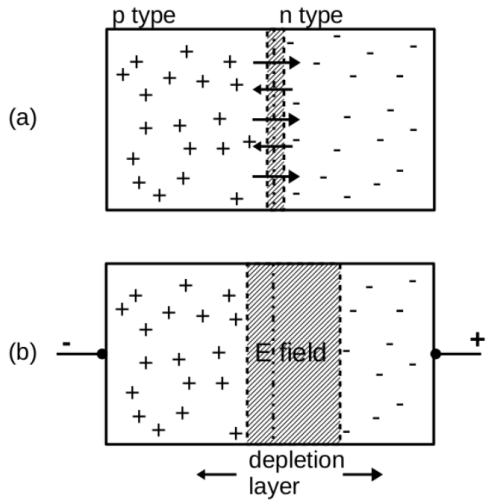

Figure 2.1.1: A pn-junction. Figure a) P-type and n-type semiconductor materials are brought into contact forming a pn-junction. In figure b) external HV is applied in reverse bias. Figure taken from [47].

In semiconductor detectors, charged particles create hole and electron pairs by ionisation in a present electric field under reverse bias. Neutral particles such as neutrinos and photons can create electron-hole pairs indirectly by inducing recoils of the nuclei of the detector material that free charges. The charge car-

riers are then pulled by the electric field towards the electrodes. This charge, which is in proportion to the energy deposited in the detector by the incoming photon, is converted into a voltage pulse by an integral charge-sensitive preamplifier.

The energy resolution in germanium detectors is defined as the contribution of five independent terms: intrinsic line width σ_{intr}, statistical uncertainty on the number of produced electron-hole pairs σ_{eh}, uncertainty on the charge collection σ_{coll}, electronic noise σ_{noise} and environmental vibrations σ_{env}. The independent resolutions add up quadratically to the overall resolution:

$$\sigma^2 = \sigma_{intr}^2 + \sigma_{eh}^2 + \sigma_{coll}^2 + \sigma_{noise}^2 + \sigma_{env}^2 \tag{2.1}$$

The σ_{noise} is typically the dominating term and is proportional to the noise peak width. It is produced by the preamplifier electronics and thus can be measured by injecting signals of known amplitude from a pulse generator into the electronics chain.

CONUS employs four HPGe spectrometers inside its onion-like shielding layers. The entire CONUS setup will be discussed in the next section.

2.2 CONUS

The CONUS experiment aimed to detect COherent elastic Neutrino nUcleus Scattering of reactor antineutrinos using cryocooled high purity germanium (HPGe) detectors. The experiment was developed at the Max Planck Institut für Kernphysik in Heidelberg in collaboration with Preussen Elektra GMBH from the nuclear power plant in Brokdorf (KBR), Germany where CONUS was set up. The operation started in 2018 and data taking stopped at the end of 2022.

There are five data collection phases. RUN-1 includes April 1st to October 29th 2018 and RUN-2 May 16th to September 23rd, 2019. Due to a regular leakage test of the entire reactor containment vessel, inducing an overpressure of 1.5 bar absolute, each detector was ventilated and then filled with ultrapure argon gas to prevent damage. Afterwards the detectors were evacuated again but unfortunately, this led to an enhanced background level by a factor of two. Therefore RUN-3 and RUN-4 were not included in the data analysis. The last phase RUN-5 took data from May 2021 to December 2022 with additional improvements to the data acquisition system. As of writing this thesis analysis of RUN-5 is still ongoing.

The CONUS experiment was located in room A-408 at KBR at a distance of 17.1 m from the reactor core centre. At this position an antineutrino flux of $2.4 \cdot 10^{13} \mathrm{s}^{-1}\mathrm{cm}^{-2}$ is expected. Notably, room A-408 lies beneath the spent fuel storage pool, a reservoir dedicated to the transportation casks of the spent fuel elements. These arrangements together with the substantial concrete structure of KBR, provided an overburden of 10 to 45 m w.e. depending on the solid angle on the experimental site. The experimental site at KBR is depicted on the left in Figure 2.2.1.

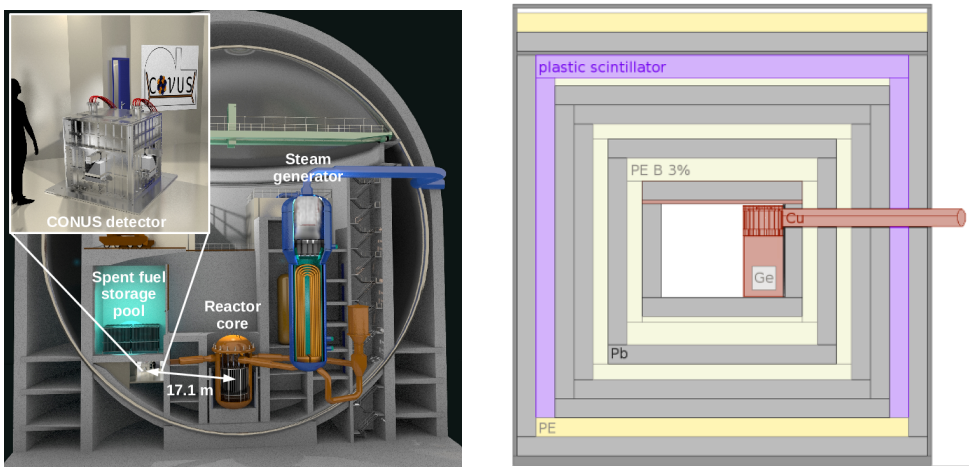

Figure 2.2.1: **Left:** Position of the CONUS experimental setup at the Brokdorf nuclear power plant. CONUS is located at a distance of 17.1 m from the reactor core centre. The spent fuel storage pool with the concrete structure provides an overburden of 10 to 45 m w.e. depending on the angle at the experimental site [48]. **Right:** Conus shield. The lead layers are coloured grey, the polyethylene layers are coloured light green and the plastic scintillators are coloured violet. A HPGe diode is marked in grey inside the copper cryostat in red [49].

CONUS used four p-type point-contact high-purity germanium spectrometers. In total, the detectors have an active mass of (3.73 ± 0.02) kg. Each detector is equipped with a low-vibration electrical cryocooler, as seen in Figure 2.2.2. The detectors fulfil all prerequisites needed for observing CEνNS at reactor sites. This includes ultra-low noise levels and thus ultra-low thresholds of 300 eV_{ee} in RUN-1/2 and 210 eV_{ee} in RUN-5. The achieved pulser resolution in terms of FWHM was always below 80 eV_{ee}[50]. The detectors are called C1 to C4.

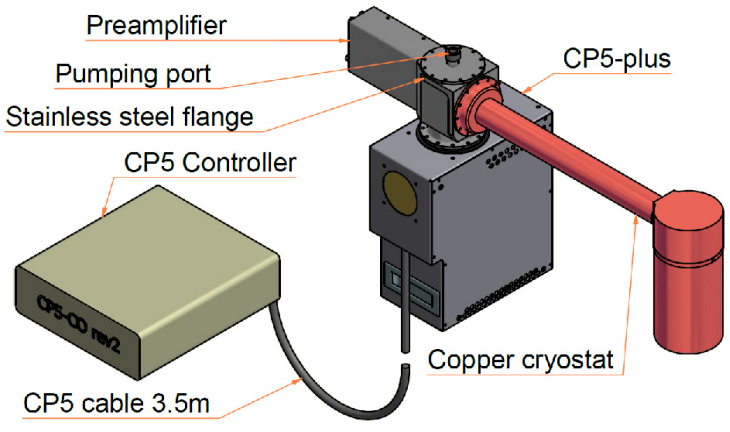

Figure 2.2.2: HPGe detector setup [50].

The most relevant background contributions to the region of interest (ROI) of CEνNS in RUN-1 and RUN-2 are summarised in Table 2.1. The μ-induced background is the largest contribution with almost half of the background. This background is mostly caused by secondary radiation within the lead shield, consisting of an electromagnetic component and more importantly neutrons. The majority of the muon-induced neutron flux is made up by fast neutrons, below 100 MeV, which engage in elastic and inelastic scatterings with the germanium nucleus, inducing nuclear recoils accompanied with and without γ-radiation. Contrasting this, thermal neutrons interacted dominantly via neutron capture, with germanium as the most relevant target material. The neutron capture produces additional products with half-lives extending CONUS μ-veto window, such as the metastable states ^{71m}Ge, ^{73m}Ge and ^{75m}Ge. Furthermore, neutrons produced by muons within the steel-enforced concrete of the building also induce recoils within the ROI.

The second largest contribution stems from the decay of ^{210}Pb, an isotope inherently contained by the CONUS shield and detector cryostats. ^{210}Pb within shield and cryostat make up almost 45% of the background in CONUS. To combat this background, the purity of the lead layer of CONUS increases towards the detector chamber, with parts of the innermost layer being composed of several decades old lead retrieved from the Freiburg Minster.

A quite small but still relevant source of background is air-borne radon, originating about 3.4% of background. Measures to mitigate the radon background included flushing of the detector chamber with radon-free gas. Additionally, the radon level within room A-408 was subject to constant monitoring. Typical activities were around 100 Bqm^{-3}.

Cosmogenic activation impacted CONUS by activating the Ge diodes and the Cu parts of the cryostat due to the high activation cross-section of the materials and the close distance to the reactor. The decays of ^{68}Ge and consecutively ^{68}Ga,^{71}Ge and ^{75}Zn are the only clear visible lines in the low energy range of the data. This makes up about 3% of the total background.

Within a very extensive study, the reactor correlated background was found to be negligible and is therefore not included in Table 2.1.

Source of background		Events in 0.4 to 1keV[$d^{-1}kg^{-1}$]	Fraction
Muon induced	Prompt μ-induced n in shield	$\sim$4.13	$\sim$40%
	Metastable Ge states	$\sim$0.04	$\sim$0.4%
	μ-induced n in concrete	$\sim$0.76	$\sim$7%
^{210}Pb induced	^{210}Pb in shield	$\sim$0.20	$\sim$2%
	^{210}Pb in cryostat	$\sim$4.48	$\sim$43%
Cosmogenic activation		$\sim$0.31	$\sim$3%
Airborne radon		$\sim$0.35	$\sim$3%
Total		$\sim$ **10 $d^{-1}kg^{-1}$**	

Table 2.1: Overview over the average relative contributions of the different background sources. Values taken from [51]. Almost half of the background is caused by muons and muon-induced showers.

As the background suppression is critical for the experiment's success, CONUS employed both active and passive shielding. The onion-like shielding layers are shown on the right in Figure 2.2.1. Beginning with passive shielding, this sketch depicts layers of lead in a light grey colour. The lead shield has a total width of 25 cm and is used to suppress and shield against environmental activity.
Another part of the passive shielding are the borated and pure polyethylene layers shown in light yellow. Muons are expected to create both secondary electromagnetic radiation and neutrons. The polyethylene layers' task is to moderate and shield against these neutrons.
The active shielding comprises a muon veto, consisting of nine layers of plastic scintillator plates marked in violet in Figure 2.3.1. Each plate is equipped with PMTs to detect scintillation light. Since plastic scintillators are also sensitive to γ-rays, the muon veto was placed inside the outermost lead layer, thereby reducing γ radiation hitting the scintillators. For each signal in the μ-veto, a constant veto window is opened up in which events inside the germanium crystals are rejected. In the CONUS shield, passive and active shielding achieved a total background suppression of four orders of magnitude [51].
Furthermore, on the right in Figure 2.2.1 one of the four HPGE diodes is marked in grey inside the copper cryostat depicted in red. The cryostat arms are transferred to the inner detector chamber through holes in the shielding layers.

2.3 CONUS+

The CONUS+experiment was installed in the Leibstadt nuclear power plant (KKL) [52], Switzerland, in the summer of 2023. The annual electricity produced at KKL is about 9753 GWh which represents 14% of Switzerland's annual power consumption. The reactor of KKL is a boiling water reactor with a thermal power of 3600 MW. It operates at a high-duty cycle, leading to an annual outage of one month known as reactor off-time in which general reactor maintenance is done and fuel elements are refilled.

CONUS+ is located in room XR-20 at a distance of 20.7 m to the reactor core centre. At this position an electron antineutrino flux of $1.45 \cdot 10^{13} \mathrm{s}^{-1} \mathrm{cm}^{-2}$ is expected. The concrete structure of KKL provides an average overburden of 8 m w.e.

The previously described CONUS detectors were refurbished to improve several aspects. The point contact size was reduced improving the pulser resolution to below 55 eV. Other changes include new preamplifier electronics based on ASIC to enhance the trigger efficiency. A water cooling system for the cryocooler of the model Julabo 500 [53] replaced the previous fan system in an effort to reduce vibrations and therefore microphonic noise.

CONUS+ uses the former CONUS detectors C2, C3 and C4. The C1 detector was exchanged with a HPGe-spectrometer of the same design called C5. The background at the new experimental site at KKL is already characterised. Some of the measurements, their methods and results will be presented in the next chapter (see chapter 3).

The CONUS+ detector is using a modified version of the CONUS shield. One of the main modifications is the exchange of an inner lead layer with an additional muon veto which is depicted in Figure 2.3.1. The CONUS+ shield has in total 20 cm of lead, 5 cm less than CONUS. How this potentially impacts the shield performance will be discussed in chapter 4. Furthermore, the CONUS+ detector was reinforced with a stainless steel cage to fulfil the severe safety restrictions, due to the large risk of earthquakes in Leibstadt.

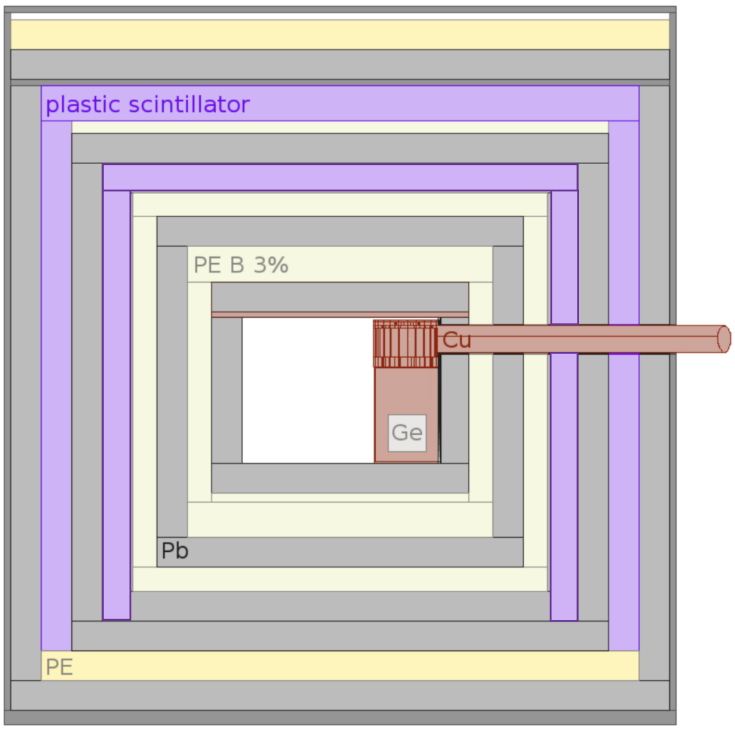

Figure 2.3.1: Side view of the CONUS+ shield geometry. The lead layers are coloured grey, the polyethylene layers are coloured light green and the plastic scintillators are coloured violet. A HPGe diode is marked in grey inside the copper cryostat in red. Modified picture from [49].

This Master's thesis work encompasses the characterisation of the muon background on-site in KKL and the design and commissioning of the new inner muon veto of CONUS+. The design of the muon veto for CONUS+ will be presented in the next section.

2.4 Design of the muon veto for CONUS+

At the former CONUS location an average overburden of 24 m w.e. was achieved through the unique situation of the experimental site being situated directly underneath the spent fuel storage pool. At the new location in KKL, this was however not possible, hence the overburden is only 8 m w.e.. As the reduction of cosmic radiation scales with depth, CONUS+ will face a much higher muon flux than CONUS.
To keep a similar background level the muon rejection efficiency of the CONUS shield of $\sim$97% has to be increased to over 99%. This motivated the introduction of an additional muon veto layer. In this section, I will describe in detail the design of the muon veto for CONUS+ and explain the principle of operation of its components.

A scintillator is a material that exhibits scintillation, the property of luminescence when excited by ionising radiation as for example muons. CONUS+ has two layers of plastic scintillators, an outer and an inner muon veto layer. Each layer is composed of nine plates of EJ-200 plastic scintillator by Scionix [54]. The material EJ-200 was chosen for its overall good properties such as long optical attenuation length, high light yield and fast timing. Both muon vetos have a quadratic top plate and the sides consist of two stacked scintillator plates. To accommodate for the cryocooler arms the top side layers have semicircular openings. Figure 2.4.1 shows on the left the design and on the right a photo of the new inner muon veto.

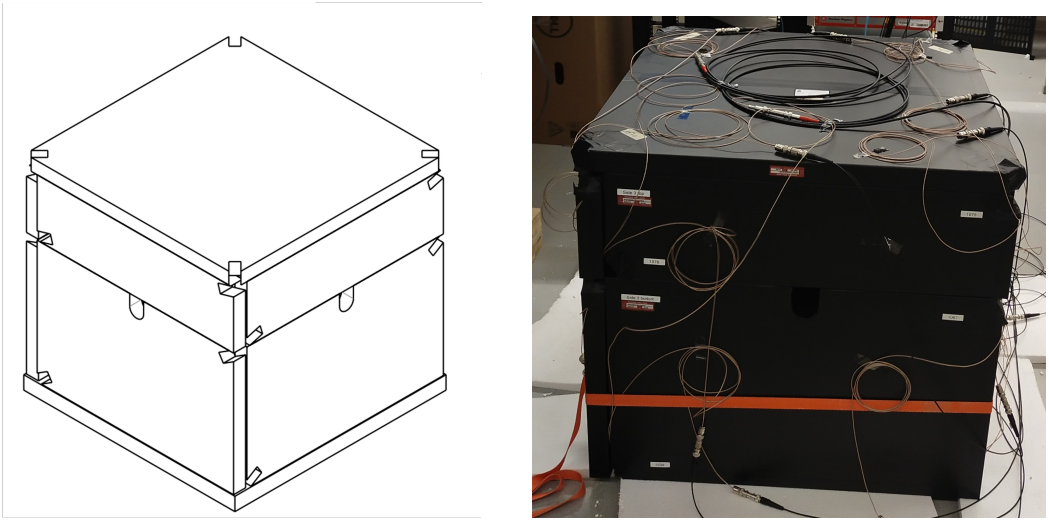

Figure 2.4.1: **Left:** Design of the plastic scintillator plates for the muon veto, exemplary for the inner veto. The semicircular openings in the side plates are to accommodate the cryocooler arms. In the recesses in the scintillator plates are the PMTs installed. **Right:** Picture of the inner muon veto assembled at the MPIK.

The plates are covered with black non-transparent film, which is strengthened with black tape where the PMTs are installed. This ensures that no visible light hits the scintillator material, as a potential leak could cause a dominating background signal rendering the muon veto inoperable. The produced scintillation light in the muon veto plates is collected by photomultiplier tubes (PMTs). They are installed in the recesses in the design drawings of Figure 2.4.1.

PMTs, multiply the current produced by incident light in multiple dynode stages. The PMT is a vacuum tube containing a photocathode, several dynodes, and an anode. The construction of a PMT can be seen in Figure 2.4.2. When incident photons strike the photocathode electrons are ejected due to the photoelectric effect. These electrons are directed with the focusing electrode towards the electron multiplier. Here, the electrons are accelerated towards the dynodes due to an electric field, producing secondary electrons. Finally, the electrons are collected by the anode.

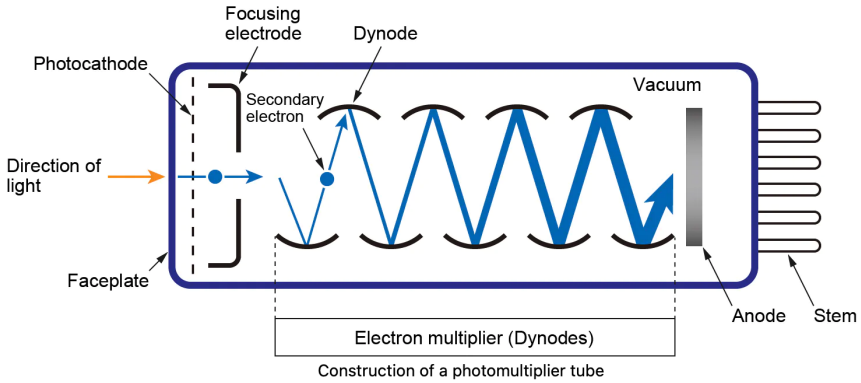

Figure 2.4.2: Construction of a PMT. Figure taken from [55].

Among the most interesting characteristics of a PMT is its gain and dark current. The gain, also called current amplification, is given by

$$\mu = \alpha \cdot \delta^n = \alpha \cdot AV^{kn}. \tag{2.2}$$

V is the supply voltage, and α is the collection efficiency, the probability that the initially produced photoelectron will hit the effective area of the first dynode. δ is the secondary emission ratio. k is determined by the structure and material of dynode and n is the number of dynode stages. A is a constant.

Dark current is the relatively small electric current that flows through photosensitive devices such as a photomultiplier tube, even in the absence of light. The dark current signal is due to thermal emissions of electrons from the photocathode, leakage current between dynodes, as well as stray high-energy radiation. This rate varies from one PMT to another and has to be tested for each PMT.

Another important characteristic of a photocathode is its sensitivity typically described by its quantum efficiency QE. In general, quantum efficiency is defined as the probability for the conversion of incident photons to an electrical signal defined as:

$$QE = \frac{\text{Output electrons}}{\text{Incident photons}}. \tag{2.3}$$

The quantum efficiency depends on the wavelength of the photons.
In both the outer and inner muon veto, each side layer contains two PMTs and the top layer, being the most important, is equipped with four PMTs.
In the commissioning of CONUS, each PMT in the outer muon was tested and given an optimal position inside the CONUS shielding as can be seen in Figure 2.4.3. The outer muon veto utilises PMTs of the model R11265U-200 [56] by Hamamatsu with a QE of 43% at 400 nm.

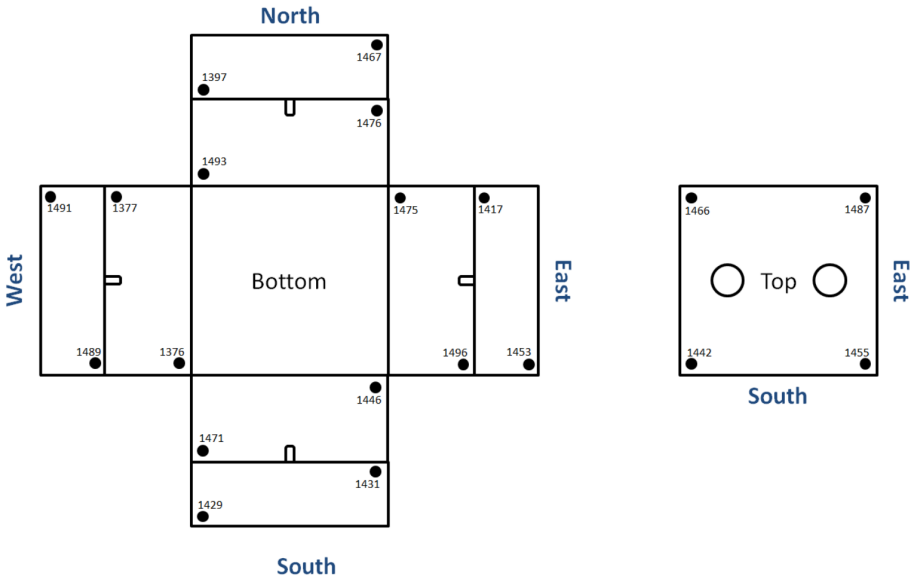

Figure 2.4.3: Position of the PMTs inside the scintillator plates in the CONUS+ shielding. Side layers are equipped with two PMTs in case one is no longer functional. Four PMTs are installed in the top layer for optimal background rejection. Figure taken from [57].

Since the new inner muon veto is closer to the detector chamber, low background PMTs from the R8520-406 [58] series by Hamamatsu were selected to reduce possible background from the PMTs themselves. They have a *QE* of 25% at 420 nm and were formerly used by the XENON1T [59] dark matter experiment. The inner PMTs were tested in the commissioning process of CONUS+. In section 5.1, I will elaborate on the tests performed and their results.

Both the scintillators and the PMTs are made up of radiopure material. The scintillator plates were screened at the MPIK, and the inner PMTs and their bases were previously screened by the XENON collaboration [60]. The material contamination numbers of the inner muon veto are collected in Table 2.2. Among these components, the PMTs exhibit the highest activities, with potassium accounting for the largest contribution. However, as the PMTs and bases only have a combined mass of $\sim$27.9 g each, they do not pose a significant background in CONUS+. The potential background caused by the materials of the muon veto in CONUS+ will be further examined in section 4.4.

Muon veto part	Isotope	Activity [mBq/kg]
Inner muon veto plates	^{226}Ra	0.09 ± 0.05
	^{228}Th	0.5 ± 0.1
	^{40}K	1.5 ± 0.5
	^{228}Ra	0.4 ± 0.1
Inner muon veto PMTs and bases	^{226}Ra	12.9 ± 2.5
	^{228}Th	13 ± 3
	^{40}K	< 221
	^{228}Ra	< 15

Table 2.2: Radiopurity of inner muon veto. The radiopurity numbers of inner muon veto PMTs were taken from [60].

Additionally, the data-taking acquisition system of CONUS was upgraded. Previously, only the veto rate was saved, limiting the analysis. In the new muon veto of CONUS+, a new analog-to-digital converter (ADC) of the model V1740D [61] is used to record the energy spectra for each PMT. In offline analysis, veto coincidence can then be applied to reject muon-induced events. This upgrade optimises the rejection efficiency and reduces the dead time.

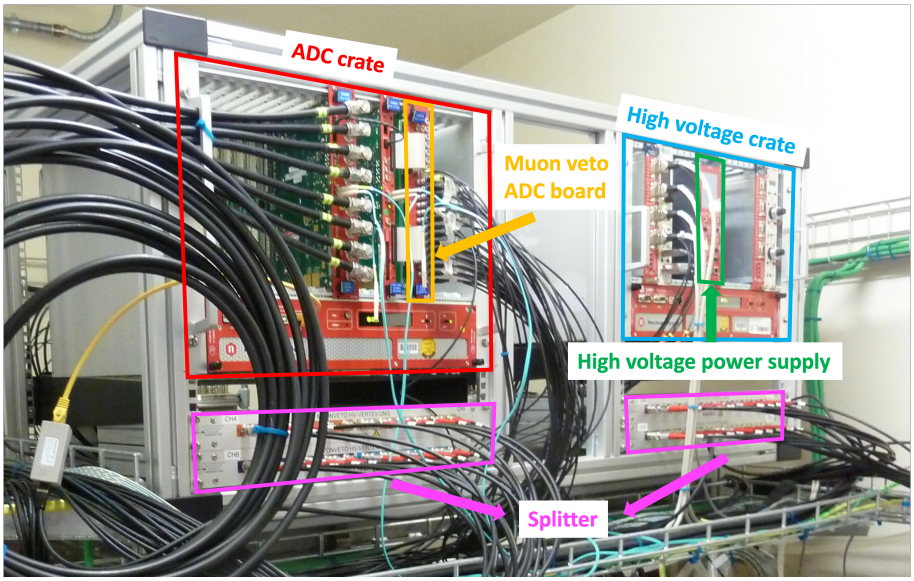

Figure 2.4.4: Setup of the muon veto and germanium detector of CONUS+. The ADC crate is on the left and on the right is the high-voltage crate.

Figure 2.4.4 shows the electrical setup in KKL. This setup involved a 8-channel N8033 [62] power sup-

ply by caen (marked in green) which was connected to 8 splitters with 6 channels (marked in pink). The PMTs high voltage connections were separated over the splitters, giving each PMT the best voltage for its operation. The yellow box marks the ADC board connected with the signal cables of all PMTs.

Prior to the new veto design, the gamma and muon background was measured on-site in KKL. The next chapter will present the measurement campaign and its conclusion for the design of the new muon veto for CONUS+.

Chapter 3

Gamma and Muon flux measurement

A series of measurements of the gamma and muon flux were conducted on site of the nuclear power plant Leibstadt.
The measurements of the gamma radiation will provide valuable insights into possible additional shielding requirements of the CONUS+. Of particular interest is the comparison of the gamma-ray flux at KKL with the flux measured at KBR.
The muon flux measurements were conducted to evaluate the background at KKL and to probe whether CONUS+ requires a muon veto upgrade. Notably, the XR-20 room in KKL has an average overburden of approximately 8 m.w. contrasting the substantial 24 m w.e. overburden present in KBR. This discrepancy in overburden levels suggests an anticipated increase in the atmospheric muon flux.

The chapter starts with the measurements of the gamma spectrum, which includes a brief introduction to the CONRAD detector. We then discuss the muon flux measurements, with more details on the liquid scintillator module used and the principles behind organic liquid scintillators. Finally, the measurements conducted at KKL will be examined.

3.1 CONRAD detector

The CONRAD [63] detector is a low background high purity germanium spectrometer featuring a diode with an active mass of 2.2 kg that ensures a high detection efficiency. This allows the detector to characterise background radiation in an energy range of 60 keV to 12 MeV.

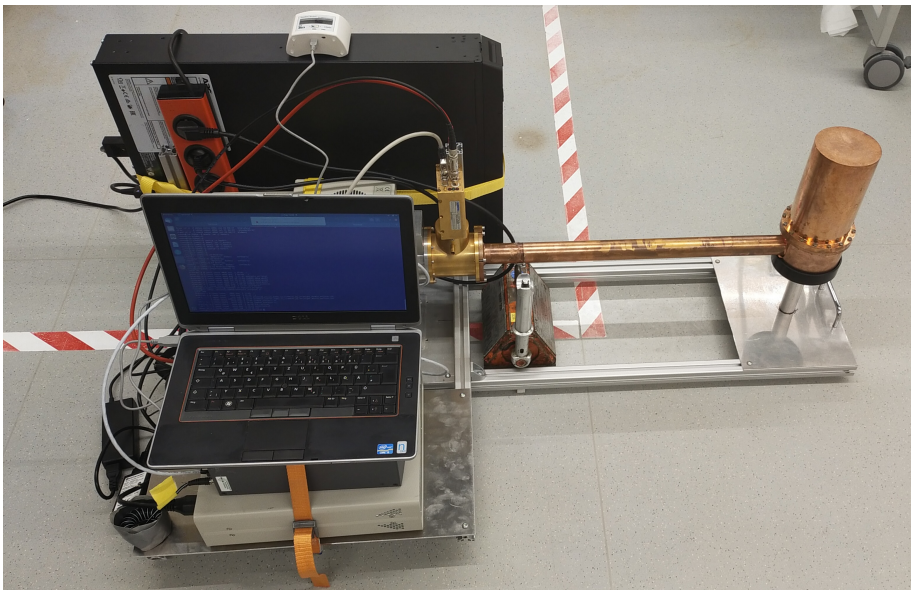

Figure 3.1.1: CONRAD detector and DAQ setup.

Manufactured at MIRION TECHNOLOGIES (Canberra Olen), the CONRAD detector consists of a semi-coaxial Ge diode in a radiopure copper (Cu) housing. CONRAD is equipped with electric cryocooling, allowing high mobility of the detector and eliminating the need for liquid nitrogen, thus rendering it suitable for use at reactor sites. The detector has a resolution of 2.5 keV FWHM and an energy threshold of $\sim$57 keV.

In the measurements performed in KKL, a DAQ setup consisting of a LYNX1 [64] module and an uninterruptible power supply system (UPS), for voltage stability, was used. The detector and DAQ setup are shown in Figure 3.1.1. The CONRAD detector was calibrated with external sources periodically, guaranteeing stability in energy gain.

3.2 Gamma measurement at KKL

In reactor shielding studies, understanding the spectral distribution of gamma radiation is important. In nuclear reactors, gamma radiation is emitted by many different sources. At MeV scale, these sources include prompt gamma rays that are emitted within 5×10^{-8} s of fission, gamma radiation of products of thermal fissions and gamma rays from neutron capture. Gamma rays with lower energies under 1 MeV are emitted in the inelastic scattering of ^{238}U, capture in construction materials and the disintegration of capture products. For more detail refer to [35].

Measurements were performed at different positions and collection times within room XR-20. The gamma-ray flux data obtained is depicted in Figure 3.2.1. The gamma peaks were labelled with their corresponding isotope. At lower energies, contributions from the Th and U decay chains as ^{208}Tl are visible. ^{40}K and

^{60}Co were found as well. Above 2.7 MeV, thermal power contributions dominate. The strongest γ lines are created in the decay of ^{16}N. This isotope is formed in the cooling water flowing through the reactor core in a nuclear power plant. It is produced predominantly in (n,p) reactions on ^{16}O and decays with a short half-life of 7.13 s via beta decay. This decay is accompanied by the emission of very energetic gamma rays. The activation of ^{16}O results from a threshold reaction requiring neutron energies over 10 MeV [65]. Other strong contributions were identified as neutron capture on ^{56}Fe, ^{55}Fe and ^{63}Cu.

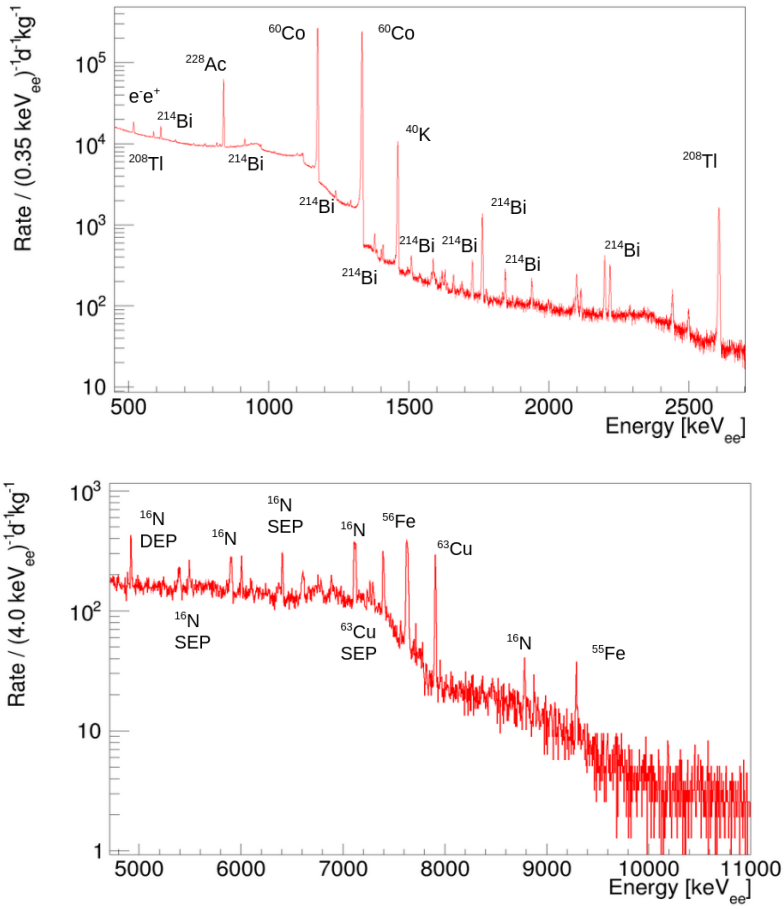

Figure 3.2.1: Gamma spectrum measured by CONRAD in KKL. The gamma peaks were labelled with their corresponding isotope.

In a previous measurement, CONRAD measured the gamma spectrum in Brokdorf [49]. The recorded spectrum at KBR is depicted in Figure 3.2.2. Interestingly, the contribution of high energy gammas in KKL over 2.7 MeV, was found to be a factor 25 smaller than in KBR. Moreover, when comparing the spectra at lower energies, there is clearly a more pronounced presence of ^{60}Co at KKL. Furthermore, at higher energies, the KKL spectrum exhibits a stronger gamma contribution stemming from neutron capture in iron.

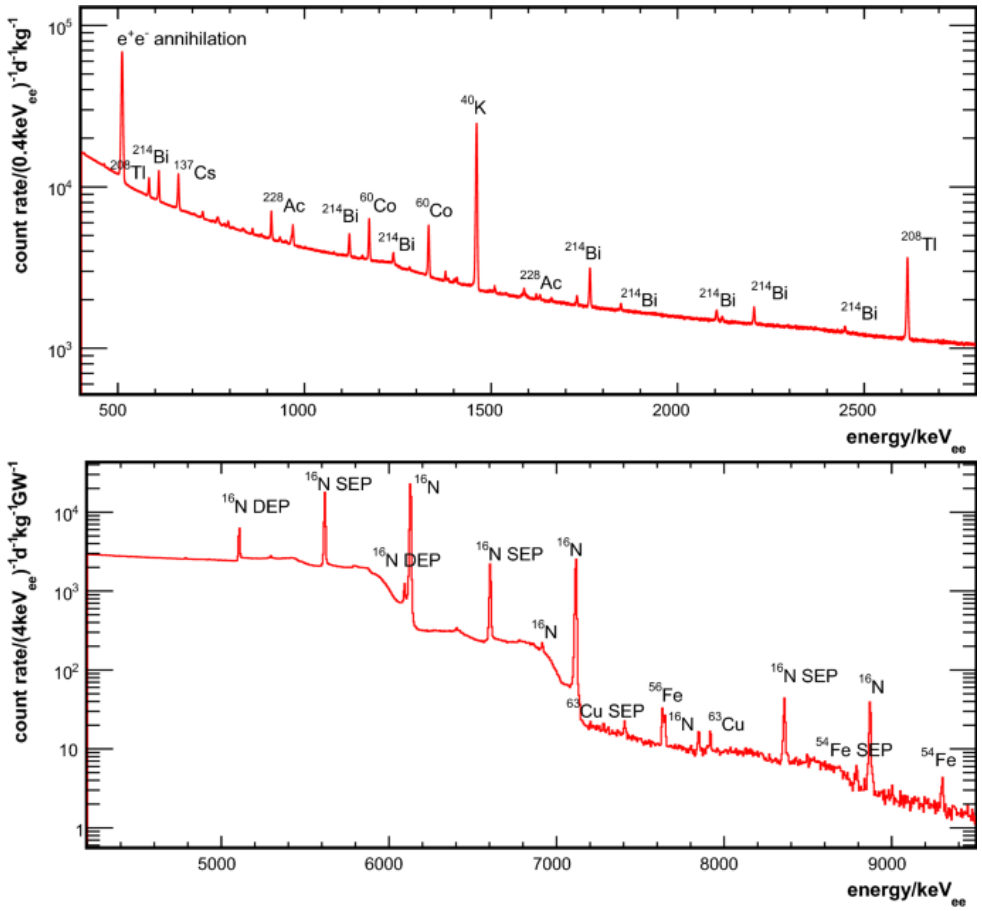

Figure 3.2.2: Gamma spectrum measured by CONRAD in KBR. The gamma peaks were labelled with their corresponding isotope [49].

Measurements with the CONRAD detector provided extensive knowledge of the gamma radiation spectrum at the new experimental location in KKL. As however almost half of the background in CONUS is caused by muon-induced events, the characterisation of the muon spectrum at KKL and its comparison with KBR will be discussed in the next section.

3.3 Experimental setup for muon flux measurements

The muon flux in KKL was measured with a setup consisting of several components including a liquid scintillator module, a high-voltage power supply, an analog-to-digital converter (ADC) and a computer.

3.3.1 Liquid scintillator module

The scintillator module is composed of a liquid container with a capacity of 117 ml and a photomultiplier tube.

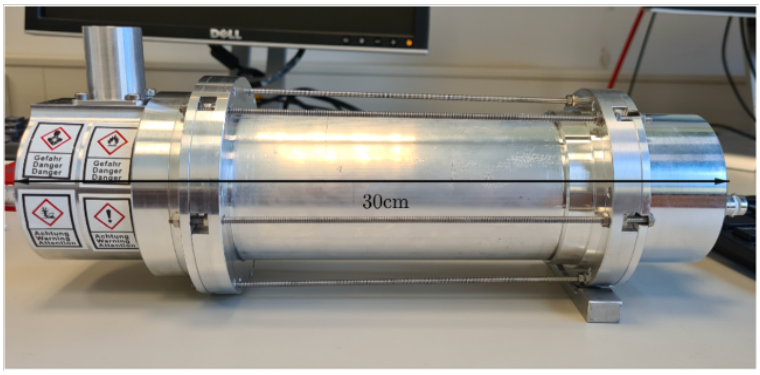

Figure 3.3.1: Liquid scintillator module [66].

The liquid container holds the liquid scintillator fluid, ensuring an airtight and lightproof environment. The cylinder cell has an inner diameter of 5.1 cm. A UV-transparent glass plate separates the liquid from a 2" photomultiplier tube of the 9954B [56] model with a borosilicate window. The PMT has a quantum efficiency of about 28% at peak and a spectral range of 290 to 680 nm [56]. Furthermore, optical coupling is used between the window and the PMT.

The container is filled through a chimney on top of the vessel. Once after filling, the container is bubbled, which is typically performed using nitrogen or argon to enhance the scintillator efficiency by minimising the oxygen content, which acts as a quenching molecule reducing the light yield. This process takes about 10 minutes. The vessel is constructed from PTFE, guaranteeing a high reflectivity, encased in an aluminium-magnesium alloy housing.

For these measurements, the commercially available scintillator liquid Ultima Gold F, with diisopropylnapthalene (DIN) as a significant component, was chosen for its fast response, high light yield and good pulse shape discrimination properties. More detail on pulse shape discrimination will be provided in section 3.4.

3.3.2 DAQ system and power supply

The CAEN V1725 [67] module serves as an ADC, transforming the analog signal received from the PMT into a digital format. The optimal power supply voltage was determined to be 1.1 kV to reduce saturation. This setting was maintained throughout all measurements.

The data was saved on the computer through the commercial software CoMPASS [68]. The software enables concurrent acquisition of energy, timing, and PSD spectra.

CoMPASS allows for customisation of various parameters, such as signal recorded length (gate) and the time before the trigger called the pre-gate and the DC offset. The software output is saved in the ROOT [69] format.

3.4 Organic liquid scintillators

Essential for understanding the operation of scintillator module is to understand how organic liquid scintillators produce light. When charged particles cross a scintillating medium, they primarily lose energy via electromagnetic interactions. Then, the electrons within the medium, instantaneously feel an intense electric field, leading to either molecular excitation or ionisation. In the context of organic liquid scintillators, a fraction of the de-excitation energy is released in the form of photons.

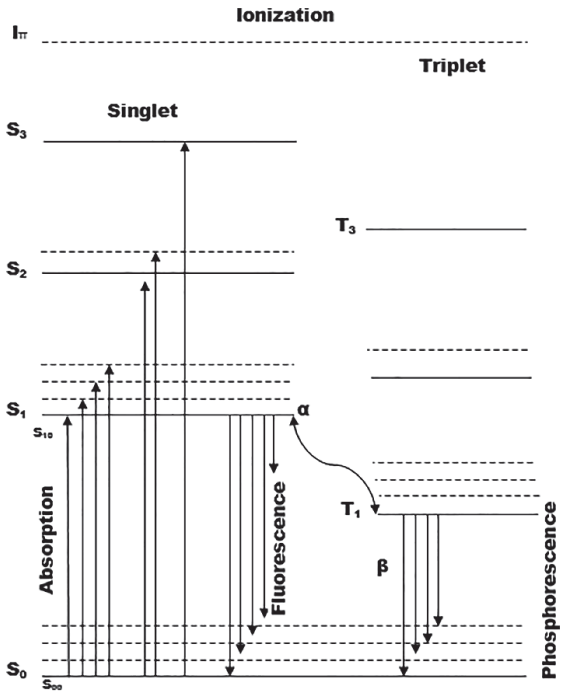

Figure 3.4.1: Energy diagram for π-orbitals. Figure taken from [70].

A more precise description of the energy transfer can be provided using Figure 3.4.1, an energy diagram for π-orbitals. Upon excitation, the molecule rapidly dissipates energy through collisions with neighbouring molecules until it reaches the S_1 level. In the transition between S_1 to S_0 fluorescence light is promptly emitted.

However, approximately 75% [71] of ionised molecules recombine in triplet states, which have various de-excitation paths available. The transition process from T_1 to S_0 is called phosphorescence and is highly forbidden. Hence, this transition process occurs over a time scale of microseconds or longer. Another path involves the production of indirect delayed luminescence through $T_1 \rightarrow S_1 \rightarrow S_0$. The molecule either acquires sufficient energy to return to S_1 or collisions among T_1 molecules lead to excitation via:

$$T_1 + T_1 \rightarrow S^* + S_0 \rightarrow S_0 + S_0 + \text{photons}. \tag{3.1}$$

In both scenarios, light is emitted with a time delay compared to direct emission. The ratio of Prompt/Delayed

fluorescence depends on excitation type and density. For particles with higher energy deposition dE/dx, the probability of Equation 3.1 is greater. Consequently, the slow component's amplitude is increased for particles such as protons, neutrons and alpha particles compared to electrons and muons. This characteristic enables the separation of particle types through pulse shape analysis, as illustrated in the comparison between fast neutrons and gammas in Figure 3.4.2.

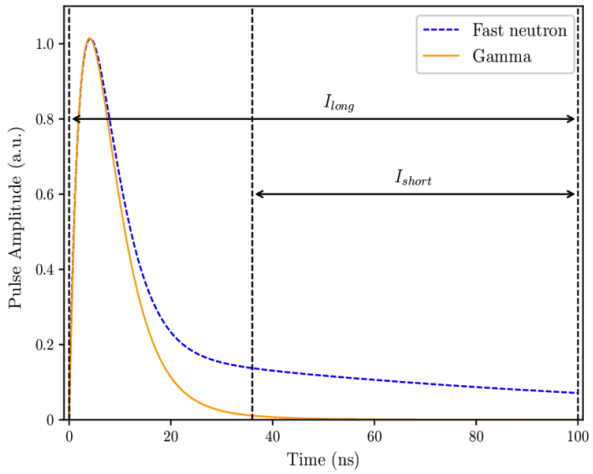

Figure 3.4.2: Schematics of pulse shape for a gamma and neutron. Due to a higher dE/dx, the slow component of the neutron pulse is larger than that of the gamma pulse. Figure taken from [72].

The method known as tail-to-total compares the integrated signal over two different intervals, one being the whole signal and one only the tail. The separation parameter is the ratio of the charge in the tail Q_{tail} to the whole signal Q_{tot}:

$$\text{PSD} := \frac{Q_{tail}}{Q_{tot}}. \tag{3.2}$$

3.5 Measurements at MPIK

Measurements using the liquid scintillator module were conducted at the MPIK to calibrate the scintillator module and measure the muon flux in an outdoor environment. The MPIK is situated at about 300 m above sea level [73] a similar height to the nuclear power plant in Leibstadt. As a result, a comparable muon rate can be expected at both locations.

3.5.1 Calibration with ^{137}Cs source

To relate ADC channels in the output root files to their corresponding energy, it is necessary to perform an energy calibration measurement of the liquid scintillator detector. A reference point with a known energy in the spectrum is needed for calibration. In this case, the Compton edge of a 370 kBq ^{137}Cs source was chosen.

With a half-life of approximately 30 years, ^{137}Cs primarily decays via beta emission to a metastable nuclear isomer of barium, ^{137m}Ba, which has a half-life of roughly 153 seconds. The decay of ^{137m}Ba to its ground state ^{137}Ba involves the emission of photons at an energy of 0.6617 MeV. The second decay mode directly populates the ground state ^{137}Ba, accounting for about 5% of all decays [74]. The decay modes are visualised in Figure 3.5.1

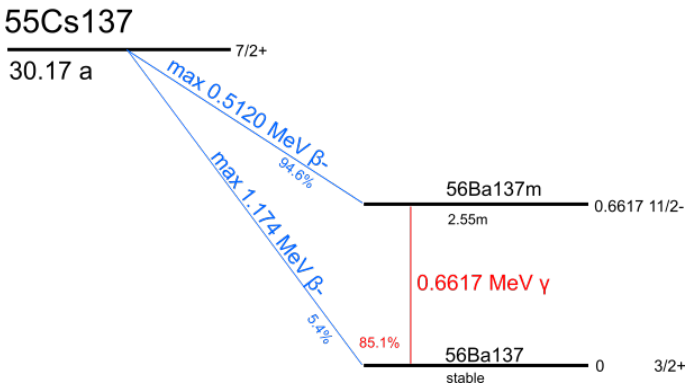

Figure 3.5.1: Decay scheme of ^{137}Cs. About 95% of decays happen via beta decay to the metastable isomer ^{137m}Ba. The decay of the isomer to its ground state is responsible for all gamma emissions in the ^{137}Cs spectrum.

The Compton edge E_c corresponds to the highest energy that can be deposited, indicating full backscatter of the photon. The edge value E_c for ^{137}Cs can be calculated as follows:

$$E_c = E_\gamma \left(1 - \frac{1}{1 + \frac{E_\gamma}{m_e c^2}(1 - cos(\theta = 180°))} \right) \approx 478 keV. \tag{3.3}$$

with the photon energy E_γ, in this case 0.6617 Mev, and m_e the mass of an electron.
However, the Compton edge is influenced by statistical effects such as fluctuations in the amount of photons,

photoelectrons and the baseline of a pulse. This smearing effect can be described by a Gaussian normal distribution

$$G(E) = \frac{1}{\sqrt{2\pi\sigma^2}} exp\left(-\frac{E^2}{2\sigma^2}\right) \tag{3.4}$$

with standard deviation σ and energy E. The expected measured spectrum $R(E)$ emerges from a convolution of the ideal Compton spectrum $r(E)$ and the Gaussian normal distribution $G(E)$. The ideal Compton spectrum is described by the parameters *a*,*b* and *c*:

$$r(E) = \begin{cases} aE^2 + bE + c & E \leq E_c \\ 0 & E > E_c. \end{cases} \tag{3.5}$$

This leads to the recorded spectrum:

$$R(E) = r(E) \circledast G(E) = \int_{-\infty}^{\infty} r(x)G(E-x)dx = \alpha_1 Erfc\left(\frac{E-E_c}{\sqrt{2}\sigma}\right) + \beta_1 exp\left(-\frac{(E-E_c)^2}{2\sigma^2}\right). \tag{3.6}$$

Here, $Erfc(x)$ denotes the complementary error function given by

$$Erfc(x) = 1 - Erf(x). \tag{3.7}$$

The remaining parameters are given by $\alpha_1 = \frac{1}{2}[a(E^2+\sigma^2) + bE + c]$ and $\beta_1 = \frac{-\sigma}{\sqrt{2\pi}} a(E_c + E) + b$.

Simulations show that the theoretical E_c corresponds rather accurately to the experimental energy at which the falling flank crosses 66% to 89% of the height of the maximum [75]. As the optimum value can vary based on the scintillator and detector, the value of 70% was selected as it was obtained for this specific scintillator module in the Bachelor's thesis by Moritz Raab [66].

The recorded spectrum $R(E)$ was fitted to the Compton edge of the ^{137}Cs spectrum, as shown in Figure 3.5.2.

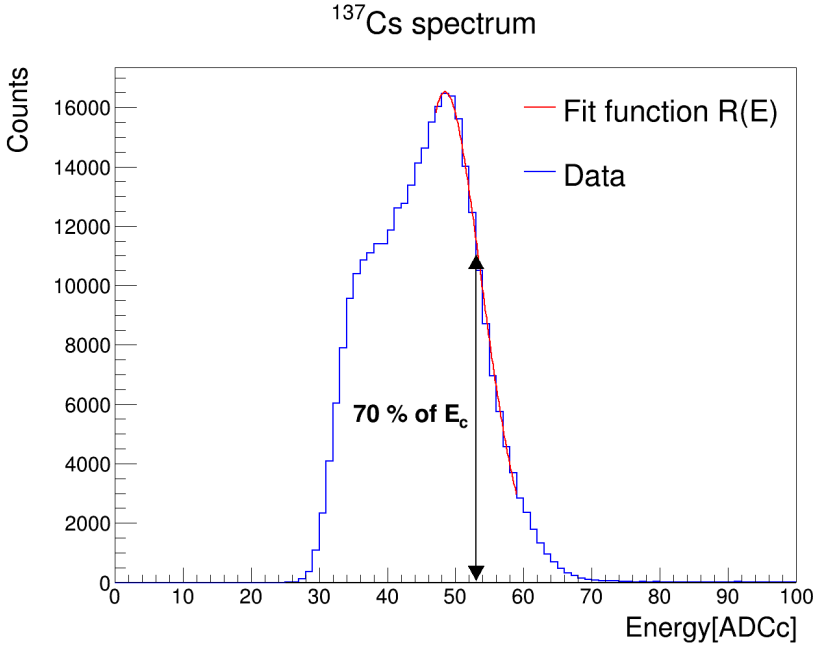

Figure 3.5.2: Measurement of ^{137}Cs spectrum with the scintillator module. The recorded spectrum $R(E)$ is fitted in red to the measured Compton edge of the ^{137}Cs spectrum.

From this figure, it is clear that 53.28 ± 0.22 ADC counts correspond to the ^{137}Cs Compton edge ($E_c = 478$ keV), resulting in a calibration factor of

$$f_1 = \frac{E_{exp}}{E_c} = \frac{53.28 \pm 0.22 \text{ ADC}}{478 \text{ keV}} \approx 0.1115 \pm 0.0005 \text{ ADC/keV}. \tag{3.8}$$

3.5.2 Measurement outdoors

The outdoor measurements were performed next to a building at the MPIK. The spectrum acquired during 4 h data taking is shown in Figure 3.5.3.

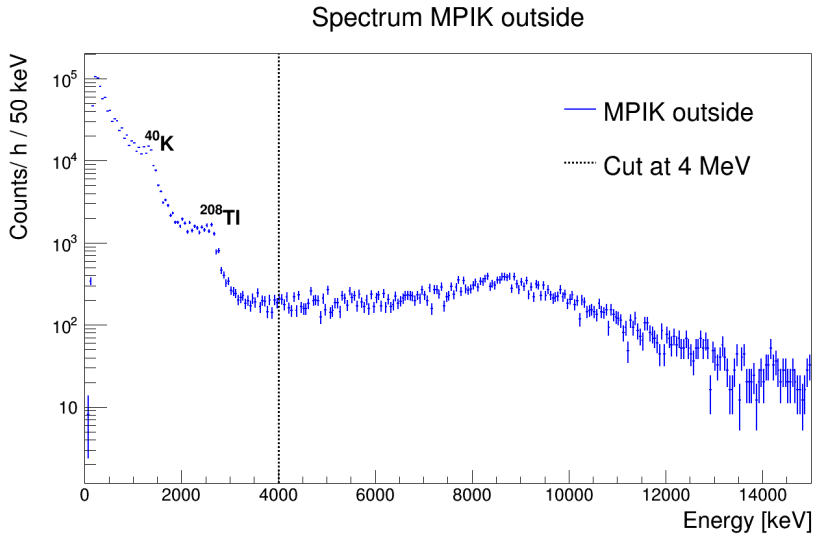

Figure 3.5.3: Spectrum at the MPIK outside. The first peak corresponds to the Compton edge of ^{40}K and the second peak to the Compton edge of ^{208}Tl.

The initial peak on the left in Figure 3.5.3 corresponds to the Compton edge of ^{40}K with $E_\gamma = 1460.8$ keV and $E_c = 1243.3$ keV. Adjacent to ^{40} K is the Compton edge of ^{208}Tl with $E_\gamma = 2614.5$ keV and $E_c = 2381.8$ keV.

In order to estimate the rate of muons, environmental gamma radiation has to be eliminated by cutting the spectrum at 4 MeV. For further background reduction, the tail-to-total method is used to cut neutron-induced events. This method is applied by dividing the signal in the tail by the total integrated charge E_{total}. The charge in the tail is defined as E_{total} minus the signal acquired in the first 40 ns, E_{short}.

The PSD parameter is defined as follows

$$PSD = \frac{E_{total} - E_{short}}{E_{total}}. \tag{3.9}$$

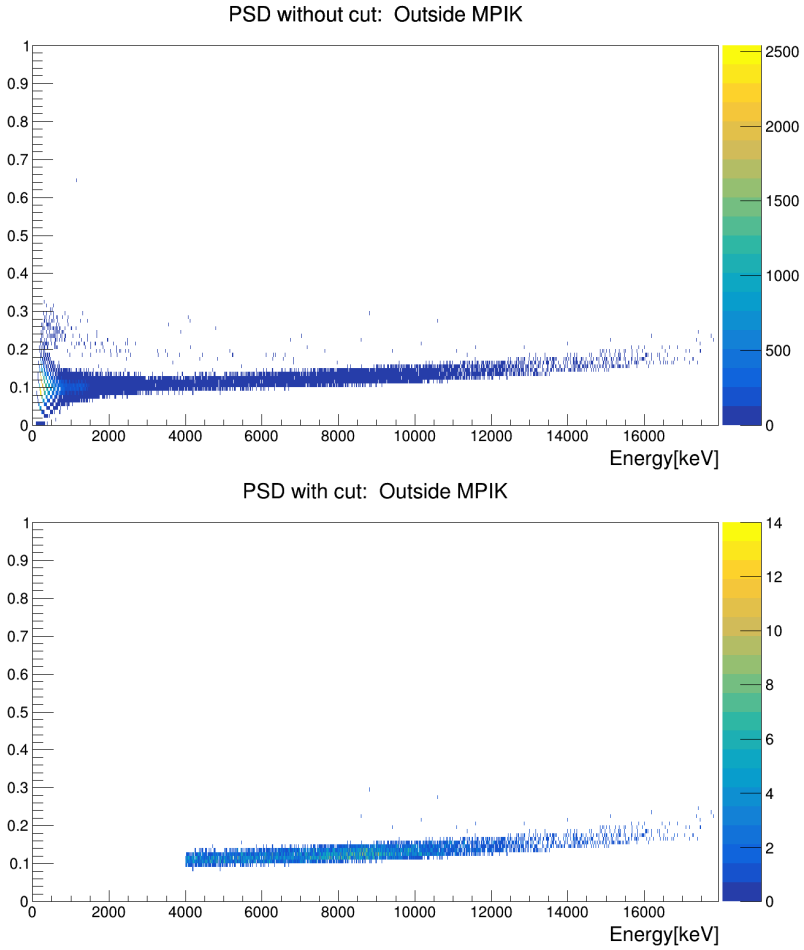

Figure 3.5.4: **Top:** PSD before cut. The upper band is inhabited by neutron events. **Bottom:** PSD after cut. Neutron events and background radiation have been removed. The band is moderately arched, indicating that some pulses were saturated during the measurement.

The upper image of Figure 3.5.4 illustrates the PSD plot without any cut. A small upper band is evident, produced by neutron events. Muon events inhabit the predominant lower band. The bottom figure of Figure 3.5.4 depicts the PSD plot after applying both energy and PSD cuts. The remaining spectrum corresponds to only muon events. Contrary to expectation the band is not entirely flat but shows a slight curve. This indicates that some pulses were saturated during the measurement, distorting the PSD, without affecting the measurement.

The total muon rate measured by the liquid scintillator module is:

$$\text{Rate(MPIK outside)} = 0.6187(^{+0.0013}_{-0.0007})_{\text{syst}}(\pm 0.0065)_{\text{stat}}\ \text{Hz}. \tag{3.10}$$

The systematic error is obtained from the fit. Since the liquid scintillator container is a cylinder, it is difficult to express the measured rate in Hz/m^2. Simply taking half the surface area of the container, approximately

56.5 cm^2, results in a rate of about $\sim 109.50(^{+0.23}_{-0.12})_{\text{syst}}(\pm 1.15)_{\text{stat}}$ Hz/m^2. This is lower than the expected muon flux at the MPIK of roughly $f_{Lit} = 200$ Hz/m^2 [28]. An alternative approach involves considering the building surrounding the measurement site. This makes it reasonable to assume that muons with an incident zenith angle over 50 degrees were not detected. With this assumption, the cross-section is 31.42 cm^2, which is equivalent to a flux of about 197 Hz/m^2. This is a pure approximation, however, it reproduces the expected muon flux well. A full Monte Carlo simulation to probe this effect will be developed in the future. From here on out, the muon rate measured outside is assumed to be 200 Hz/m^2.

3.6 Measurements in KKL

The muon rate was measured within the nuclear power plant in Leibstadt both during reactor operation, ON-time, and during reactor outage, OFF-time.

3.6.1 Measurements during reactor ON-time

During reactor operation, measurements were taken at four different positions in XR-20. The specific locations are indicated in Figure 3.6.1. Notably, position five resides within the CONUS+ position, making the rate at this position most relevant for estimating the muon flux for CONUS+.

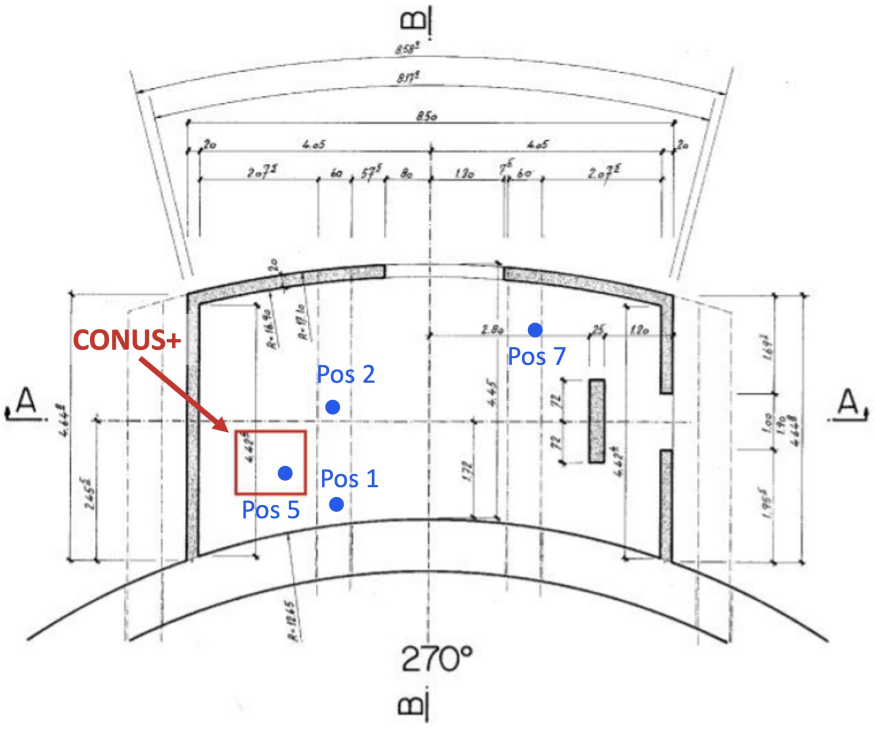

Figure 3.6.1: XR-20 room at KKL. Muon rate was measured at positions 1,2,5 and 7. Position 5 corresponds to the CONUS+ location.

The initial energy cut at 4 MeV proved insufficient for filtering background radiation during reactor operation because nuclear reactors generate an additional high energy gamma background [35]. As the measurements with the CONRAD detector revealed a gamma background extending up to the last measured line of ^{55}Fe at 9.3 MeV, an energy cut at 10 MeV was chosen. This corresponds to selecting muons with an incidence zenith angle over 30 degrees. Therefore, these rates can not be directly compared to rates obtained with an energy cut at 4 MeV.

Results presented in Table 3.1 demonstrate that position seven exhibits the lowest muon rate, followed by position five. This outcome aligns with the expectations, as increased overburden due to proximity to the concrete wall will likely reduce the muon rate. A comparison to the MPIK spectra suggests an additional background due to the presence of ^{60}Co. This was also observed in the measurement of the gamma radiation with CONRAD (see section 3.2). Position five, having the second lowest muon rate, proves that CONUS+ is well situated within room XR-20.

Position	Time [h:min:s]	Rate[Hz] cut at 10 MeV	Rate [Hz/m^2]
Position 1	03:24:43	$0.06447(^{+0.0021}_{-0.0011})_{\text{syst}}(\pm 0.0023)_{\text{stat}}$	$99.7(^{+3.2}_{-1.7})_{\text{syst}}(\pm 3.5)_{\text{stat}}$
Position 2	01:52:32	$0.07287(^{+0.0016}_{-0.0019})_{\text{syst}}(\pm 0.0032)_{\text{stat}}$	$112.7(^{+2.5}_{-2.9})_{\text{syst}}(\pm 5.0)_{\text{stat}}$
Position 5	20:38:04	$0.06085(^{+0.0016}_{-0.0016})_{\text{syst}}(\pm 0.0009)_{\text{stat}}$	$94.1(^{+2.5}_{-2.5})_{\text{syst}}(\pm 1.4)_{\text{stat}}$
Position 7	00:34:55	$0.05632(^{+0.0028}_{-0.0024})_{\text{syst}}(\pm 0.0048)_{\text{stat}}$	$87.1(^{+4.3}_{-3.7})_{\text{syst}}(\pm 7.4)_{\text{stat}}$

Table 3.1: Rates at different position in XR-20 during reactor on time. Position 5 corresponds to the CONUS+ location. The 10 MeV cut corresponds to only selecting muons with an incidence angle of up to 30 degrees.

3.6.2 Measurement during reactor OFF-time

To further investigate the impact of gamma radiation on the muon spectrum and to accurately measure the muon rate, several measurements were conducted during reactor outage to avoid high energy gammas. Since a considerable amount of time passed between the reactor on and off measurements and additionally the scintillator was refilled, the detector was calibrated again. This time, however, no source was used, but instead, the ^{40}K and ^{208}Tl Compton edges of the background spectrum were studied with the method described in subsection 3.5.1. An average calibration factor of $f_2 = 0.1072 \pm 0.0011$ ADC/keV was obtained.

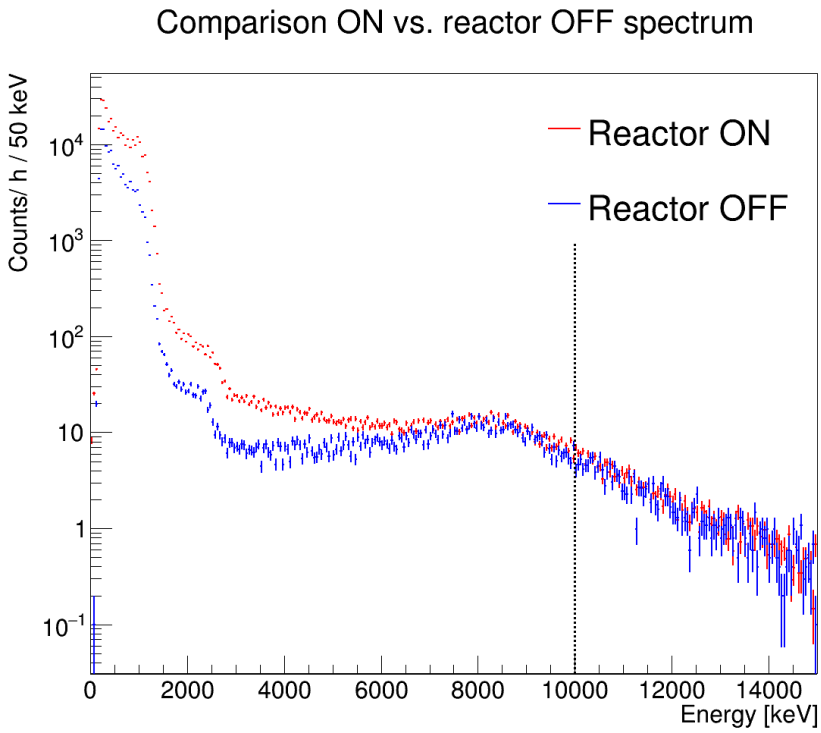

Figure 3.6.2: Comparison of the spectrum during reactor OFF and reactor ON-time. Both spectra are normalised to counts per hour. The vertical dashed line indicates the energy cut at 10 MeV

In Figure 3.6.2, the red spectrum represents the data collected during ON-time, while the blue spectrum corresponds to reactor OFF-time. The energy cut at 10 MeV is indicated in a dashed black line. From Figure 3.6.2 it is evident that gamma radiation significantly impacts the spectrum during ON-time.

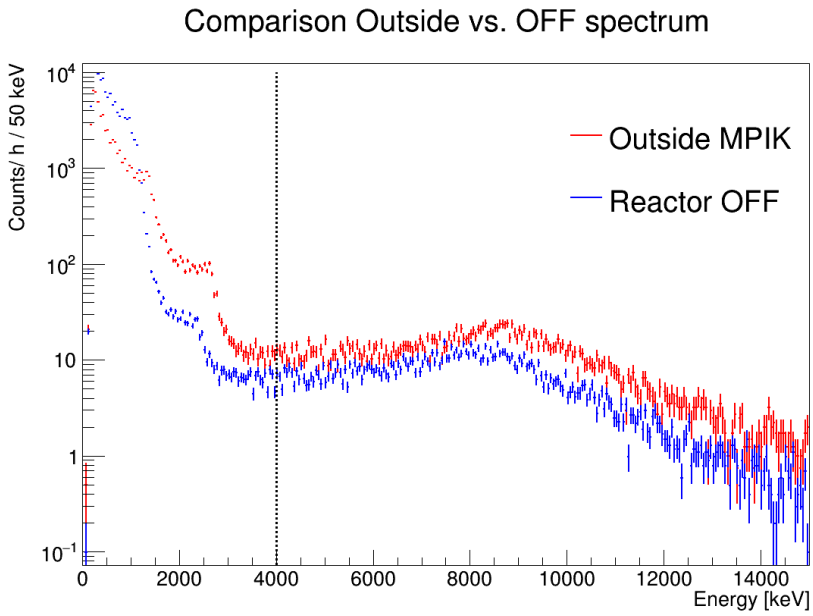

Figure 3.6.3: Comparison of the spectrum during reactor OFF-time and the MPIK spectrum outside. The Compton edge of ^{40}K at 1243 keV is distorted by an additional contribution of ^{60}Co at 1119 keV.

In Figure 3.6.3 the spectrum during off-time is compared with the MPIK spectrum outside. Both locations are at similar heights, with the MPIK being about 300 m above sea level and KKL being 340 m above sea level [73]. The muon flux at KKL is about $\sim$ 1.8 times below the flux at MPIK. In this image, it is also visible how the Compton edge of ^{40}K at 1243 keV is distorted by an additional contribution of ^{60}Co at 1119 keV.

Notably, the spectra during ON and OFF-time as well as the spectrum during reactor OFF-time and the MPIK spectrum outside, exhibit small shifts against each other. This is most likely caused by insufficient calibration data. However, for the purpose of the analysis, this discrepancy does not have a significant effect. After applying the 4 MeV energy and PSD discrimination cuts, the remaining muon rate during OFF-time is about $0.3479(^{+0.0012}_{-0.0016})_{\text{syst}}(\pm 0.0031)_{\text{stat}}$ Hz, which corresponds to $112.5(^{+0.4}_{-0.5})_{\text{syst}}(\pm 1.0)_{\text{stat}}$ Hz/m^2.
To put these numbers into context, they can be compared to KBR. The muon flux was measured at the KBR location and in the low-level laboratory (LLL) at the MPIK. According to these measurements, the rate at LLL is 1.6 times larger than in KBR [49]. Measurements with the scintillator module in LLL showed a rate of $0.2171(^{+0.0004}_{-0.0003})_{\text{syst}}(\pm 0.0018)_{\text{stat}}$ Hz. Therefore, the rate at KKL is approximately 2.6 times larger than the muon rate at the experimental location in KBR.

Muons however are not the leading cause of background in the shield but the muon-induced neutrons. The former experimental location at KBR had an average overburden of 24 m w.e.. At this depth, the muon-

induced neutron flux can be approximated to $4.7 \times 10^{-4} \mathrm{cm}^2 \mathrm{s}^{-1}$. Considering the reduction of cosmic rays in subsection 1.4.1 the CONUS+ location at KKL has an estimated overburden of about 6 m w.e.. At this overburden muons produce about 9.3×10^{-4} neutrons per $\mathrm{cm}^2 \mathrm{s}^{-1}$ [28]. This is 2.5 larger than at KBR.

In CONUS, muons caused a total of about 5 evt/kg/d below one keV, with the total background being about 10 evt/kg/d. With the same shield configuration, at the location in KKL, the background could increase to 12.5 evt/d/kg, making the muon-induced background 70% of the total background. To maintain a similar background level in CONUS+ the active shield needs to improve its background rejection of muon-induced events from about 97% [51] to over 98.8%.

Achieving this efficiency level with an additional muon veto is the most straightforward approach from an experimental standpoint. The next chapter will use various Monte Carlo simulations to explore whether this can be accomplished with an additional muon veto and how it might impact the overall shielding.

Chapter 4

Monte Carlo simulations for CONUS+

In order to investigate the effect of the muon veto upgrade on the detector's overall performance, a series of Monte Carlo simulations were conducted. These simulations were executed through the utilisation of MAGE [76] (MAjorana-GErda), a GEANT4-based Monte Carlo framework jointly developed by the MAJORANA and GERDA collaborations. Within Geant4, it is possible to simulate a range of particle interactions. The choice of physics list depends on the nature of the simulated interaction. These physics lists define the particles to be simulated and the models responsible for describing them.

The MaGe framework already has several physics lists implemented. For instance, electromagnetic interactions are described with low-energy models that are based on the Livermore data libraries. This is described in greater detail in [76]. For this thesis, the physics list optimised for low-energy and low-background experiments, as well as muon-induced neutrons, was selected.

The simulations include the full geometry of the CONUS+ setup, encompassing shield and detectors. The code developed by Janina Hakenmüller was modified and enhanced to fit the new CONUS+ configuration. This modification involves the integration of the PMT geometry and the geometry of the new inner muon veto. The CONUS+ geometry is depicted in Figure 4.0.1. Additionally, both muon vetos were designated as sensitive detectors within the simulation framework. This allows the tracking of all particle entry points. Furthermore, the simulations record the energy deposition of individual particles within the sensitive volumes, e.g. the muon vetos and the germanium crystals.

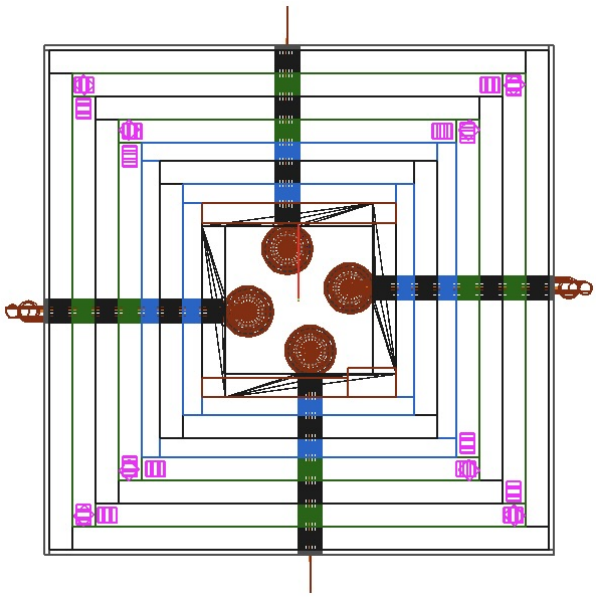

Figure 4.0.1: Top view of the CONUS+ detector. PMTs are shown in pink. The plastic scintillator layers are depicted in green. The four high-purity germanium detectors are shown in red.

These implementations enable simulations focused on the rejection efficiency of the muon vetos, their impact on material background, and the potential gamma shielding reduction.

4.1 Simulation of the muon flux

The zenith angle distribution of cosmic muons is drawn from the muon distribution function defined in [77]. To precisely simulate the energy distribution of muons at the specific location of Leibstadt, the PARMA/EXPACS4.0 [78] toolset was used. EXPACS is an EXcel-based Program for Calculating Atmospheric Cosmic-ray Spectrum and PARMA is a PHITS based Analytical Radiation Model in the Atmosphere, which comprises numerous analytical functions with parameters whose numerical values were fitted to reproduce the results of the extensive airshower simulation performed by Particle and Heavy Ion Transport code System (PHITS) [79].
This allows to instantaneously calculate a variety of terrestrial cosmic ray fluxes, including neutrons, protons, muons and photons. The calculations are dependent on time and location in Earth's atmosphere. The calculated energy distribution for the atmospheric muon flux in Leibstadt is depicted in Figure 4.1.1.

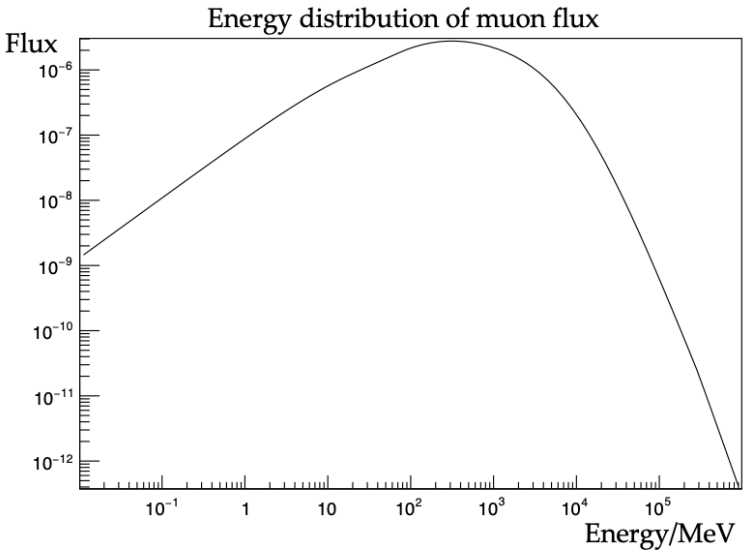

Figure 4.1.1: Energy distribution of atmospheric muons calculated with PARMA/EXPACS4.0 for the position of Leibstadt.

The muons are generated in the Monte Carlo simulation using the General Particle Source(GPS), which gives the user the possibility to choose from diverse source geometries and specify the energy and angular distributions from the primary particles. This was vital in accurately simulating the atmospheric muon flux at the specific KKL location. However, a compromise must be made when defining the source geometry, taking into account considerations such as source size, desired statistics, simulation duration and feasibility. For instance, larger sources require a greater number of particles and consequently extend the simulation time.

While a source encompassing the CONUS+ shield might seem ideal from a purely physical perspective, simulations involving a hemisphere yielded relatively low particle fluxes within the CONUS+ detector. This deficiency in particle count hindered the attainment of satisfactory statistical significance. After evaluating various geometries, it was discerned that a simple plane positioned above the detector offered the most optimal compromise.

Nevertheless, it's important to acknowledge that the angular and energy distributions of muons could potentially be influenced by the specific location within room XR-20. The geometry of the nuclear reactor building in conjunction with the solid angle coverage of the ceiling and the walls, could lead to variations in these distributions. Addressing this variation would necessitate the development of a new particle generator, a task beyond the scope of this Master's thesis. Consequently, for all simulations, a flat overburden was adopted to simplify the simulation conditions.

In the course of the simulation, a substantial number of muons were generated. By utilising the measurements detailed in subsection 3.6.2, the generated muon flux was normalised to reflect the actual number of muons per unit area and time. This normalisation process ensured a faithful representation of the real-world conditions within the simulation framework.

4.2 Efficiency

The focal point of the muon veto upgrade is the enhancement achieved through the incorporation of an inner veto layer. In these simulations, the atmospheric muon flux is generated as previously described in section 4.1. In this context, a muon event is recorded as observed by a muon veto, once it deposits more than 2.6 MeV within a single plastic scintillator plate. This particular energy threshold was chosen due to its ability to effectively discriminate against high-energy gamma events that can also generate hits within the plastic scintillator material. This threshold cut was selected at 2.6 MeV for higher cuts would lead to a significant reduction of data available for CEνNS searches.

In Figure 4.2.1 the energy depositions inside both muon veto layers are depicted. In total 10^8 particles were emitted from the source geometry. In both muon vetos the energy deposition spectrum shows three peaks. The first peak corresponds to vertical energy deposition in the top plate. The second peak originates from not vertical muons passing an even larger fraction of the scintillator, thereby depositing more energy. The largest peak stems from muons with vertical directions that pass the side plates of the muon veto, effectively having the longest path inside the scintillator. This peak is thereby only present in the energy deposition spectrum of the side plates. This can be confirmed as most muons at sea level have an average energy of approximately 4 GeV, and lose about 2 MeV per g/cm^2 [80]. When passing through the entire length of the side plates, they are expected to lose about 170 MeV in the outer layer and about 63 MeV in the inner muon veto. In the top plates, muons with a vertical trajectory are expected to lose 12 Mev and 9 MeV in the outer and inner plates, respectively. This agrees well with the spectra observed in Figure 4.2.1 and Figure 4.2.2.

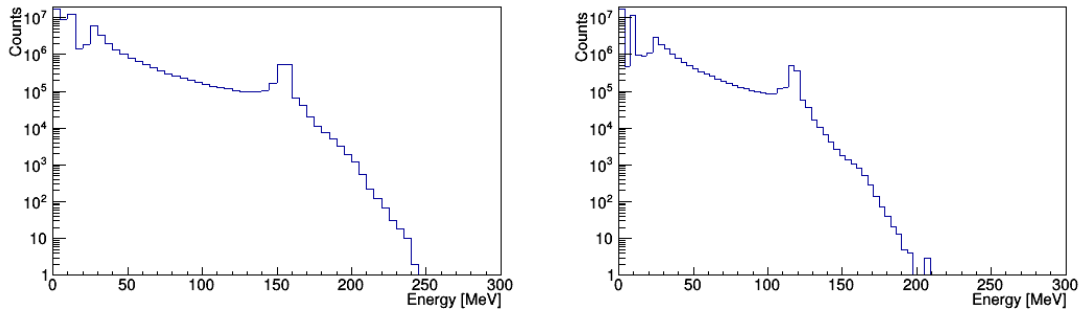

Figure 4.2.1: **Left:** Total energy deposition in the outer muon veto. **Right:** Total energy deposition in the inner muon veto. The peak with the highest energy corresponds to vertical muons travelling through the side plastic scintillator plates.

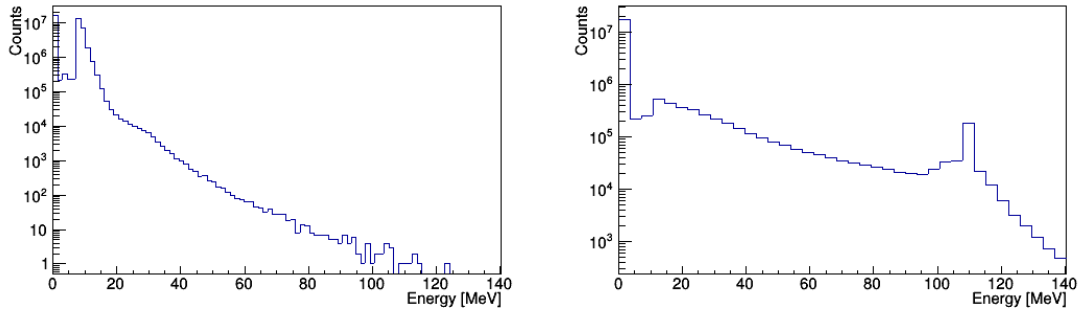

Figure 4.2.2: **Left:** Total energy deposition in the top plate of the inner muon veto. **Right:** Total energy deposition in one side layer of the inner muon veto.

The parameter of interest is the efficiency of the muon veto to detect particles that instigate events within the region of interest (ROI) of CEνNS and neutrino magnetic moment (NMM). These ranges span from 0.16 to 1 keV for CEνNS and 2 to 8 keV for the NMM.

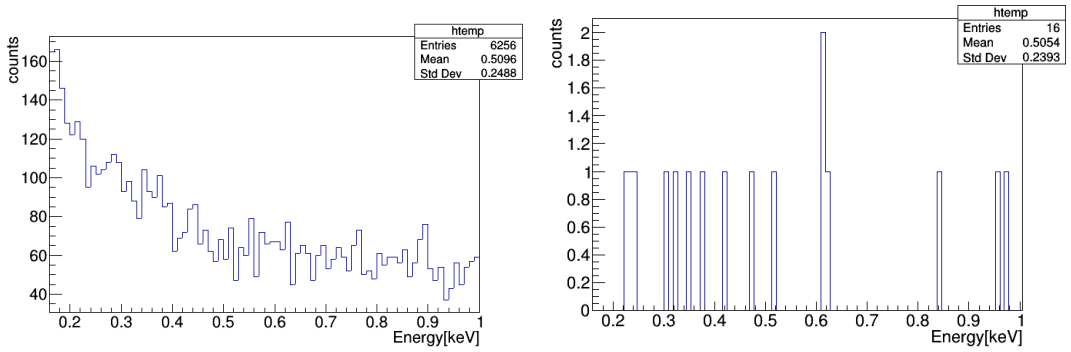

(a) Energy depositions in the ROI of CEνNS inside the germanium crystals.

(b) Energy depositions not detected in ROI of CEνNS inside the germanium crystals.

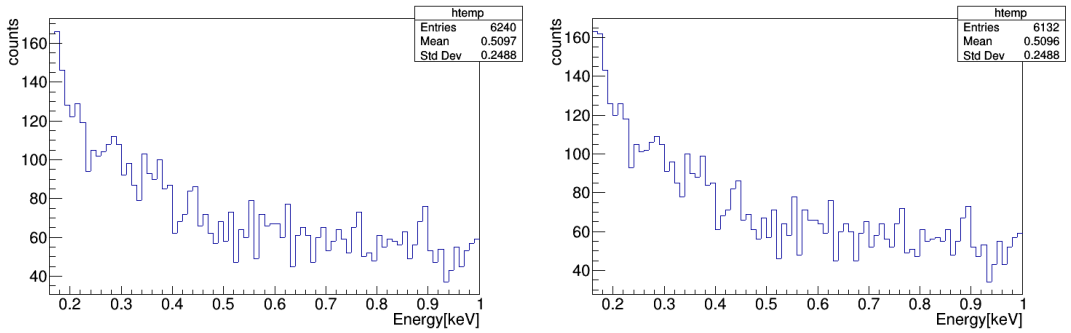

(c) Energy deposition in the ROI of CEνNS inside the germanium crystals detected by the outer muon veto.

(d) Energy deposition in the ROI of CEνNS inside the germanium crystals detected by the inner muon veto.

Figure 4.2.3: Energy deposition inside the germanium crystals.

Conducting simulation with a total of 10^8 particles, a collective of 6256 events were recorded within the ROI for CEνNS in the germanium crystals. Out of these events, 6240 deposited more than 2.6 MeV in the outer layer of the muon veto. This gives the outer veto's detection efficiency of:

$$\varepsilon^{out}_{CE\nu NS} = \frac{6240}{6256} \approx 99.74\%. \tag{4.1}$$

On the other hand, the inner muon veto detected 6132 events. This gives a detection efficiency of:

$$\varepsilon^{in}_{CE\nu NS} = \frac{6132}{6256} \approx 98.01\%. \tag{4.2}$$

As for the efficiency in the NMM ROI:

$$\varepsilon^{out}_{NMM} = \frac{16455}{16480} \approx 99.85\%. \tag{4.3}$$

$$\varepsilon^{in}_{NMM} = \frac{16256}{16480} \approx 98.64\%. \tag{4.4}$$

Simulations show that the inner muon veto's detection efficiency is lower than the outer muon veto's. This can be attributed to the fact that most background stems from neutrons, generated through spallation processes of muons in the lead layers. Neutrons induced in the lead layer situated between the two muon vetos

can cause events in the germanium crystals which will not be recorded by the inner muon veto. On the contrary, the outer muon veto likely detects the corresponding muon, thereby achieving a higher detection efficiency. Interestingly, about 95.57% of events inside the germanium crystals are caused by neutrons.

Overall, the simulations offer a promising outlook, suggesting that a remarkably high level of efficiency for the muon veto of CONUS+, reaching approximately 99%, is attainable in theory. It's imperative to underscore that these efficiency simulations encompass the realm of ideal conditions, and thus, the practical efficiency may deviate from this theoretical projection.

Previous tests for CONUS obtained a rejection efficiency of about 97% for the outer muon veto. This disparity with the MC could be caused by potential dead time inherent to the scintillator plates or the light collection efficiency of the PMTs themselves.
The dead time is the amount of time from the total measurement where no data is taken, usually given in percent. It is related to the window length for which the data acquisition stops after an incoming muon in the scintillator plate. In CONUS the window length was set to 164 μs which resulted in a dead time of $\sim$0.3% [57].
Furthermore, the impact of high energy gamma radiation, including gamma emissions resulting from the decay of ^{16}N as observed with CONRAD (see section 3.2), could require a higher energy cut, effectively reducing the rejection efficiency.
Given these considerations, it's reasonable to anticipate that the actual efficiency of the muon veto will likely manifest at a slightly lower level than projected in the simulations.
In the next section, it will be examined, if the light collection efficiency of the PMTs significantly impacts the performance of the muon veto.

4.3 Light collection simulations

The effective detection of events inside the plastic scintillator plates is crucial for reaching a low dead time and therefore a high muon rejection efficiency. To verify that the configuration of the PMTs, in terms of their number and positions, is suitable for optimal light collection, light simulations were conducted in Geant4. In these simulations, 200000 energy depositions of 1 MeV each, uniformly distributed inside the inner plastic scintillator plates, were initiated. Included in the simulations are all three types of plastic scintillator plates, namely the top, lateral-top and lateral-bottom plates, the PMTs and their dead volumes. The scintillator parameters used in this simulation are taken from [81], while the PMT quantum efficiency was sourced from [58]. Furthermore, a reflectivity of 99% is assumed. The geometries of the side plates in Geant4 are illustrated in Figure 4.3.1.

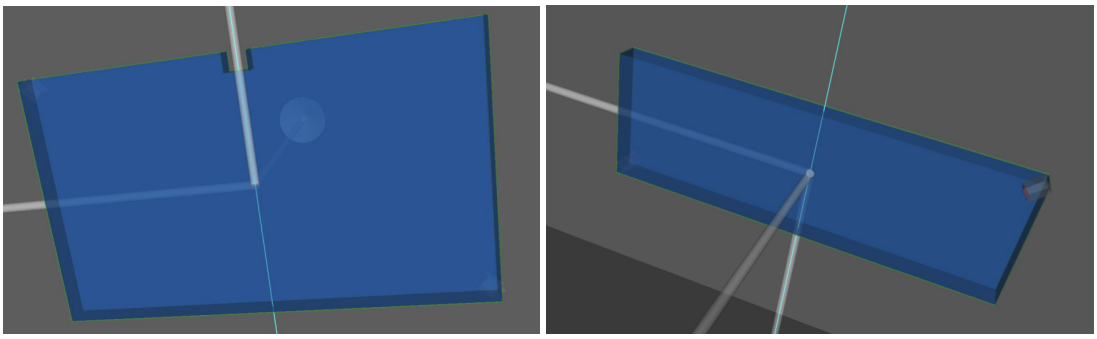

Figure 4.3.1: Geometries of of scintillator plates in Geant4. **Left:** Lateral-bottom plate. **Right:** Lateral-top plate.

The emission spectra of the plastic scintillator plates can be seen in Figure 4.3.2.

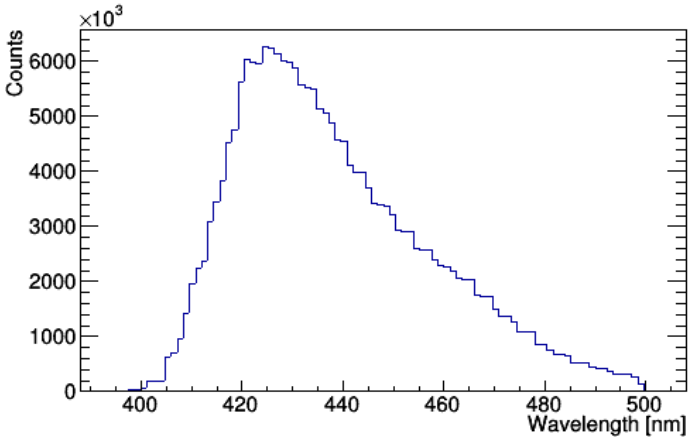

Figure 4.3.2: Emission spectra of the plastic scintillator.

Figure 4.3.3 shows the number of photons collected in the side plates per PMT, with the lateral-top plate on the left and the lateral-bottom plate on the right. The PMTs in the lateral-top plate collect overall more photons than in the much larger lateral-bottom plate.

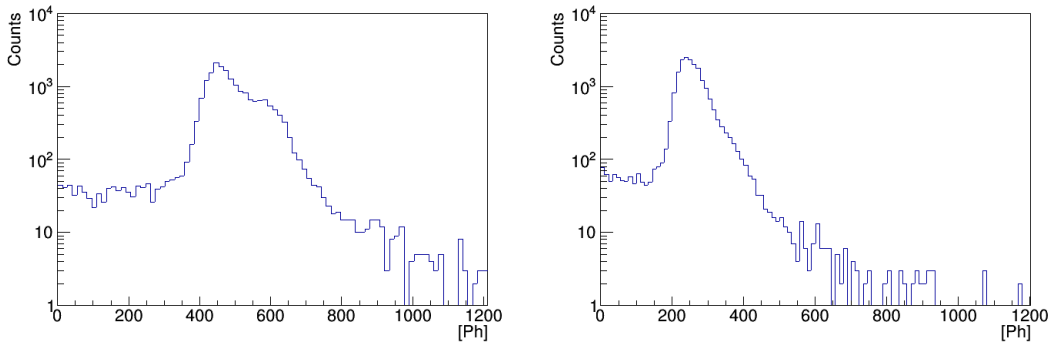

Figure 4.3.3: Light collection in scintillator plates. **Left:** Lateral-top plate. **Right:** Lateral-bottom plate.

The results from these simulations reveal that each PMT in the top plate collects about $\sim$1.3% of the produced light. Slightly higher is the light collection efficiency of the lateral-bottom plate PMTs with about 2.4%. The smallest plate, the lateral-top plate, has the highest light collection with about 4.51%.

This analysis reaffirms the suitability of the PMT configuration in CONUS+ for optimal light collection, contributing to the overall effectiveness of the muon veto.

Furthermore, the uniformity of the light collection was studied. The asymmetry of photons detected by one PMT compared to the other PMT is plotted against the length of the side top plate in Figure 4.3.4. Close to the centre of the plate, the light collection is quite uniform. However, in the vicinity of the PMTs, the asymmetry increases. For most events, the asymmetry is not larger than 30%. Within close proximity of the PMTs, tails are formed which correspond to light depositions almost solely collected by one PMT. This highlights the necessity for at least two PMTs inside the plastic scintillator plates.

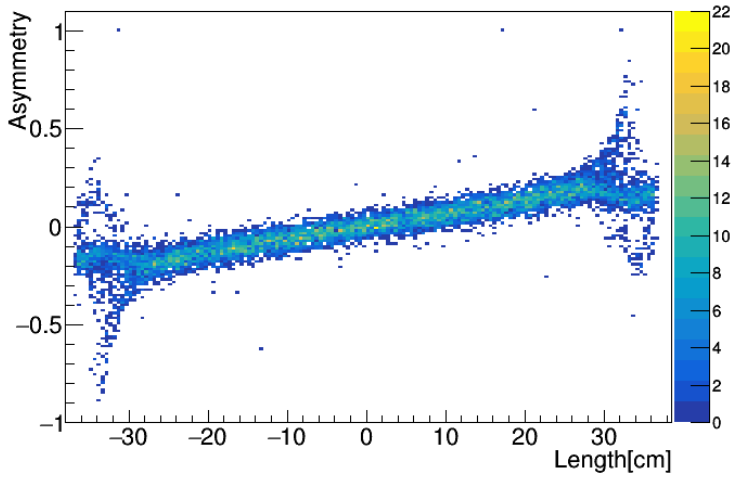

Figure 4.3.4: Asymmetry studies in the lateral-top plate.

4.4 Material background

In low-threshold experiments, the presence of background arising from material background constitutes a significant concern. With the replacement of a lead layer by a plastic scintillator layer equipped with 20 PMTs, it becomes crucial to assess the potential contribution of this new material background within the relevant regions of interest. To study the contamination effect stemming from muon veto plates and PMTs, separate simulations were conducted using the RDMiso generator. The material contamination numbers for the PMTs were provided by previous measurements by the XENON1T collaboration and the scintillators were screened at the MPIK (see Table 2.2).

Detector part	Isotope	Events in CEνNS ROI [events/year]	Events in NMM ROI [events/year]
Inner muon veto plates	^{226}Ra	$< 5 \cdot 10^{-2}$	$< 5 \cdot 10^{-2}$
	^{228}Th	$< 2 \cdot 10^{-2}$	$1.32 \cdot 10^{-1}$
	^{40}K	$< 9 \cdot 10^{-3}$	$< 9 \cdot 10^{-3}$
	^{228}Ra	$< 2 \cdot 10^{-1}$	$2.27 \cdot 10^{-1}$
	Total	$\mathbf{< 2 \cdot 10^{-1}}$	$\mathbf{3.6 \cdot 10^{-1}}$
Inner muon veto PMTs	^{226}Ra	$< 2 \cdot 10^{-2}$	$< 2 \cdot 10^{-2}$
	^{228}Th	$< 1 \cdot 10^{-2}$	$1.77 \cdot 10^{-2}$
	^{40}K	$< 4 \cdot 10^{-2}$	$< 4 \cdot 10^{-2}$
	^{228}Ra	$< 2 \cdot 10^{-2}$	$5.68 \cdot 10^{-1}$
	Total	$\mathbf{< 2 \cdot 10^{-2}}$	$\mathbf{7.44 \cdot 10^{-2}}$
Total		**$< 2 \cdot 10^{-1}$ events/year**	**$4.34 \cdot 10^{-1}$ events/year**

Table 4.1: Expected events in ROI of CEνNS signal and NMM ROI

The material background caused by both the inner muon veto plates and PMTs is summarised in Table 4.1. In the simulations, no events were observed within the ROI of the CEνNS signal. Notably, the upper limit for events within the CEνNS ROI for the entire system is impressively below $2 \cdot 10^{-1}$ events per year. An estimated total of $4.34 \cdot 10^{-1}$ events per year are expected within the ROI for NMM.
Given these findings, it is evident that the material background attributed to the incorporation of an additional muon veto can be safely disregarded. The negligible impact of this background on the overall experiment highlights the careful design and meticulous assessment of the upgraded system.

4.5 Shielding from gammas

The substitution of a lead layer does not solely introduce a new background component, it also results in a reduction of the passive shielding within the experimental setup. To predict how 5 cm less lead impacts the background caused by gamma radiation, a series of simulations were conducted. These simulations were carried out both with and without the incorporation of the muon veto upgrade.
The gamma radiation was simulated according to the measurements with the CONRAD detector on site in KKL (see section 3.2). For these simulations, a selection of relevant gamma lines as listed in Table 4.2 were considered. The GPS generator was employed, and the source geometry was configured as a complete sphere encompassing the detector, as gamma radiation is expected to arrive from all angles.

Isotope	Energy [keV]	Rate in CONRAD [counts/day/kg]	Events in CEνNS ROI [events/day/kg]
^{60}Co	1175	755505	< 0.8823
	1334	773089	< 0.8644
^{63}Cu	7916	537	< 0.0939
^{55}Fe	9301	133	< 0.0225
^{56}Fe	7646	838	< 0.1479
^{40}K	1462	114718	< 0.1305
^{16}N	71113	1372	< 0.2397
^{208}Tl	2615	24853	< 0.0285

Table 4.2: Results of the gamma radiation simulation with muon veto upgrade. No events were detected within the ROI of both the CEνNS signal and the NMM.

In simulations with and without an upgrade, no events were detected within the ROI of both the CEνNS signal and the NMM. This outcome aligns with expectations, considering that the gamma background was already a subdominant factor in the original CONUS setup. In total, less than 2.4 events are expected per day. However, these contributions are mainly made up by gammas from the decay of ^{60}Co. Future simulations with better statistics will be able to constrain this limit further.

In the upcoming chapter, the inner muon veto will be subjected to real-world experimental testing. Subsequently, we will compare these empirical findings with the MC simulation results presented in this chapter, thereby confirming their validity.

Chapter 5

Commissioning of the inner muon veto at MPIK

Before installation at the nuclear power plant in Leibstadt, the inner muon veto underwent comprehensive testing within the 11A laboratory at the MPIK in Heidelberg. These tests aimed to optimise the settings of the muon veto in KKL and provide an initial understanding of its operation.

This chapter starts with general PMT tests, which evaluated the functionality of the PMTs and bases, and PMT calibration. Then, the light yield of the plastic scintillator plates is studied utilising both measurements and simulations. The chapter ends with a run of the entire inner muon veto setup in the CONUS+ configuration in the Low-Level Laboratory (LLL) of the MPIK.

5.1 Photomultiplier tests

The general functionality of the PMTs was assessed before their integration into the plastic scintillator plates. Once installed, the individual PMTs were calibrated using single photoelectron (SPE) pulses.

5.1.1 Testing general function of PMTs and bases

The first part of commissioning involved testing the overall functionality of all PMTs. A total of 23 PMTs were available for testing. Each PMT was placed inside a black-walled box, as depicted in Figure 5.1.2, which was further covered by a blanket made of a light shielding material. The PMTs were tested at voltages of 750 V, 800 V, 850 V and 900 V. To ensure consistency in testing, the same base was used to test all PMTs. Furthermore, to guarantee that each PMT was adequately de-excited after handling, an additional 30 minutes was waited between installing the PMT in the setup and the measurements. The light-tightness of the setup

was verified by performing measurements with and without light, which demonstrated no change in signal or rate, confirming the setup's light-proof nature. The response of the PMTs to single events was observed using an oscilloscope.

In total out of the 23 PMTs, 21 were found to be functional and fit to be installed in the plastic scintillator plates of the inner muon veto.

Furthermore, dark current measurements were conducted for each PMT at 750 V, and the results are presented in Figure 5.1.1. Clearly, PMT 1163 and PMT 1042 exhibit the largest dark current flux. This is mainly caused by a greater number of impurities in the photocathodes which generate electrons and holes in the depletion region of the device. Excluding PMTs with unusually high currents, e.g. PMTs 1163, 1042, LV1371 and LV1388, the average dark current is about 194 Hz.

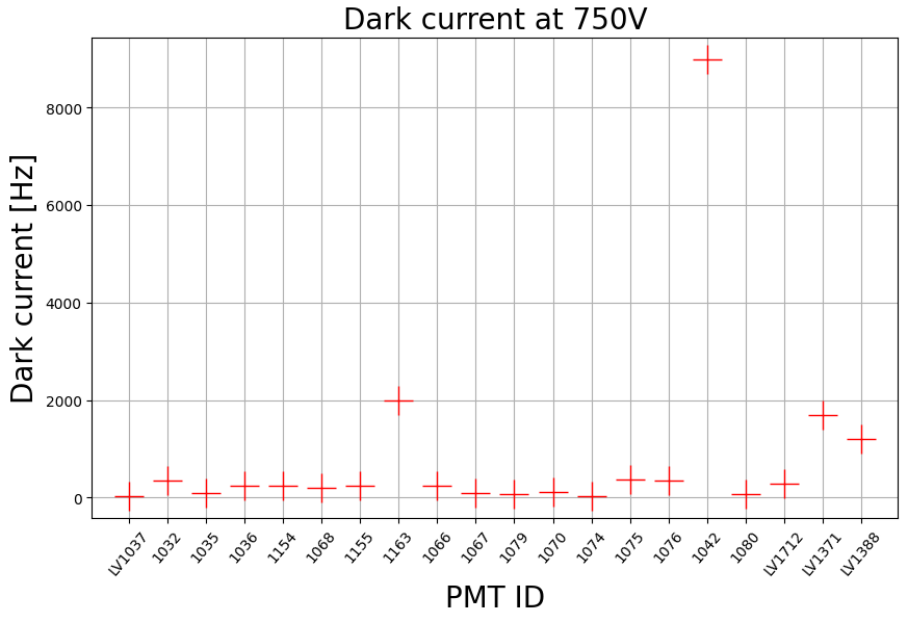

Figure 5.1.1: Dark current at 750 V. PMT 1163 and PMT 1042 exhibit the highest dark currents. This is caused by a greater amount of impurities in the photocathodes which generate electrons and holes in the depletion region of the device.

After each PMT was assigned a respective base further tests were performed. During these tests, the gain of each PMT was estimated. This was done by studying the pulse response to single photoelectron events (SPE) caused by dark current on the oscilloscope. On the right of Figure 5.1.2 a typical pulse shape is illustrated in the example of PMT 1068. Typical SPE amplitudes ranged from 2 to 4 mV.

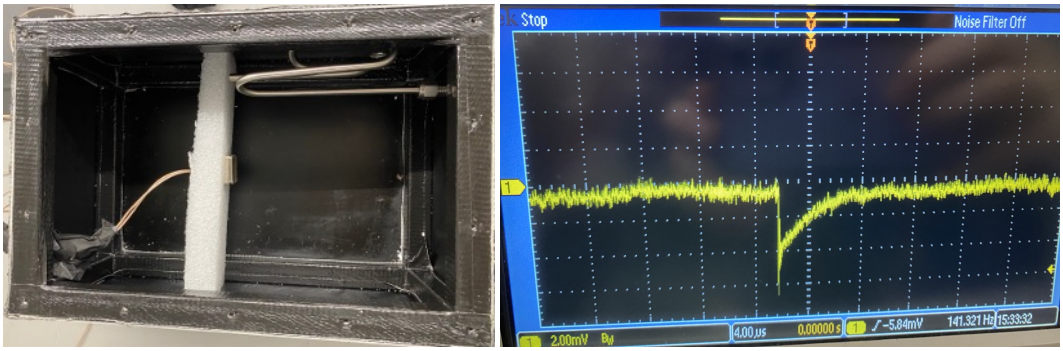

Figure 5.1.2: **Left:** Testing setup for the PMT tests, with an installed PMT visible in the middle. **Right:** Oscilloscope signal showing responses to single events (PMT 1068).

Based on their gain and dark current characteristics, optimal positions within the CONUS+ shielding were determined. PMTs with similar gains were grouped together within the same plate, and the four PMTs with the best performance were selected for positioning within the top scintillator plate. The placements are shown in Figure 5.1.3.

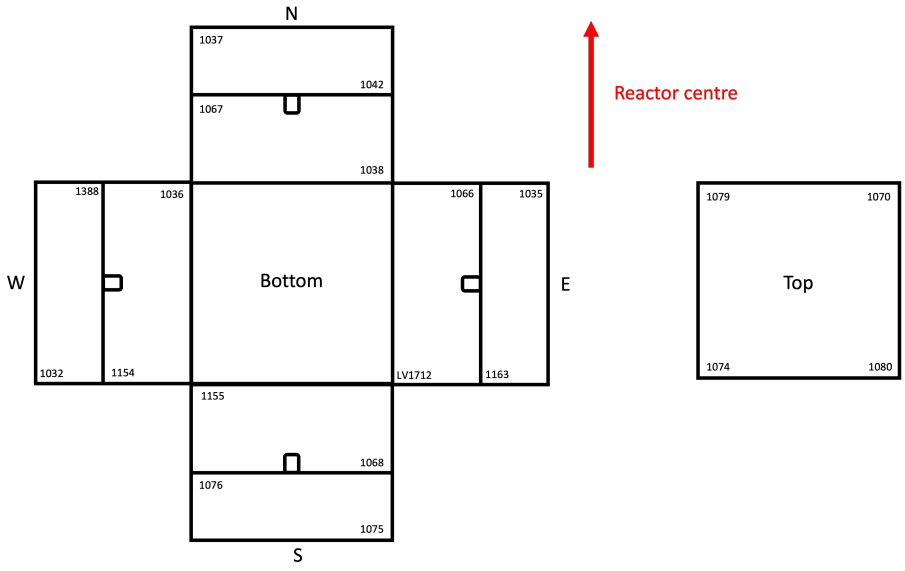

Figure 5.1.3: Positions of the inner PMTs within CONUS+ shielding

5.1.2 PMT gain calibration using SPE pulses

The PMTs were installed within the scintillator plates by Scionix [54]. After the plates returned to the MPIK, every PMT was reassessed. During testing the connections of signal and voltage cable to the bases of the PMTs were found to be quite delicate and at risk of breaking off. Therefore, after checking the PMTs' compatibility with their respective bases, measures were taken to enhance the stability of the signal and voltage connections and make the scintillator plates light-tight, utilising an appropriate silicone fixation. The silicone fixation can be seen in Figure 5.1.4.

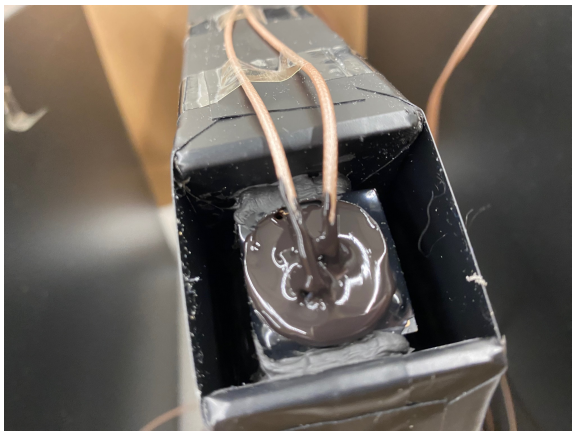

Figure 5.1.4: PMT base secured with silicone.

A standard method for PMT gain determination is obtaining the PMT response to a single photoelectron. The position of the charge peak produced by a single photoelectron emission is measured relative to the position of the pedestal peak, the electronic noise peak, which corresponds to zero induced photoelectrons.

While the ideal scenario involves testing PMTs individually, the fact that they were already installed in the plastic scintillator plates necessitated a modified testing strategy. Calibration is done using dark current where the amount of light is small enough that the single photoelectron emission is more likely than multiple photoelectron emission cases. These pulses are however dominated by the scintillation pulses of the plastic scintillator. Therefore we need to set a large acquisition window of 20 μs and analyse the data following a scintillation pulse. This ensures that contributions of the scintillation pulse are not included. In this region, we search for the largest peak and integrate the charge around the peak in a pre-set window of 15 μs. With an average dark current of about 200 Hz, the probability of having a dark current event in this region is about 0.3% in each pulse. The whole pulse shape is shown in Figure 5.1.5. The selected region after the pulse is marked in red.

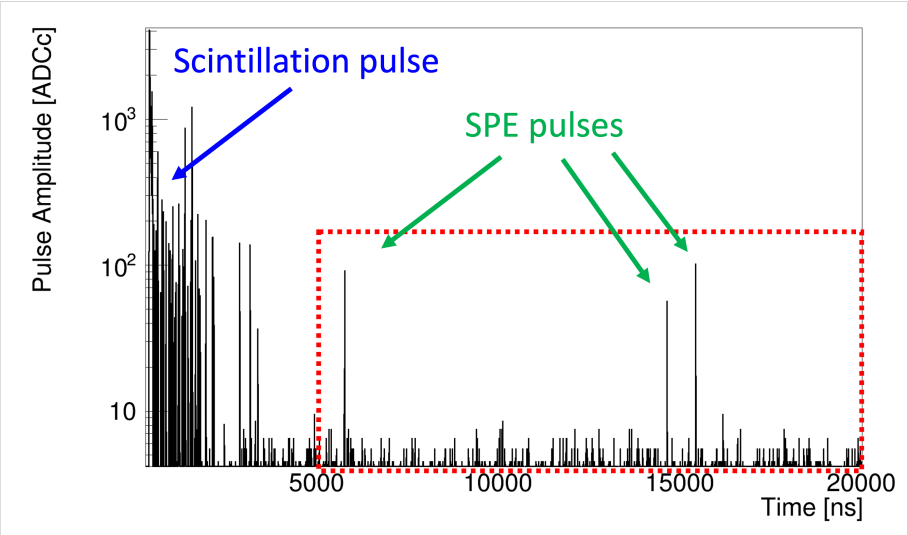

Figure 5.1.5: Entire pulse shape. The data following a scintillation pulse is analysed to ensure that single photoelectron events dominate over multiple photoelectrons generated by scintillation within the plate. The region selected is marked in red.

In order to extract the PMT gain we need to estimate the mean amplitude corresponding to one photoelectron event (PE). In the ideal case without any noise contributions the number n of PE to reach the first dynode of a PMT for a given number of emitted PE N is given by a Poisson distribution:

$$P(n;N) = \frac{N^n e^{-N}}{n!}. \tag{5.1}$$

The dynode chain amplification response can be described by a Gaussian:

$$G(x) = \frac{1}{\sqrt{2\pi\sigma^2}} exp(-\frac{(x-\mu_{SPE})^2}{2\sigma^2}), \tag{5.2}$$

where x is the measured amplitude, μ_{SPE} is the mean SPE amplitude and σ is the standard deviation of the SPE amplitude distribution. Assuming n observed PE, the observed spectra can be represented in the following form:

$$S(x) = \sum_n A_n \frac{N^n e^{-N}}{n!} \frac{1}{\sqrt{2\pi n\sigma^2}} exp(-\frac{(x-\mu_{SPE})^2}{2\sigma^2}). \tag{5.3}$$

The effective gain calibration factor is obtained by fitting amplitude and pulse area distributions with the above analytical form and extracting the mean SPE amplitude parameter μ_{SPE}. For our data, this means we are fitting the integrated charge of the pedestal peak and the single electron peak:

$$S_{exp}(x) = \theta_P \frac{1}{\sqrt{2\pi n\sigma_P^2}} exp(-\frac{(x-\mu_P)^2}{2\sigma_P^2}) + \theta_{SPE} \frac{1}{\sqrt{2\pi n\sigma_{SPE}^2}} exp(-\frac{(x-\mu_{SPE})^2}{2\sigma_{SPE}^2}). \tag{5.4}$$

In Figure 5.1.6 the fits to the pulses of the PMTs in the top plate are depicted. These measurements were conducted at a voltage setting of 900 V. The green fit corresponds to the pedestal peak and the blue to the SPE peak.

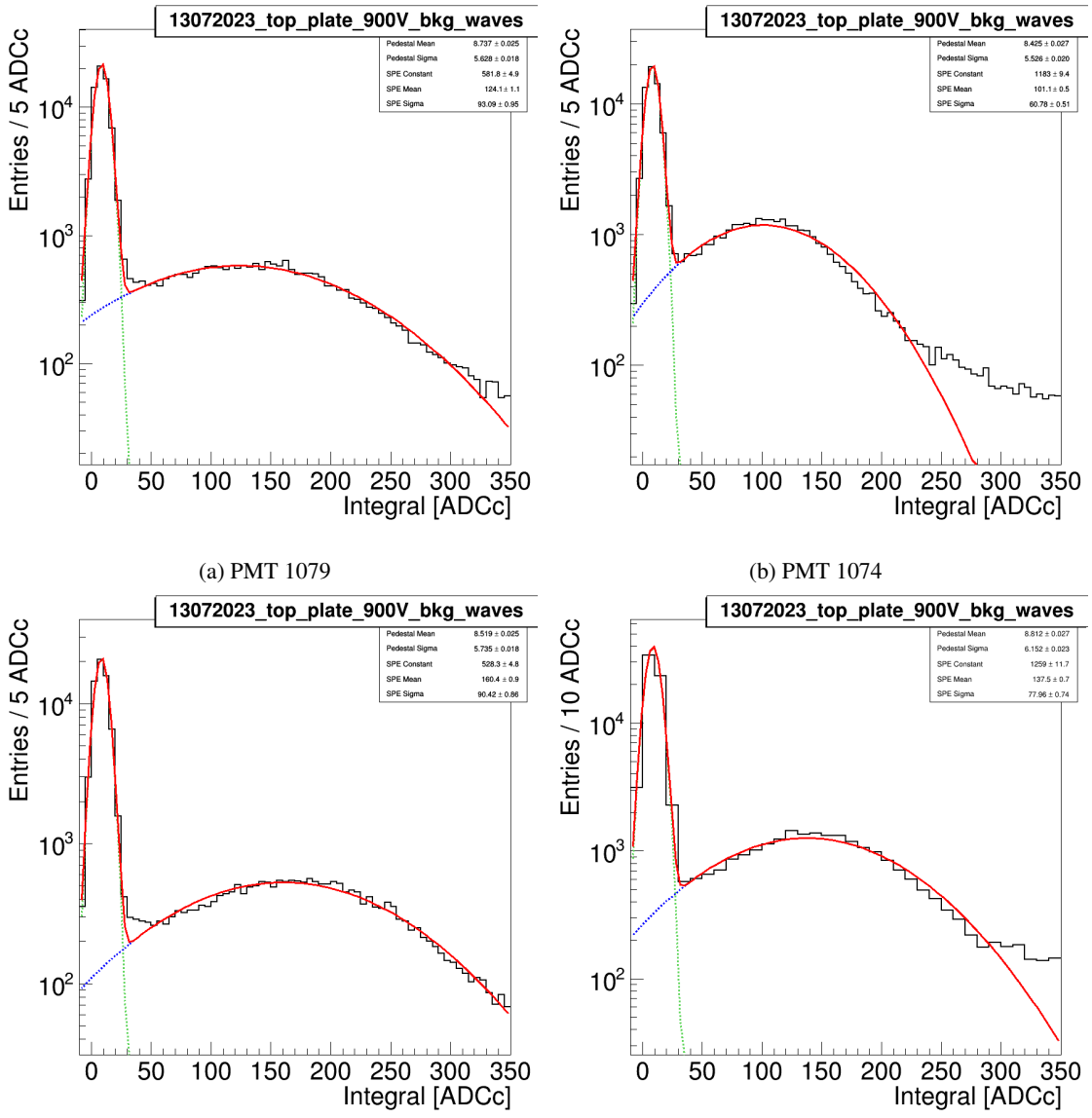

(a) PMT 1079

(b) PMT 1074

(c) PMT 1070

(d) PMT 1080

Figure 5.1.6: Fit to the pedestal and single photoelectron peak pulse of the top plate PMTs.

Details of the fit outcomes for each PMT are summarised in Table 5.1. Within some scintillator plates, the PMTs exhibit substantial differences against each other, often reaching around 50 counts. However, within the top plate, the PMTs display remarkably similar parameters, excluding PMT 1074.

Plate	PMT ID	750V	800V	850V	900V	Gain [SPE/V]
Top	1079	36.26 ± 0.14	58.51 ± 0.22	94.3 ± 0.4	138.7 ± 0.3	0.61 ± 0.07
	1074	27.68 ± 0.16	42.55 ± 0.28	67.85 ± 0.22	116.50 ± 0.20	0.46 ± 0.05
	1070	43.16 ± 0.12	70.18 ± 0.19	112.6 ± 0.40	160.4 ± 0.9	0.71 ± 0.08
	1080	35.24 ± 0.14	57.09 ± 0.20	93.05 ± 0.32	137.5 ± 0.7	0.60 ± 0.07
North Top	LV1037	20.10 ± 0.19	26.0 ± 1.4	38.7 ± 1.2	35.5 ± 1.5	0.121 ± 0.025
	1042	56.91 ± 0.21	85.8 ± 0.6	107.1 ± 1.4	118.6 ± 1.7	0.44 ± 0.08
North Bottom	1067	52.83 ± 0.24	62.1 ± 0.4	99.5 ± 0.6	156.4 ± 1.1	0.54 ± 0.08
	1038	22.77 ± 0.17	30.26 ± 0.27	42.3 ± 0.3	56.7 ± 0.6	0.21 ± 0.03
East Top	1035	56.54 ± 0.16	89.05 ± 0.27	140.7 ± 0.4	209.7 ± 0.7	0.90 ± 0.11
	1163	83.9 ± 1.3	52.75 ± 0.11	118.9 ± 0.5	155.40 ± 0.20	0.45 ± 0.10
East Bottom	1066	61.0 ± 0.2	102.6 ± 0.4	164.9 ± 0.8	252.5 ± 1.6	1.11 ± 0.12
	LV1712	-	-	-	-	-
South Top	1075	45.51 ± 0.18	73.96 ± 0.26	110.9 ± 0.5	161.3 ± 1.0	0.70 ± 0.08
	1076	29.7 ± 0.2	44.26 ± 0.18	68.4 ± 0.3	105.1 ± 0.8	0.43 ± 0.05
South Bottom	1068	41.51 ± 0.21	67.7 ± 0.4	112.2 ± 0.6	169.3 ± 1.1	0.74 ± 0.08
	1155	30.6 ± 0.3	51.9 ± 0.5	88.6 ± 0.5	139.6 ± 0.7	0.33 ± 0.05
West Top	1032	47.22 ± 0.17	75.5 ± 0.3	104.3 ± 0.7	149.7 ± 1.2	0.63 ± 0.08
	LV1388	114.3 ± 0.4	193.7 ± 0.9	309.7 ± 1.5	293 ± 19	1.40 ± 0.18
West Bottom	1154	50.09 ± 0.25	82.2 ± 0.5	132.1 ± 1.0	202.6 ± 1.6	0.88 ± 0.10
	1036	56.91 ± 0.6	61.1 ± 0.3	93.6 ± 0.6	137.8 ± 1.0	0.46 ± 0.08

Table 5.1: SPE value for every PMT at different voltages. The gain was deduced by a linear fit to the SPE values. PMT LV1712 was not usable during testing and is therefore not included.

The SPE parameter μ_{SPE} were estimated at voltage levels of 750 V, 800 V, 850 V, and 900 V. The relationship between SPE and voltage was characterised using a linear function $f(x) = a \cdot x + b$. An example of this is shown in Figure 5.1.7. Here the corresponding voltage is plotted against the SPE value of all four PMTs. The gain parameters a are summarised in Table 5.1. Since the systematic errors obtained by the fit in Table 5.1 were quite small, more conservative errors of 10% were chosen in order to account for the systematic errors in analysis, as temperature conditions, voltage stability and the missing identification of SPE pulses.

As can be seen for the PMT 1074 in Figure 5.1.7, not all PMTs were working optimally at higher voltages. For PMT 1074 the pulse obtained at 850 V and 900 V showed strong changes in the overall shape. Therefore, the PMT voltages were adapted to have similar gains within the same scintillator plate. During operation, the base of PMT LV1712 was damaged. For this reason, PMT LV1712 is excluded from this analysis. After the PMT tests were concluded, the base was repaired.

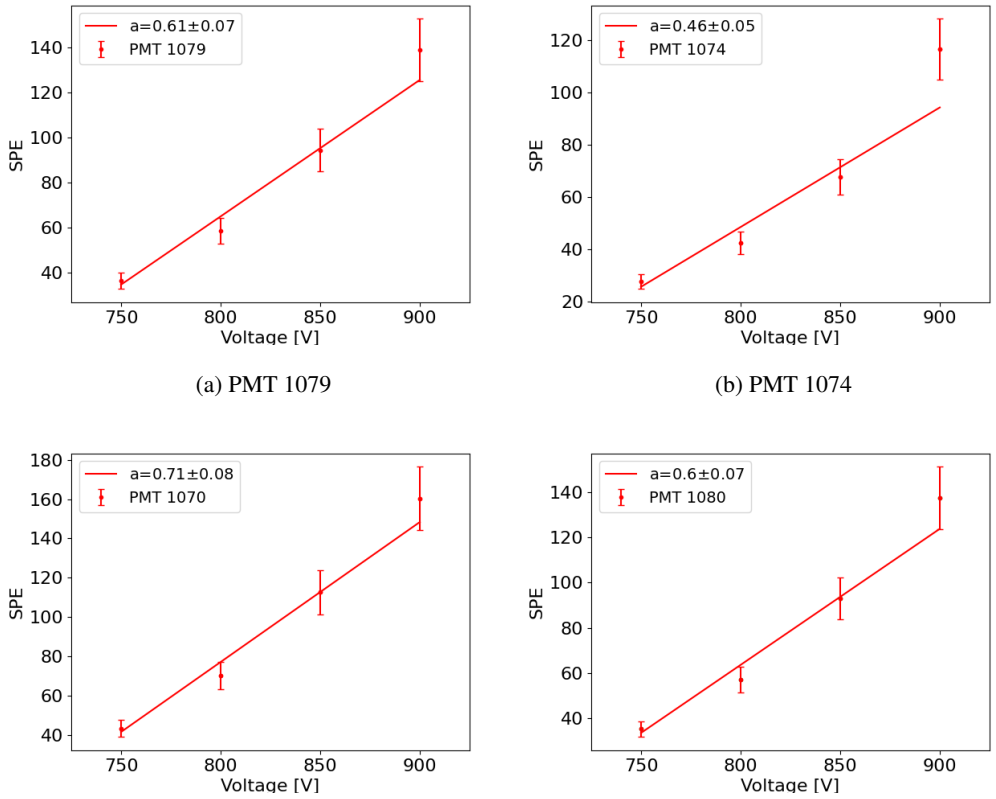

(a) PMT 1079

(b) PMT 1074

(c) PMT 1070

(d) PMT 1080

Figure 5.1.7: SPE dependence on voltage. The gain a was obtained with a linear fit. An error of 10% was assumed for the SPE values. The SPE value of PMT 1074 for 900 V does not fit well with the other SPE values at lower energies. This is due to the PMT not being suitable to perform at such high voltages and, therefore experiencing strong changes in the PMT pulse shape.

5.2 Light yield of the scintillator plates

The Monte Carlo simulation of section 4.2 predicted a promising rejection efficiency of approximately 99% for the muon veto in CONUS+. However, these simulations were conducted with ideal conditions assuming that every energy deposition in the scintillator layer over 2.7 MeV was detected with a 100% efficiency. For more realistic predictions it is crucial to understand the light yield of the plastic scintillator plates.

The absolute light yield of a scintillator is defined as the number of scintillation photons produced per unit of energy deposited. One should differentiate between absolute light yield (ν) from technical light yield (T). Absolute light yield is the ratio of the total number of scintillation photons (N_{PH}) to energy (E) deposited in the scintillator:

$$\eta = \frac{N_{PH}}{E}. \tag{5.5}$$

Technical light yield is a ratio of photoelectrons produced (N_{PE}), passing through a window, to energy E, deposited by radiation in the scintillator:

$$T = \frac{N_{PE}}{E}. \tag{5.6}$$

In the following section, the technical light yield of the scintillator plates is determined through experimental measurements as well as through MC simulations. From here on out, the technical light yield will be referred to as simply light yield.

5.2.1 Light yield measurements

The light yield of the scintillators is experimentally obtained by measuring the spectrum of a ^{60}Co source centred in the middle of the plastic scintillator plate. Each measurement lasted for five minutes and was performed at a voltage of 900 V.

^{60}Co is a synthetic radioactive isotope of cobalt with a half-life of 5.27 years [82]. ^{60}Co undergoes beta decay to the stable isotope ^{60}Ni. The activated nickel nucleus emits two gamma rays with energies 1.17 MeV and 1.33 MeV.

$$^{59}_{27}Co + n \rightarrow ^{60}_{27}Co \rightarrow ^{60}_{28}Ni + e^- + \bar{\nu}_e + \text{ gamma rays} \tag{5.7}$$

Figure 5.2.1 depicts the measured spectra of the ^{60}Co source in red and the background spectrum in blue. At higher energies the muon contribution is visible. At the low end of the spectrum the bump produced by the ^{60}Co line appears.

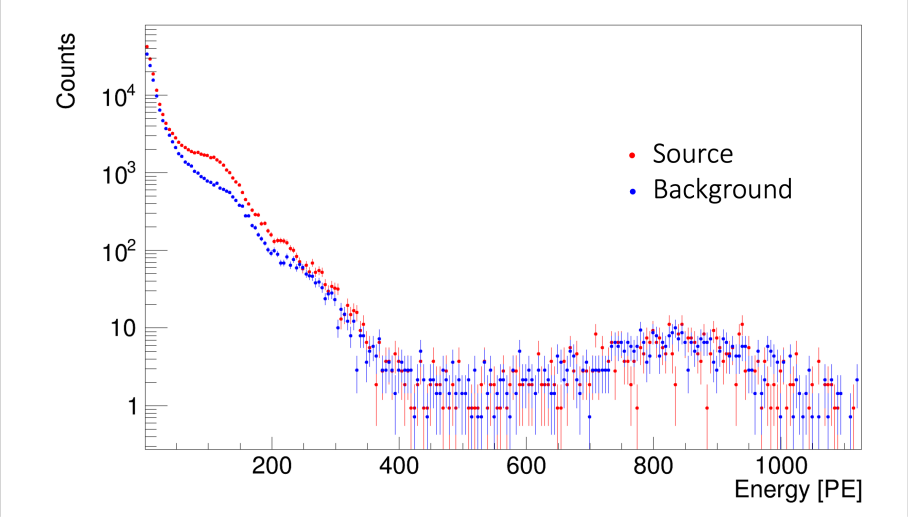

Figure 5.2.1: Spectrum of ^{60}Co source and background.

The net signal due to ^{60}Co is obtained by subtracting the background spectrum from the source spectrum. Gaussian fitting of the gamma peak is then applied to the difference spectrum. The mean value of the Gaussian distribution corresponds to the average value of the two gamma lines produced from the ^{60}Co decay of about 1.25 MeV. The light yield is obtained by:

$$T\ [\text{PH}]/[\text{MeV}] = \frac{E_{Gaussian}[\text{PE}]}{1.25[\text{MeV}]}. \tag{5.8}$$

The light yields of the different scintillator plates are summarised in Table 5.2. Missing in this table is PMT LV1712 in the east bottom side.

Plate	Top	Lateral-top				Lateral-bottom			
		North	East	South	West	North	East	South	West
T[PE/MeV]	174 ± 9	180 ± 7	174 ± 8	178.2 ± 2.8	179 ± 7	73.9 ± 1.6	37.7 ± 2.5	69 ± 5	70 ± 4

Table 5.2: Light yield of the scintillator plates at 900V.

The highest light yields have the lateral-top layers, with an average of 177 ± 6 PE/MeV. This value is similar to the light yield of the top plate of 174 ± 9 PE/MeV.

The largest discrepancies show the lateral-bottom plates with an average of 63 ± 3 PE/MeV. However, this is because in the east bottom side, PMT LV1712 could not be included. Excluding the east bottom side the average light yield in the lateral-bottom scintillator plates is 71.0 ± 2.7 PE/MeV.

5.2.2 Light yield simulations

To gain deeper insights into the light yield of the plastic scintillators, MC simulations similar to the light collection efficiency simulations discussed in section 4.3, were conducted. These simulations were carried out using Geant4. The scintillator parameters used in this simulation are taken from [81], while the PMT quantum efficiency was sourced from [58]. Furthermore, a reflectivity of 99% was assumed. In each simulation, the simulated ^{60}Co source generated a total of 20000 particles.

In Figure 5.2.2 the number of photoelectrons created by the PMTs of the top scintillator plate is depicted. A Gaussian fit applied to the peak of the photoelectron spectrum, marked in red, yielded a mean of 122.6 ± 0.5 PE. This results in a simulated light yield of $T_{sim} = 98.1 \pm 0.4$ PE/MeV. Following the same procedure, the light yield in the lateral-top and lateral-bottom layers of 173.8 ± 0.7 PE/MeV and 92.5 ± 0.4 PE/MeV is acquired.

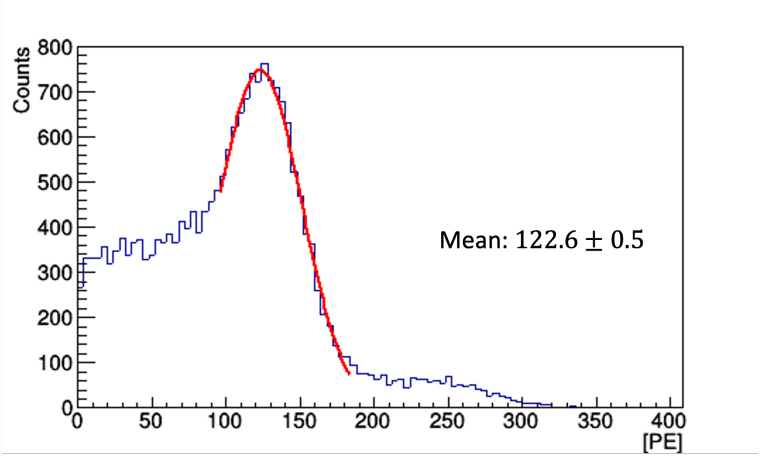

Figure 5.2.2: Number of photoelectrons induced in the MC simulation in each PMT for the inner top plate.

The light yields obtained in the simulations are summarised in Table 5.3 and compared to the experimental averages. The east bottom side was excluded from the comparison. The largest discrepancies in light are observed in the top layer, with a difference exceeding 75 PE/MEV. However, these numbers remain within the same order of magnitude. Closest to the measurements is the value of the lateral-top layers with a total of $T_{sim} = 173.8 \pm 0.7$ [PE/MeV] per plate, in contrast to the experimental average of $T_{exp} = 177 \pm 6$ [PE/MeV].

However, larger discrepancies emerge in the case of the lateral-bottom layers. The experimental average light yield, excluding the east bottom plate, is 71.0 ± 2.7 PE/MeV contrasting the 92.5 ± 0.4 PE/MeV obtained in simulations.

In summary, the MC simulations exhibit a general alignment with the light yield measurements, falling within the same order of magnitude. Future simulations which incorporate more intricate geometries and

optimised parameters will improve this agreement.

	Top plate	Lateral-top plate	Lateral-bottom plate
T_{exp} [PE/MeV]	174 ± 9	177 ± 6	71.0 ± 2.7
T_{sim} [PE/MeV]	98.1 ± 0.4	173.8 ± 0.7	92.5 ± 0.4

Table 5.3: Comparison of average experimental light yield to simulated light yield. The east bottom side was excluded from the average.

5.3 CONUS+ run with new DAQ

To evaluate the performance of the inner CONUS+ muon veto, measurements were conducted in the Low-Level Laboratory (LLL) at the MPIK, with an overburden of 15 m w.e. The nine plastic scintillator plates were placed in the CONUS+ configuration surrounding the four HPGe detectors, as illustrated in Figure 5.3.1. The DAQ setup of KKL, described in section 2.4, was employed, with the PMTs operating at optimised voltages as determined in 5.1.2.

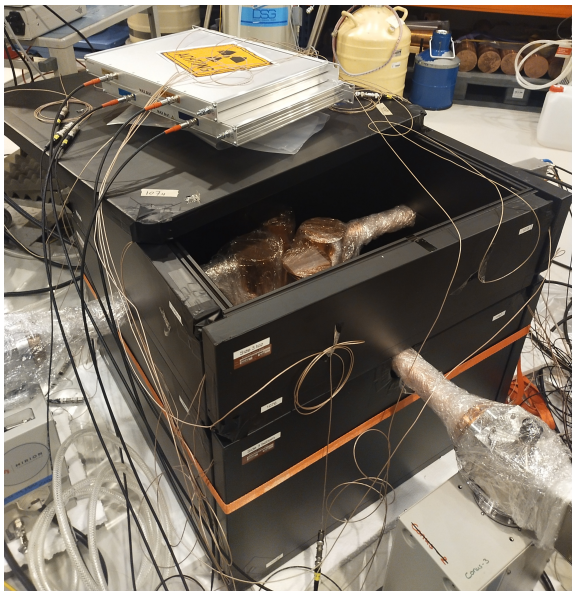

Figure 5.3.1: Muon veto test setup in LLL. The four CONUS+ detectors are installed inside the muon veto plates in the CONUS+ shield configuration.

For each PMT, both the energy deposition and timestamp data were recorded and saved in a root file. Figure 5.3.2 presents the spectra measured in different positions within the plastic scintillator plates. Overall, PMTs in the top plate showed much steeper energy deposition spectra. This can be seen best in the example of PMT 1074. In the top plate, only the energy spectrum of PMT 1079 shows a distorted shape, due to an

unexpected low gain.

On the contrary, spectra of the side layers display a more gradual decline and generally contain more events at higher energies. These findings are consistent with the MC spectra of energy depositions inside the plastic scintillators, as shown in Figure 4.2.2, confirming the validity of our MC simulations.

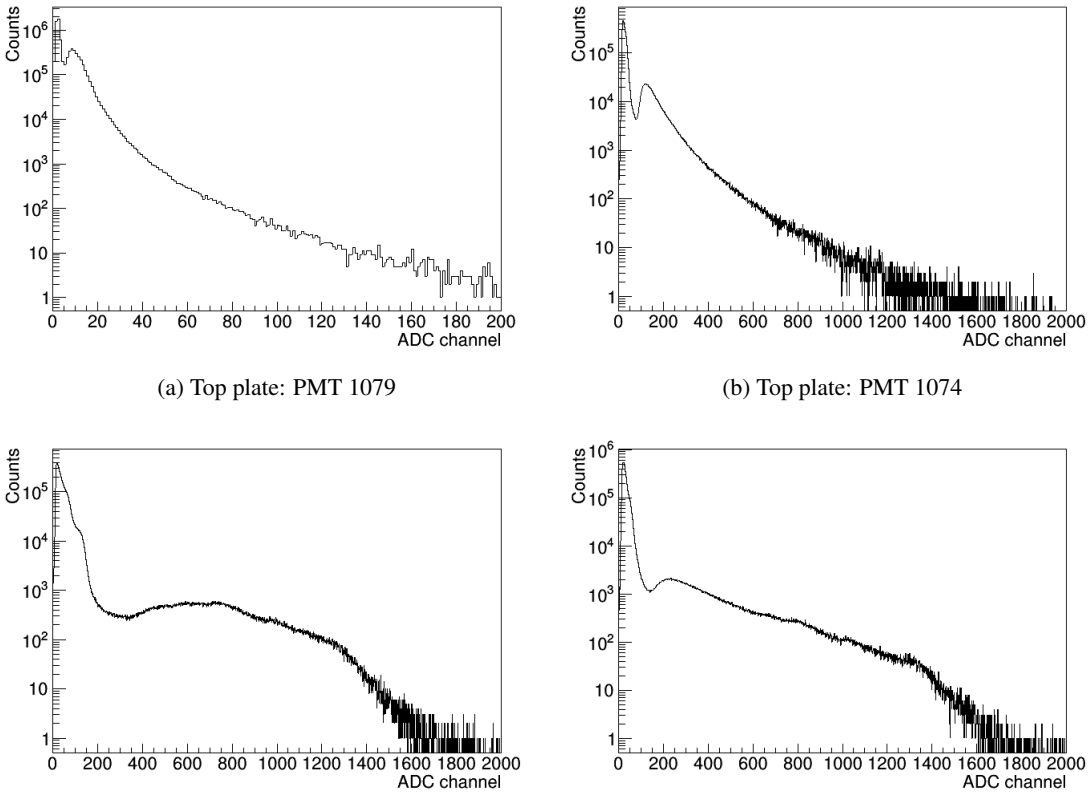

(a) Top plate: PMT 1079

(b) Top plate: PMT 1074

(c) Lateral-top: PMT 1042

(d) Lateral-bottom: PMT 1154

Figure 5.3.2: PMT spectra in different positions in inner muon veto. The top plate PMTs show much steeper energy spectra. Notably, the spectrum of PMT 1079 shows distortion hinting at a not optimised voltage setting. Spectra of the side layers exhibit a much more gradual decline compared to the top layers.

To assess the muon rates for each PMT within the plastic scintillator plates, a similar approach as described in chapter 3 was employed, including an energy cut to eliminate background gamma radiation. Figure 5.3.3 displays the spectrum of PMT 1080 with the energy cut shown in red.

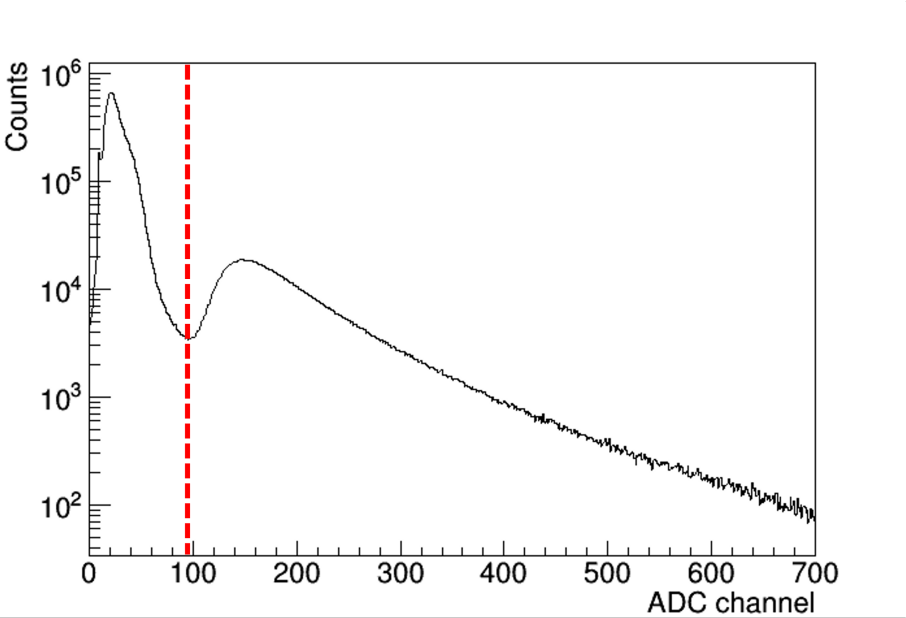

Figure 5.3.3: Spectrum of PMT 1080 with energy cut indicated in red.

Table 5.4 provides a summary of the muon rates in Hz for each PMT within the plastic scintillator plates. The top plate PMTs register the highest rates, averaging at 40.117 ± 0.027 Hz per PMT, as they are installed in the largest scintillator plate and more muons travel through the top than the side layers. Furthermore, the lateral-top layers average at 5.748 ± 0.010 Hz and the lateral-bottom layers at 11.744 ± 0.014 Hz.

	Top plate			
PMT	1079	1074	1070	1080
Rate[Hz]	51.02 ± 0.03	38.953 ± 0.026	31.554 ± 0.024	38.941 ± 0.026

	North Top		North Bottom	
PMT	LV1037	1042	1067	1038
Rate[Hz]	5.978 ± 0.010	5.771 ± 0.010	11.606 ± 0.014	11.761 ± 0.015

	East Top		East Bottom	
PMT	1035	1163	1066	LV1712
Rate[Hz]	5.716 ± 0.010	5.673 ± 0.010	11.673 ± 0.014	-

	South Top		South Bottom	
PMT	1075	1076	1155	1068
Rate[Hz]	-	5.780 ± 0.010	11.738 ± 0.014	11.650 ± 0.014

	West Top		West Bottom	
PMT	1032	LV1388	1154	1036
Rate[Hz]	5.638 ± 0.010	5.680 ± 0.010	11.951 ± 0.015	11.826 ± 0.015

Table 5.4: Rates of the PMTs in LLL. PMT LV1712 and PMT 1075 were not usable during testing.

Furthermore, additional analysis was conducted using a custom script to explore coincidences between PMTs. A 20 ns coincidence window was chosen. Given the sub-optimal performance of PMT 1079, it was excluded from the coincidence analysis.

Initially, the rates within the inner muon veto of different scintillators were examined by fitting the rate per second against time using a linear fit function. The right image of Figure 5.3.4 presents the rate over the entire measurement period for the top layer. The fit is depicted in red. As can be seen, the rate was overall stable throughout the entire measurement.
The rate within the top layer was determined to be 39.745 ± 0.027 Hz, which corresponds to about 64.52 ± 0.04 Hz/m^2. This is slightly lower than the rate expected by the liquid scintillator measurements suggesting $70.12(^{+0.12}_{-0.11})_{\text{syst}}(\pm 0.60)_{\text{stat}}$ Hz/m^2. The discrepancy likely stems from different measurement positions inside LLL and slightly different energy cuts. The rate inside the top plate is more than 50% of the rate in the entire inner muon veto of about 74.73 ± 0.04 Hz. Therefore, the top layer detects more than half of all incoming muons.

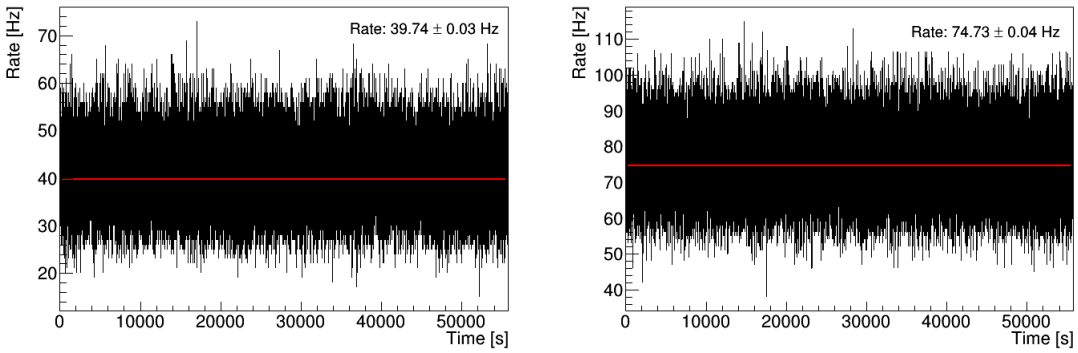

Figure 5.3.4: **Left:** Event rate in the top plate of inner muon veto. **Right:** Event rate across the entire muon veto.

Additionally, the coincidence between PMTs was investigated. The left image in Figure 5.3.5 depicts the number of PMTs triggered in each event within the top plate. In most instances, all three PMTs are triggered. Consequently, the majority of muon events within a plastic scintillator layer are detected by all PMTs.

In the case of the entire muon veto, the most common outcome is that three PMTs are triggered, likely corresponding to the top layer PMTs. Figure 5.3.5 illustrates the number of PMTs triggered in each event in the entire inner muon veto. As most side layers are equipped with two PMTs each, this number is the second most common. The third highest number of PMTs triggered is five, potentially stemming from a muon passing both the top and one side plate. Instances of more than seven triggered PMTs are likely due to random coincidences.

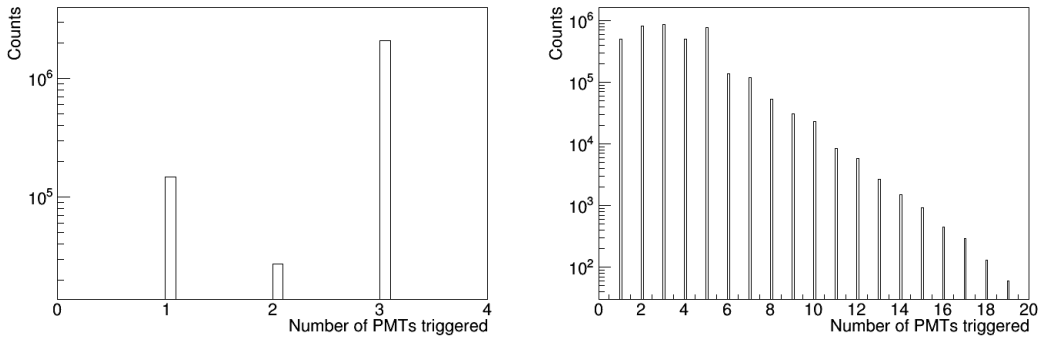

Figure 5.3.5: **Left:** Number of PMTs triggered in each event in the top layer of the inner muon veto. **Right:** Number of PMTs triggered in each event in the entire inner muon veto.

In conclusion, the inner muon veto has demonstrated its operational readiness for installation within CONUS+. The muon veto recorded a total rate of 74.73 ± 0.04 Hz using an energy cut to remove background radiation. Analysis of coincidences between PMTs reveals that in most cases, multiple PMTs are triggered simultaneously. This observation presents an opportunity to explore a complementary approach to applying an energy cut by identifying the angular incidence of muons through PMT coincidences.

This method will be explored in the next chapter, centred around the installation of the inner muon veto in CONUS+ and the first run of the entire muon veto.

Chapter 6

Installation of the muon veto at KKL

In the summer of 2023, the CONUS+ experiment, including the newly integrated inner muon veto system, was successfully installed at the nuclear power plant in Leibstadt. The installation process was executed with meticulous attention to cleanliness and contamination prevention, particularly for the inner components.

The installation commenced by assembling the CONUS+ lower shielding layers from outer to inner. For better access to position components, such as lead bricks, one side of the shielding was intentionally left partially disassembled, as depicted in the left image of Figure 6.0.1. In this image, the white layers are polyethylene, while the black scintillator plates belong to the muon veto. The detectors were installed before advancing to the upper layer of the CONUS+ shielding. During this installation, particular care was put on cleanliness and uniform force application to the cryostat's arm to prevent bending. Following multiple adjustments, the CONUS+ detectors were securely positioned within the shield. Subsequently, the upper portion of the CONUS+ shield was assembled.

Figure 6.0.1: **Left:** Lower half of the CONUS+ shielding. Three out of four muon veto side layers are installed. **Right:** View from the closed outer muon veto.

The left image of Figure 6.0.1 shows the closed outer muon veto. The copper cables on the top plate are the signal and high-voltage cables of the PMTs.

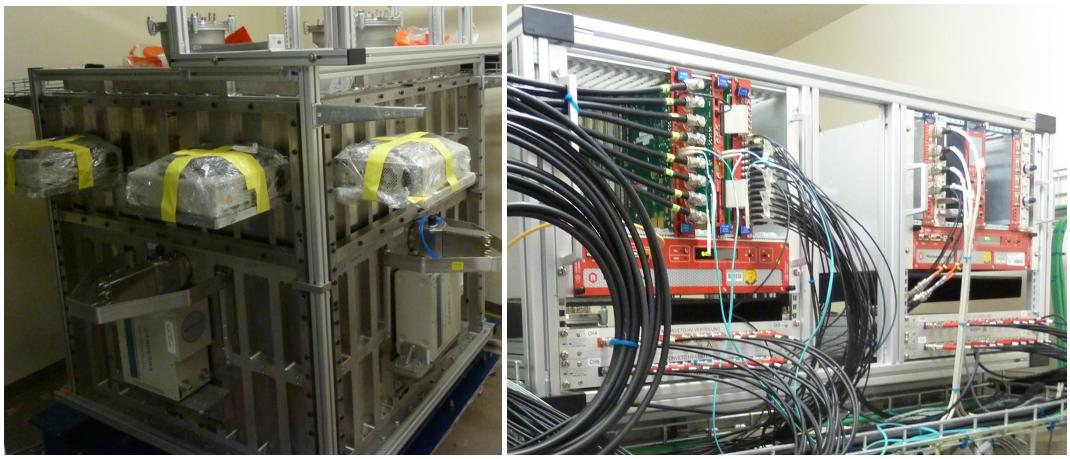

Figure 6.0.2: **Left:** Closed shield of CONUS+. **Right:** CONUS+ DAQ setup.

The left image of Figure 6.0.2 offers a view of the fully assembled CONUS+ shield. Within the setup, the signal and high-voltage cables are transferred through four feed-throughs located at the top of the shield. The DAQ system, shown on the right of Figure 6.0.2, was configured as detailed in section 2.4. This included the division of the PMT high voltage connections into seven groups, all of which were subsequently connected to five channel splitters. One splitter was intentionally left unconnected, providing flexibility for future experimentation involving varying voltages for specific PMTs.
Despite all efforts, testing the muon veto PMTs after the installation of CONUS+ revealed that two PMTs in the top inner layer were non-operational. Fortunately, the precautionary installation of four PMTs in the top layers allows for the continued operation of the inner top plastic scintillator plate.

The entire muon veto in KKL was tested in the same procedure as performed at MPIK (see section 5.3). This includes general analysis of the energy depositions inside the muon veto layers, as well as coincidence studies.
First, the energy spectra of both top plates were examined. The spectra are illustrated in Figure 6.0.3, with the outer veto on the right and the inner veto on the left. Notably, the PMTs in the newly installed inner muon veto demonstrate a much better energy resolution, enabling a more effective separation between the gamma background and muons via an energy cut.

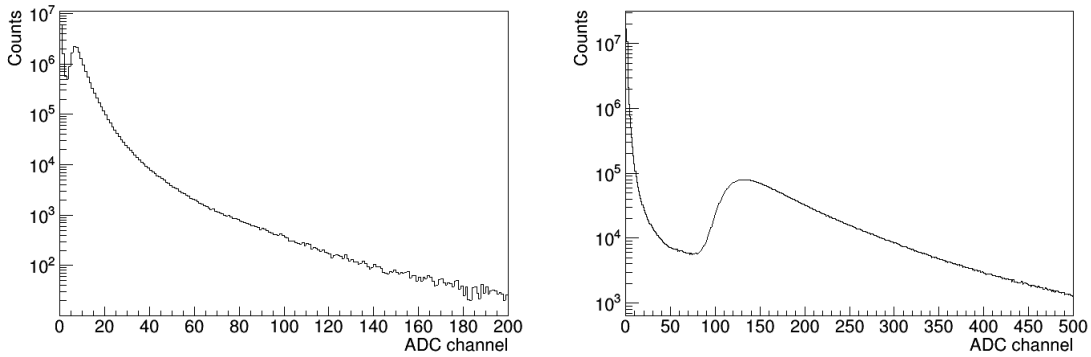

Figure 6.0.3: Spectra of PMTs in the inner and outer top plate. **Left:** Outer Plate: PMT 1466. **Right:** Inner Plate: PMT 1079.

Furthermore, the rates of both top plates were studied in the same method described in section 5.3. The rates are summarised in Table 6.1. On average, the top plate of the outer muon veto observed a rate of 92.89 ± 0.024 Hz. In comparison, the inner top plate averages at 54.775 ± 0.019 Hz. Within the same plates, the rates of the PMTs are in good agreement.

	Outer top plate				Inner top plate	
PMT	1466	1442	1487	1455	1080	1079
Rate[Hz]	92.340 ± 0.024	93.045 ± 0.024	93.727 ± 0.024	92.468 ± 0.024	54.792 ± 0.019	54.757 ± 0.019

Table 6.1: Rates of the top plate PMTs.

The muon veto was further studied with a PMT coincidence time window of 20 ns. The total rate of the entire muon veto is shown in Figure 6.0.4. With a linear fit, depicted in red, the average rate of 180.35 ± 0.05 Hz was obtained. With a muon rejection window of about 410 μs, this gives a dead time of about 7%. The rate was stable throughout the measurement.

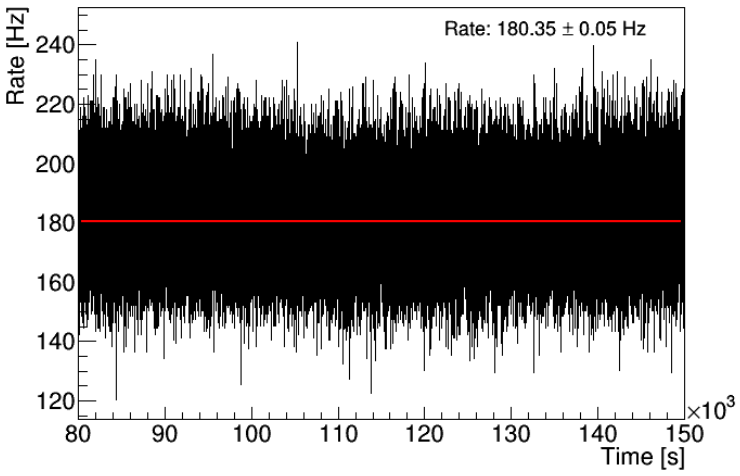

Figure 6.0.4: Total rate of the entire muon veto.

Additionally, the individual rates within the muon veto layers were analysed and compared to previous measurements at LLL and KBR.

The rate of the inner muon veto averages at 101.13 ± 0.04 Hz. Considering the muon flux measurements with the liquid scintillator module from section 3.6, a 1.6 times larger flux is expected at KKL compared to LLL. With about 74.73 ± 0.04 Hz in LLL (see section 5.3) this leads to an expected rate of $\sim 119.57 \pm 0.08$ Hz in KKL.

However, it is important to account for the additional overburden experienced by the inner muon veto due to being located inside the CONUS+ shield. This overburden results from $\sim$ 10 cm of lead, $\sim$ 5 cm of stainless steel and $\sim$ 10 cm of polyethylene, totalling an extra 1.8 m w.e.. Consequently, a slightly lower rate of about $\sim$ 107 Hz is expected. Any remaining discrepancies may be attributed to subtle variations in energy cuts employed during analysis.

Moreover, the CONUS+ muon veto run at KKL can be compared with a previous measurement of the CONUS muon veto at KBR. The outer muon veto in CONUS+ observed a rate of 178.02 ± 0.05 Hz in KKL, while at KBR in the CONUS setup, the veto observed a rate of 84 ± 4 Hz during reactor OFF-time. Hence, the KKL rate is about 2.1 times larger than that at KBR. This is less than expected by the measurements with the liquid scintillator module, which suggested a rate 2.6 times higher. As however the precise details of the energy cut applied to the KBR data remain unknown, it is not possible to compare these numbers precisely. Therefore a modest variance in these rates is justifiable.

Furthermore, the observation that the rate of the entire muon veto system slightly exceeded the rate obtained with the outer muon veto alone holds promise for the effectiveness of the muon veto upgrade in reducing background.

During the commissioning of the muon veto in KKL, the viability of a complementary method for muon track reconstruction was explored. Given the expectation that cosmic muons at relativistic energies tend to follow nearly straight paths with minimal scattering, it is reasonable to assume that for these muons the detection time difference between two scintillators is very small [83]. For this reason, a short coincidence window of 20 ns was set.

In Figure 6.0.5, the distribution of the number of PMTs triggered by the same event within the entire muon veto is depicted. Notably, the chart reveals a preference for an even number of triggered PMTs over an odd number, suggesting that both PMTs within the scintillator plates detect the muon in most cases. It is important to note that a maximum of twelve PMTs can be triggered by a single muon event. However, the chart extends well beyond this point, implying the presence of random coincidences within the scintillator plates. The number of coincidences drops considerably after reaching ten, as expected since these events require muons to arrive within a very limited range of incidence angles.

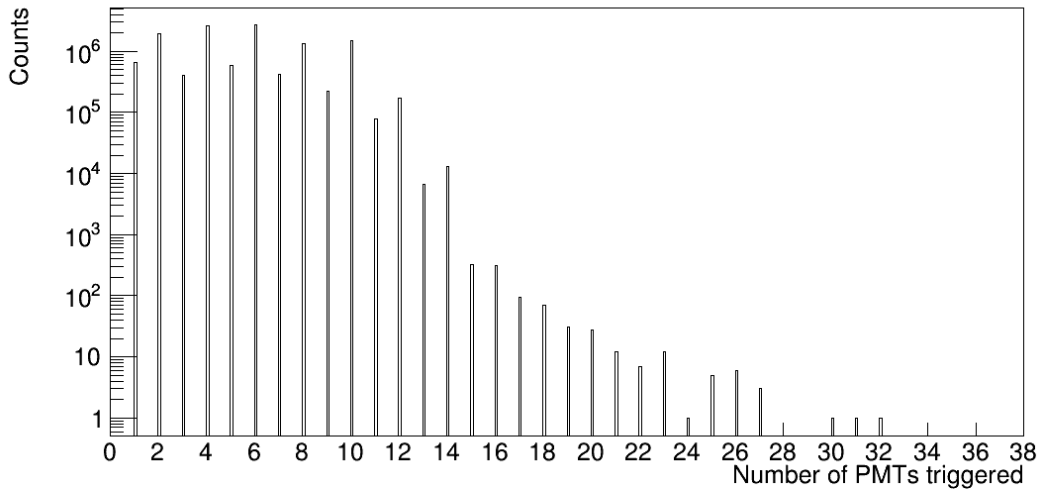

Figure 6.0.5: Number PMTs triggered in each event for the entire muon veto.

In Figure 6.0.6, the rates dependent on different coincidence requirements are presented. A rate of 137 Hz is observed for the coincidence of four PMTs. Considering that the outer top plate, which is the only scintillator plate with four PMTs, has a rate of 93 Hz, the additional events are due to coincidences between different scintillators. Furthermore, it is worth noting that more than half of the events result in signals detected by six PMTs and up to 14% in ten PMTs. Beyond this point, the rate for events involving more than twelve PMTs drops below $\sim$ 1 Hz.

Figure 6.0.6: Coincidence rates dependent on PMTs triggered per event.

This outcome is quite promising, suggesting the potential for muon track reconstruction. Such reconstruction could lead to the application of more refined criteria for background rejection and veto window time, ultimately reducing dead time and background for the CONUS+ experiment. Ongoing work includes the development of more advanced algorithms to further leverage this capability.

The muon veto system's primary objective is to reject muon-induced events inside the germanium crystals effectively. This involves defining a time window where all events are rejected following a signal over a certain energy threshold in the scintillator plates. However, the current lack of synchronisation between the ADC boards of the muon veto and the germanium detectors precludes the application of this rejection window to the germanium data.

Looking ahead, the first run of the entire muon veto offers a promising outlook for the CONUS+ experiment. The pivotal step of synchronising the ADC boards between the germanium spectrometers and the muon veto will enable the successful mitigation of muon-induced background in the CONUS+ experiment.

Chapter 7

Conclusion and Outlook

This Master's thesis successfully contributed to the CONUS+ experiment by developing a new muon veto to address the increased muon flux at the experimental location in the Leibstadt nuclear power plant. The work included on-site muon flux measurements, simulations of the impact of introducing the new muon veto layer to the CONUS+ shielding, and the commissioning and installation process.

The CONUS+ experiment is a follow-up experiment of CONUS and uses an upgraded setup of its detector. It is located at the nuclear power plant in Leibstadt (KKL), Switzerland. At the experimental site an electron antineutrino flux of $1.45 \times 10^{13} \mathrm{s}^{-1}\mathrm{cm}^{-2}$ is expected.

A series of gamma and muon flux measurements were performed on-site at KKL. The gamma measurements were conducted with the CONRAD HPGe spectrometer. The contributions of high energy gammas over 2.7 MeV were found to be a factor 25 smaller than in KBR. However, the KKL spectrum showed a more pronounced presence of ^{60}Co and a stronger contribution of gammas from neutron capture in iron.
Muon flux measurements on-site at the nuclear power plant were performed using a liquid scintillator module, calibrated with ^{137}Cs source at the Max Planck Institut für Kernphysik (MPIK) in Heidelberg. The muon rate during reactor outage was about $0.3479^{+0.0012}_{-0.0016}$ Hz, corresponding to $112.5^{+0.4}_{-0.5}$ Hz/cm^2. This elevated muon rate, approximately 2.6 times larger than that at the former experimental location of CONUS in the power plant Brokdorf (KBR), was attributed to a reduction in overburden at KKL to about 6 m w.e. compared to 24 m w.e. at KBR. To maintain a similar background level in CONUS+, the muon veto is required to improve its background rejection efficiency from $\sim$97% to over 98.8%. This motivated the introduction of an additional muon veto within the CONUS+ shielding.

One of the main updates of the shielding is the replacement of an inner lead layer with a second plastic scintillator layer, which functions as an active muon veto. Each muon veto consists of nine plastic scintil-

lator plates, with a quadratic top plate and two stacked scintillator plates forming the sides. The top plates are equipped with four photomultiplier tubes (PMTs), while each side plate is outfitted with two PMTs.

A series of Monte Carlo (MC) simulations were performed to investigate the impact of a muon veto upgrade. The simulations included the entire geometry of the CONUS+ setup, encompassing the shield and detectors. The muon flux was accurately simulated for the location at the nuclear power plant in Leibstadt considering the angular and energy distribution of muons. Simulations indicate that the outer muon veto has a total rejection efficiency in the region of interest (ROI) of CEνNS of $\varepsilon_{out} \approx 99.74\%$, and the inner muon veto of $\varepsilon_{in} \approx 98.01\%$. These promising results suggest that a remarkably high level of efficiency for the muon veto of CONUS+, reaching approximately 99% is attainable in theory. However, practical considerations, such as the detection efficiency of the scintillator plates, could slightly reduce this number.

Additional Geant4 MC simulations were conducted to examine the light collection efficiency of the PMTs inside the plastic scintillator layers. The analysis confirmed the suitability of the PMT configuration for optimal light collection.
MC simulations also explored the potential contribution of a new material background caused by the PMTs and scintillator plates. The upper limit for events within the region of interest (ROI) for CEνNS was below 2×10^{-1} events per year for the entire system, with an expected total of 4.34×10^{-1} events per year in the ROI for the neutrino magnetic moment (NMM).
In addition, simulations were conducted to assess the impact of external gamma radiation based on the measurements performed with CONRAD. These simulations yielded no events within the CEνNS and NMM ROI, aligning with expectations that the gamma background was already a subdominant factor in the original CONUS setup. In total, less than 2.4 events are expected per day. Future simulations with better statistics will be able to constrain this limit further.

Prior to its installation, the inner muon veto underwent testing at the MPIK. Based on these tests, the PMTs' optimal positions within the CONUS+ shielding were chosen.
Additional work went into studying the light yield of the scintillator plates. The light yield was obtained experimentally using a ^{60}Co source and through an MC simulation. Experimental measurements estimated a light yield of 174 ± 9 for the top plate and light yields averaging at 177 ± 6 and 71.0 ± 2.7 for the lateral top and bottom plates respectively. These numbers were in the same order of magnitude as values obtained in light yield simulations.

To evaluate the performance of the inner CONUS+ muon veto, the system was tested in the Low-Level Laboratory (LLL) at the MPIK with an overburden of 15 m w.e.. Examination of the energy deposition spectra showed strong agreement with the MC simulations. Subsequently, a more detailed analysis was

performed, with a coincidence window of 20 ns in addition to an energy cut aimed to remove background radiation. This analysis revealed a rate of 64.52 ± 0.04 Hz/m^2 within the top plate of the plastic scintillator. This compares well to the rate obtained with the liquid scintillator module in LLL, which measured $70.12(^{+0.12}_{-0.11})_{\text{syst}}(\pm 0.60)_{\text{stat}}$ Hz/m^2. The total rate of the inner muon veto in LLL is 74.73 ± 0.04 Hz. Additionally, investigations of coincidence between PMTs revealed that, in most cases of muon detection, more than one PMT is triggered.

Finally, in August 2023, the CONUS+ experiment, including the newly integrated inner muon veto, was successfully installed at the nuclear power plant in Leibstadt. Tests following the installation of the muon veto plates showed that two PMTs in the inner top layer were non-operational. However, due to the precaution of equipping the top layers with four PMTs, the inner plastic scintillator plate can still be operated.
Examination of the energy spectra of both top scintillator plates indicated that the PMTs of the newly installed inner muon veto exhibit a much better energy resolution, allowing a more effective separation between gamma background and muons via an energy cut.
Studying the entire muon veto with a coincidence time window of 20 ns and an energy cut, revealed an average rate of 180.35 ± 0.05 Hz, which leads to a dead time of about 7%. Moreover, the separate rates of both vetos were studied and compared to previous measurements at LLL and KBR. In total the inner muon veto averaged at 101.13 ± 0.04 Hz and the outer veto at 178.02 ± 0.05 Hz. This observation suggests a potential enhancement in background rejection by employing two muon vetos instead of one.

Based on the liquid scintillator measurements, a 1.6 times larger flux of $\sim 119.57 \pm 0.08$ was expected for the inner muon veto rate at KKL. Considering the additional overburden experienced by the inner muon veto due to being located within the CONUS+ shield and slight variations in energy cut, the rates are in good agreement.
Furthermore, a comparison was made between the rates of the outer muon veto in CONUS+ in KKL and a previous measurement in CONUS at KBR. For the outer veto, a 2.1 larger rate was found at KKL, contrasting the expected 2.6 increase expected based on measurements with the liquid scintillator module. As however the precise details of the energy cut applied to the KBR data remain unknown, it is not possible to compare these numbers exactly. Therefore, a modest variance in these rates is justifiable.

As previously demonstrated in the inner muon veto run at LLL, in most cases, muons trigger more than one PMT. Upon studying the rates in KKL dependent on the required number of PMTs triggered, it was revealed that up to 14% of the events triggered ten PMTs. This observation provided a promising opportunity to explore a complementary approach for muon track reconstruction, utilising coincidence requirements.

The primary objective of the muon veto system is to effectively reject muon-induced events inside the germanium crystals. This involves defining a time window within all events are rejected following a signal over a certain energy threshold in the scintillator plates. In future analysis, the rejection of muon-induced events will be studied.

In conclusion, this Master's thesis has effectively contributed to the CONUS+ experiment by devising and implementing an advanced muon veto. The established simulation framework will serve as a valuable tool for assessing potential future CONUS+ setup enhancements and deepening our knowledge of the muon veto operation.

Looking forward, the application of the muon veto rejection window will facilitate a comprehensive study of the background reduction, thereby allowing us to assess the effectiveness of the muon veto in rejecting background signals. Parameters such as the muon veto window will require optimisation to achieve optimal results.
Furthermore, coincidence analysis will enable a complementary approach for muon identification, with the potential to significantly enhance the rejection efficiency of the muon veto. The work accomplished in this Master's thesis sets the foundation for future research into the development and refinement of the coincidence algorithm for the CONUS+ muon veto system.

Bibliography

[1] Gary Steigman. Neutrinos and big bang nucleosynthesis. Advances in High Energy Physics, 2012: 1–24, 2012. doi: 10.1155/2012/268321. URL https://doi.org/10.1155%2F2012%2F268321.

[2] C. L. Cowan, F. Reines, F. B. Harrison, H. W. Kruse, and A. D. McGuire. Detection of the free neutrino: a confirmation. Science, 124(3212):103–104, 1956. doi: 10.1126/science.124.3212.103. URL https://www.science.org/doi/abs/10.1126/science.124.3212.103.

[3] Q. R. et al. Ahmad. Measurement of the rate of $\nu_e + d \rightarrow p + p + e^-$ interactions produced by ^8b solar neutrinos at the sudbury neutrino observatory. Phys. Rev. Lett., 87:071301, Jul 2001. doi: 10.1103/PhysRevLett.87.071301. URL https://link.aps.org/doi/10.1103/PhysRevLett.87.071301.

[4] Y. et al. Fukuda. Evidence for oscillation of atmospheric neutrinos. Phys. Rev. Lett., 81:1562–1567, Aug 1998. doi: 10.1103/PhysRevLett.81.1562. URL https://link.aps.org/doi/10.1103/PhysRevLett.81.1562.

[5] John N. Bahcall. Solar neutrinos. i. theoretical. Phys. Rev. Lett., 12:300–302, Mar 1964. doi: 10.1103/PhysRevLett.12.300. URL https://link.aps.org/doi/10.1103/PhysRevLett.12.300.

[6] Hitoshi Murayama. The origin of neutrino mass. Physics World, 15(5):35, may 2002. doi: 10.1088/2058-7058/15/5/36. URL https://dx.doi.org/10.1088/2058-7058/15/5/36.

[7] O.G. Miranda and J.W.F. Valle. Neutrino oscillations and the seesaw origin of neutrino mass. Nuclear Physics B, 908:436–455, 2016. ISSN 0550-3213. doi: https://doi.org/10.1016/j.nuclphysb.2016.03.027. URL https://www.sciencedirect.com/science/article/pii/S055032131630013X. Neutrino Oscillations: Celebrating the Nobel Prize in Physics 2015.

[8] LEGEND Collaboration, N. Abgrall, I. Abt, M. Agostini, A. Alexander, C. Andreoiu, G. R. Araujo, III Avignone, F. T., W. Bae, A. Bakalyarov, and et al. LEGEND-1000 Preconceptual Design Report. arXiv e-prints, art. arXiv:2107.11462, July 2021. doi: 10.48550/arXiv.2107.11462.

[9] C. Augier et al. Measurement of the $2\nu\beta\beta$ decay rate and spectral shape of ^{100}Mo from the CUPID-Mo experiment. 7 2023.

[10] G. Adhikari et al. nEXO: neutrinoless double beta decay search beyond 10^{28} year half-life sensitivity. J. Phys. G, 49(1):015104, 2022. doi: 10.1088/1361-6471/ac3631.

[11] Christian Spiering. Towards high-energy neutrino astronomy. The European Physical Journal H, 37(3): 515–565, jul 2012. doi: 10.1140/epjh/e2012-30014-2. URL https://doi.org/10.1140%2Fepjh%2Fe2012-30014-2.

[12] D. Akimov et al. Observation of coherent elastic neutrino-nucleus scattering. Science, 357 (6356):1123–1126, sep 2017. doi: 10.1126/science.aao0990. URL https://doi.org/10.1126%2Fscience.aao0990.

[13] D. Akimov et al. First measurement of coherent elastic neutrino-nucleus scattering on argon. Physical Review Letters, 126(1), jan 2021. doi: 10.1103/physrevlett.126.012002. URL https://doi.org/10.1103%2Fphysrevlett.126.012002.

[14] Daniel Z. Freedman. Coherent effects of a weak neutral current. Phys. Rev. D, 9:1389–1392, Mar 1974. doi: 10.1103/PhysRevD.9.1389. URL https://link.aps.org/doi/10.1103/PhysRevD.9.1389.

[15] R. Aaij et al. Measurement of the forward-backward asymmetry in z/$* \rightarrow$ - decays and determination of the effective weak mixing angle. Journal of High Energy Physics, 2015(11), nov 2015. doi: 10.1007/jhep11(2015)190. URL https://doi.org/10.1007%2Fjhep11%282015%29190.

[16] Thomas Rink. Coherent elastic neutrino-nucleus scattering – First constraints/observations and future potential. In 56th Rencontres de Moriond on Electroweak Interactions and Unified Theories, 5 2022.

[17] Basudeb Dasgupta and Joachim Kopp. Sterile neutrinos. Physics Reports, 928:1–63, sep 2021. doi: 10.1016/j.physrep.2021.06.002. URL https://doi.org/10.1016%2Fj.physrep.2021.06.002.

[18] M. Abdullah et. al. Coherent elastic neutrino-nucleus scattering: Terrestrial and astrophysical applications, 2022.

[19] H. Bonet et al. Novel constraints on neutrino physics beyond the standard model from the CONUS experiment. JHEP, 05:085, 2022. doi: 10.1007/JHEP05(2022)085.

[20] Caroline von Raesfeld and Patrick Huber. Use of CEvNS to monitor spent nuclear fuel. Phys. Rev. D, 105(5):056002, 2022. doi: 10.1103/PhysRevD.105.056002.

[21] James R. Wilson. Coherent neutrino scattering and stellar collapse. Phys. Rev. Lett., 32:849–852, Apr 1974. doi: 10.1103/PhysRevLett.32.849. URL https://link.aps.org/doi/10.1103/PhysRevLett.32.849.

[22] Kate Scholberg. Observation of coherent elastic neutrino-nucleus scattering by coherent, 2018.

[23] Mark Thomson. Mondern Particle Physics. Cambridge University Press, 2013.

[24] Patrick Huber. Determination of antineutrino spectra from nuclear reactors. Physical Review C, 84(2), aug 2011. doi: 10.1103/physrevc.84.024617. URL https://doi.org/10.1103%2Fphysrevc.84.024617.

[25] Vadim A. Bednyakov and Dmitry V. Naumov. Coherency and incoherency in neutrino-nucleus elastic and inelastic scattering. Phys. Rev. D, 98:053004, Sep 2018. doi: 10.1103/PhysRevD.98.053004. URL https://link.aps.org/doi/10.1103/PhysRevD.98.053004.

[26] J.L. Autran, D. Munteanu, T. Saad Saoud, and S. Moindjie. Characterization of atmospheric muons at sea level using a cosmic ray telescope. Nuclear Instruments and Methods in Physics Research Section A: Accelerators, Spectrometers, Detectors and Associated Equipment, 903:77–84, 2018. ISSN 0168-9002. doi: https://doi.org/10.1016/j.nima.2018.06.038. URL https://www.sciencedirect.com/science/article/pii/S0168900218307599.

[27] O. C. Allkofer and P. K. F. Grieder. Cosmic rays on earth. 1984.

[28] G. Hausser. Cosmic ray-induced background in ge-spectrometry. Nuclear Instruments and Methods in Physics Research Section B: Beam Interactions with Materials and Atoms, 1993. doi: https://doi.org/10.1016/0168-583X(93)95931-T.

[29] Michael F. L'Annunziata. Radioactivity. Elsevier Science B.V., 2007. ISBN 978-0-444-52715-8.

[30] C. Dees. Neutron radiation shielding strategies for glovebox applications. URL https://www.osti.gov/biblio/1401982.

[31] Bundesamt für Strahlenschutz. Radon in gebäuden, 2022. https://www.bfs.de/DE/themen/ion/umwelt/radon/vorkommen/gebauede.html.

[32] Maiano C. Pattavina L. et al. Clemenza, M. Radon-induced surface contaminations in low background experiments. The European Physical Journal C, 71(11):1805, 2011. doi: 10.1140/epjc/s10052-011-1805-0.

[33] Susana Cebriá n. Cosmogenic activation of materials. International Journal of Modern Physics A, 32(30):1743006, oct 2017. doi: 10.1142/s0217751x17430060. URL https://doi.org/10.1142%2Fs0217751x17430060.

[34] Yoichiro Shimazu. Molten Salt Reactors and Thorium Energy. Woodhead Publishing, 2017. ISBN 9780081011263.

[35] Matts Roos. Sources of gamma radiation in a reactor core. Journal of Nuclear Energy. Part B. Reactor Technology, pages 98–104, 1959. doi: https://doi.org/10.1016/S0368-3273(15)30005-5.

[36] E. Aprile et al. Search for coherent elastic scattering of solar neutrinos in the XENON1t dark matter experiment. Physical Review Letters, 126(9), mar 2021. doi: 10.1103/physrevlett.126.091301. URL https://doi.org/10.1103%2Fphysrevlett.126.091301.

[37] Florian Jörg. From 222Rn measurements in XENONnT and HeXe to radon mitigation in future liquid xenon experiments. Phd thesis, August 2022. URL http://www.ub.uni-heidelberg.de/archiv/31915.

[38] CONNIE Collaboration and A. Aguilar-Arevalo et al. The connie experiment, 2016.

[39] Youssef Sarkis. The CONNIE experiment: upgrade and latest results. Zenodo, Jul 2022. doi: 10.5281/zenodo.6785368.

[40] Venktesh Singh and Henry T. Wong. Recent results and status of texono experiments, 2004.

[41] V. Sharma et al. Studies of quantum-mechanical coherency effects in neutrino-nucleus elastic scattering. Phys. Rev. D, 103(9):092002, 2021. doi: 10.1103/PhysRevD.103.092002.

[42] I.et al Alekseev. First results of the νGeN experiment on coherent elastic neutrino-nucleus scattering. Phys. Rev. D, 106:L051101, Sep 2022. doi: 10.1103/PhysRevD.106.L051101. URL https://link.aps.org/doi/10.1103/PhysRevD.106.L051101.

[43] H. et al. Bonet. Constraints on elastic neutrino nucleus scattering in the fully coherent regime from the CONUS experiment. Phys. Rev. Lett., 126(4):041804, 2021. doi: 10.1103/PhysRevLett.126.041804.

[44] J. Colaresi, J. I. Collar, T. W. Hossbach, C. M. Lewis, and K. M. Yocum. Measurement of Coherent Elastic Neutrino-Nucleus Scattering from Reactor Antineutrinos. Phys. Rev. Lett., 129(21):211802, 2022. doi: 10.1103/PhysRevLett.129.211802.

[45] Ricochet Collaboration et al. Ricochet progress and status, 2021.

[46] Ardellier-Desages F. Bento A. et al. Angloher, G. Exploring CEvNS with NUCLEUS at the Chooz nuclear power plant. Eur. Phys. J., 2019. doi: https://doi.org/10.1140/epjc/s10052-019-7454-4.

[47] Janina Dorin Hakenmüller. Looking for coherent elastic neutrino nucleus scattering with the CONUS experiment. Phd thesis, 2020.

[48] Preussen Elektra. Nuclear power plant brokdorf. URL https://www.preussenelektra.de/de/das-sind-wir/unsere-kraftwerke/kraftwerkbrokdorf.html.

[49] J. Hakenmüller et al. Neutron-induced background in the CONUS experiment. Eur. Phys. J. C, 79(8): 699, 2019. doi: 10.1140/epjc/s10052-019-7160-2.

[50] H. Bonet et al. Large-size sub-keV sensitive germanium detectors for the CONUS experiment. Eur. Phys. J. C, 81(3):267, 2021. doi: 10.1140/epjc/s10052-021-09038-3.

[51] H. Bonet et al. Full background decomposition of the CONUS experiment. Eur. Phys. J. C, 83(3):195, 2023. doi: 10.1140/epjc/s10052-023-11240-4.

[52] Leibstadt AG. Nuclear power plant leibstadt. URL https://www.kkl.ch/unternehmen/ueber-uns.

[53] JULABO UK Ltd. F500 compact recirculating cooler. URL https://www.julabo.com/de/produkte/umlaufkuehler-umwaelzkuehler/f-kompakt-umlaufkuehler/f500.

[54] Scionix Holland B.V. General purpose ej-200, ej-204, ej-208, ej-212. URL ,https://scionix.nl/frame/.

[55] Matsusada. What is a photomultiplier tube (pmt)? URL https://www.matsusada.com/application/ps/photomultiplier_tubes/.

[56] 51 mm (2") photomultiplier 9954B series data sheet. ET Enterprises, Ltd., 2010.

[57] Tobias Schierhuber. Ultra-Low Background Germanium Spectroscopy. Master's thesis, 2017.

[58] Photomultiplier tube R8520-406/R8520-506. Hamamatsu Photonics K.K., 2021. URL https://www.hamamatsu.com/content/dam/hamamatsu-photonics/sites/documents/99_SALES_LIBRARY/etd/R8520-406_TPMH1342E.pdf.

[59] E. Aprile et al. The XENON1T Dark Matter Experiment. Eur. Phys. J. C, 77(12):881, 2017. doi: 10.1140/epjc/s10052-017-5326-3.

[60] E. Aprile et al. Material screening and selection for XENON100. Astroparticle Physics, 35(2): 43–49, sep 2011. doi: 10.1016/j.astropartphys.2011.06.001. URL https://doi.org/10.1016%2Fj.astropartphys.2011.06.001.

[61] V1740D. CAEN S.p.A., . URL https://www.caen.it/products/v1740d/.

[62] N8032. CAEN S.p.A., . URL https://www.caen.it/products/n8032/.

[63] Janina Hakenmüller and Gerd Heusser. Conrada low level germanium test detector for the conus experiment. Applied Radiation and Isotopes, 194:110669, 2023. ISSN 0969-8043. doi: https://doi.org/10.1016/j.apradiso.2023.110669. URL https://www.sciencedirect.com/science/article/pii/S0969804323000222.

[64] Lynx Digital Signal Analyzer. Mirion Technologies, Inc., 2019. URL https://mirionprodstorage.blob.core.windows.net/prod-20220822/cms4_mirion/files/pdf/spec-sheets/ops-509_lynx_dsa_spec_rebrand_5.pdf.

[65] Anders Nordlund Hakan Mattsson, Farshid Owrang. Utilisation of ^{16}N in Nuclear Power Plants. CHALMERS UNIVERSITY OF TECHNOLOGY DEPARTMENT OF REACTOR PHYSICS, 2003.

[66] Moritz Raab. Optical properties and pulse shape discrimination of safe liquid scintillators. Bachelor's thesis, 2021.

[67] CAEN S.p.A. V1725 / v1725s. URL https://www.caen.it/products/v1725/.

[68] User Manual UM5960 CoMPASS Multiparametric DAQ Software for Physics Applications. CAEN SpA, 2020. Rev. 11 - April 1st.

[69] Root: analyzing petabytes of data, scientifically. https://root.cern/. Accessed: 2023-09-07.

[70] Santosh Gupta and Yuanbing Mao. Nano Scintillator-Book. 09 2020.

[71] John B. Birks. The Theory and practice of scintillation counting. 1964.

[72] Michal Cieslak, Kelum Gamage, R. Glover, and C. James Taylor. Pulse shape discrimination performance of a pixelated plastic scintillator (ej-299-34) for a coded-aperture based dual particle imaging system. Journal of Instrumentation, 14:P07017–P07017, 07 2019. doi: 10.1088/1748-0221/14/07/P07017.

[73] autospur.de. Höhenanfragen für standorte, 2023. https://www.autospur.de/Staumeldungen/wie-hoch.html15,49.384161,8.706644.

[74] D Delacroix, J Guerre, P Leblanc, and C Hickman. Radionuclide and radiation protection data handbook 2nd edition (2002). Radiation protection dosimetry, 98:9–168, 02 2002. doi: 10.1093/oxfordjournals.rpd.a006705.

[75] Mohammad Safari, Fereydoun Abbasi davani, and Hossein Afarideh. Differentiation method for localization of compton edge in organic scintillation detectors. 10 2016. doi: 10.22034/rpe.2020.104839.

[76] Yuen-Dat Chan et al. Mage - a geant4-based monte carlo framework for low-background experiments, 2008.

[77] Prashant Shukla and Sundaresh Sankrith. Energy and angular distributions of atmospheric muons at the earth, 2018.

[78] Tatsuhiko Sato. Analytical model for estimating terrestrial cosmic ray fluxes nearly anytime and anywhere in the world: Extension of parma/expacs. PloS one, 10:e0144679, 12 2015. doi: 10.1371/journal.pone.0144679.

[79] Tatsuhiko et al. Sato. Particle and heavy ion transport code system, phits, version 2.52. Journal of Nuclear Science and Technology, 50:913–923, 06 2013. doi: 10.1080/00223131.2013.814553.

[80] Donald E. Groom et al. Muon stopping power and range tables 10 mev-100 tev. Atomic Data and Nuclear Data Tables, 2001. URL `https://pdg.lbl.gov/2023/AtomicNuclearProperties/adndt.pdf`.

[81] General purpose ej-200, ej-204, ej-208, ej-212. https://eljentechnology.com/products/plastic-scintillators/ej-200-ej-204-ej-208-ej-212. Accessed: 2023-30-09.

[82] F.G. Kondev, M. Wang, W.J. Huang, S. Naimi, and G. Audi. The nubase2020 evaluation of nuclear physics properties *. Chinese Physics C, 45(3):030001, mar 2021. doi: 10.1088/1674-1137/abddae. URL `https://dx.doi.org/10.1088/1674-1137/abddae`.

[83] Jan Paepen et al. Characterisation of plastic scintillators used as an active background shield for neutron detection. JRC Technical Reports, 2016.

List of Figures

List of Tables

Acknowledgement

I would like to express my sincere gratitude to the individuals whose contributions and support were instrumental in the completion of my Master's thesis. First and foremost, I extend my heartfelt thanks to Prof. Dr. Dr. h.c. Manfred Lindner for providing me with the invaluable opportunity to undertake my thesis within the CONUS group at MPIK.

Furthermore, I am deeply grateful to Dr. Christian Buck, Dr. Werner Maneschg, and Nicola Ackermann for their invaluable assistance in reviewing and refining my thesis. I also wish to acknowledge the entire CONUS group for fostering a welcoming environment, offering assistance with all my challenges, and generously dedicating their time to answer my queries. Special recognition goes to Nicola Ackermann and Janina Hakenmüller for their invaluable assistance with my Geant4 simulations.

Last but certainly not least, I want to convey my utmost appreciation to Dr. Edgar Sanchez for his exceptional patience, kindness, and unwavering support throughout the course of my Master's thesis. I cannot envision having a more dedicated supervisor. Thank you, Edgar.